2009-2010 AIAA Foundation

Team Aircraft Design Competition

-Proposal-

USC Advanced Commercial Concepts Presents:

Albatross

University of Southern California

Devin Lewis
Member # 307714
Payload
Aesthetics
Ground Operations

Todd Erickson
Member # 421648
Propulsion
Configuration
Alternative Fuels

Sina Golshany
Member # 281677
Lead Designer
Propulsion
Configuration

Chris Nvavu
Invoice # 721079
Configuration
Structures
Ergonomics

Keith Holmlund
Member # 413045
High Speed Aerodynamics
Low Speed Aerodynamics
Aircraft Performance

Kristina Larson
Member # 306306
Management
High Speed Aerodynamics
Configuration

Phillip Adkins
Invoice # 715137
Acoustics
Numerical Analysis
Tool Development

Michael Zarem
Member # 416621
Systems Integration
Environmental Impact
Cost Analysis

Darin Gaytan
Member # 279164
Aircraft Performance
Configuration
Flight Dynamics

John Roehrick
Member # 421593
Weights
Acoustics
Systems

Dr. Ron Blackwelder
Faculty Advisor
Member # 1460

Dr. Oussama Safadi
Project Advisor
Member # 283128

Aaron Chang
Industrial Advisor
Invoice # 716176

Table of Contents

Nomenclature:

A	Blade wetted area
α	Angle of attack
AR_W	Wing aspect ratio
$\bar{\gamma}$	Average flight path angle
C_a/C_w	Aileron chord to wing chord ratio
C_{D0}	Parasite drag coefficient
$C_{D0_{TO}}, C_{D0_{clean}}$	Airplanes zero-lift drag coefficient at takeoff, clean configuration
$C_{d_{blade}}$	Average Blade Drag Coefficient
C_{ENVTAX}	Cost associated with environmental taxation
$C_{L_{max_{S\,(Clean)}}}$	Maximum lift coefficient for clean stall configuration
$C_{L_{max_{TO}}}$	Maximum lift coefficient at takeoff
$C_{L_{opt,MaxR}}$	Lift coefficient correspond to the optimum range performance
C_{l_a}	Airplane rolling-moment-coefficient due to ailerons deflection
$C_{m_{a,}}$	Airplane pitching-moment-coefficient-due-to-AOA derivative
C_{l_β}	Airplane rolling-moment-coefficient-due-to-yaw rate-derivative
C_{n_β}	Airplane yawing-moment-coefficient-due-to-side-slip-derivative
d/D	Ratio of the radome diameter to the average diameter of the mid fuselage
D_p	Diameter of the propeller
Δ_n	Correction factor due to pilot technique and handling qualities
$\Delta W_{F_{usedi}}$	Fuel weight used in the i'th segment
$\Delta c_{l_{\delta f_{TO}}}, \Delta c_{l_{\delta f_L}}$	Change of sections airfoil coefficient due to flaps deflection
$\Delta C_{L_{W\delta fTO}}, \Delta C_{L_{W\delta fL}}$	Change in wing lift coefficient due to flap deflection
$\zeta_{P,long}$	Longitudinal phugoid mode damping ratio
ζ_{SP}	Short period mode damping ratio
η_{i_f}	Flap inboard station, in term of wing half span
η_{O_f}	Flap outboard station, in term of wing half span
I_{xx_B}, I_{yy_B}, I_{zz_B}	Moment of inertia along the body axis
$Level_P$	Level for phugoid stability
$Level_{\xi SP}$	Level for short period damping
$L/D\big\|_{TO}$	Lift-to-Drag ratio at takeoff
λ_w	Wing taper ratio
Λ_w	Wing sweep angle

Λ_{LE}	Leading edge wing sweep
m_b	Blade mass
M_{DD}	Drag divergence Mach number
M_i	Normalized emission multiplier
M_{ff}	Fuel Fraction: 1- (Fuel Weight/Takeoff Weight)
NP_{free}	Free stick neutral point
$P_{1,2}$	Intermediate parameters to compute Phillip's angle (Section 5.8)
P_3	Combustor inlet pressure
Π_{TO}	Engine setting at takeoff
ϱ_F	Fuel density
Re_{tr}	Reynolds number corresponding to the chordwise transition to turbulence
S_{air}	Distance from obstacle height to the point of touchdown
S_L	Landing distance
S_{LG}	Ground roll landing distance
S_{NO_x}	NOx severity index
S_{TO}	Total field length
S_{TOG}	Take-off ground run distance
S_W	Wing surface area
SM	Static margin
$T_{1/2_P}$	Time to half amplitude in phugoid mode
T_{2_P}	Time to double amplitude in phugoid mode
T_3	Combustor inlet temperature
T_{avail}	Thrust available
T_{req}	Thrust required
v_0	Initial tangential blade velocity at blade center of mass
V_A	Approach speed
$V_{Cr_{Max}}$	Maximum cruise speed
V_{LOF}	Speed at liftoff
V_{SL}	Landing stall speed
$V_{S_{TO}}$	Takeoff stall speed
war	Water-to-air ratio
W_E	Empty weight
$W_{F\ \text{used}}$	Weight of fuel used
W_{TO}	Takeoff weight
$(W/S)_{TO_{max}}$	Maximum take-off wing loading
$(W/T)_{TO_{max}}$	Maximum take-off power loading
φ_T	Thrust vector inclination with respect to freestream airflow

X_{apex_W}	X coordinate of the wing apex (i.e. distance b/w wing quarter chord station and the nose reference point)
$\bar{x}_{ac}, \bar{x}_{ac_{wf}}, \bar{x}_{ac_h}$	X coordinate of aerodynamic center in terms of mean aerodynamic chord
X_{CG}, Y_{CG}, Z_{CG}	Location of center of gravity
$\bar{x}_{cg}$	X coordinate of center of gravity in terms of mean aerodynamic chord
$\omega_{n_{P,long}}$	Longitudinal phugoid mode undamped natural frequency
$\omega_{n,S.P}$	Short period undamped natural frequency
Ω	Phillip's angle (Impingement angle) of a released blade

Acronyms:

AAA	Advanced Aircraft Analysis
AIAA	American Institute of Aeronautics and Astronautics
AIC	Aviation Induced Cloudiness
AIMC	Aircraft Information Management Computer
ACE	Actuator Control Electronics
APU	Auxiliary Power Unit
ASM	Air Separation Module
BPR	Bypass Ratio
CAROC	Cash Airplane-Related Operating Costs
CFD	Computational Fluid Dynamics
CG	Center of Gravity
DLU	Data Localizing Units
DOC	Direct Operating Cost
EPNdB	Effective Perceived Noise in Decibels
ESDU	Engineering Sciences Data Unit
ECS	Environmental Control System
E/E	Electrical/Electronics
EIS	Entry into Service Date
FAR	Federal Air Regulation
GTF	Geared Turbo Fan
HRJ	Hydrotreated Renewable Jet
HUD	Head Up Display
ICA	Initial Cruise Altitude
ISA	International Standard Atmosphere
L/D	Lift-to-Drag Ratio
MIDU	Multi-Function Interactive Display Unit
MLW	Maximum Landing Weight
NLF	Natural Laminar Flow
OEI	One Engine Inoperative
PFCC	Primary Flight Control Computers
RDTE	Research Development Testing and Evaluation
RFP	Request for Proposal
RMPU	Remote Power Management Unit
SAR	Specific Air Range
SFC	Specific Fuel Consumption
TSFC	Thrust Specific Fuel Consumption
UACC	University of Southern California Advanced Commercial Concepts
ULD	Unit Load Device

Acknowledgement:

Having completed this project, we would like to express our appreciation of the help and support given by the faculty of USC's aerospace and mechanical engineering department. First of all, we wish to thank the people who were integral to the creation of this project: *Dr. Ron Blackwelder, Mr. Blaine Rawdon,* and *Mr. Mark Page.* With their experience in the field of aircraft design, they have been very supportive in all the phases of this project. During the first months of his retirement, *Dr. Ron Blackwelder* contributed greatly to all aspects of this project, including technical and organizational support for team members. *Dr. R.J. Huyssen*, managing director of Diomedes Innovations, Ltd. also contributed greatly to by providing well needed advice and feedback, mostly in relation to configuration design and engine integration. Special thanks are also due to Marc Aubertine in USC's writing program for his contribution to the organization and composition of this proposal.

Several people have been instrumental in allowing this project to be completed, but above all, we are indebted to our editorial supporters: Professors *Larry Redekopp, Oussama Safadi, Fokion Egolfopoulos,* and *David Wilcox* who backed our efforts over the past year. We would also like to thank two individuals within the Boeing Company who provided encouragement to begin this project: *Dr. David J. Paisley,* and *Mr. Perry Rea.* Throughout this project we have received funding, as well as feedback and encouragement, from individuals in charge of the Los Angeles Professional Chapter of AIAA and the USC's Office of Undergraduate Research. Among many others we would like to thank *Dr. David Glasgow* at the University of Southern California and the Los Angeles branch of the AIAA chaired by Dean Davis for providing us with the essential funding for this research project to proceed. Last but not least, we wish to give thanks to all our friends and family for being there, providing both an understanding and supportive attitude in a multitude of ways.

May 2010, Los Angeles
USC's Advanced Commercial Concepts Team

Executive Summary:

The next generation of medium range commercial transport aircraft is considered to be the focal point of present-day research in the commercial aviation industry. The expected increase in oil price, the possible introduction of a carbon tax, and stricter environmental constraints have made the development of more efficient and environmentally compatible commercial aircraft necessary to replace the aging fleets of Boeing 737 and Airbus A320. This has created a substantial demand for viable successors to some of the most produced and commercially successful aircraft development projects in the history of aviation. This has resulted in the initiation of significant development in the fields of aircraft propulsion, systems, and structure to ameliorate the shortcomings of conventional configurations in the areas of fuel economy, carbon footprint, and aerodynamic efficiency. Echoing the needs of today's commercial aviation industry, the request for proposal issued by the American Institute of Aeronautics and Astronautics presents challenges, such as an increase in cruise L/D by 25%, use of alternative fuels, incorporation of modern subsystem technology, and utilization of novel configuration concepts to reduce the cost and environmental effects of future commercial transports.

Albatross attempts to address these issues by integrating revolutionary and evolutionary concepts, such as natural laminar flow, bleedless open fan engines that use alternative fuels, fully electric systems architecture, composite load bearing structure, and ultra-high aspect ratio folding wings that provide compatibility with current airport infrastructure while increasing overall aerodynamic efficiency. Using a custom designed open fan engine that reflects projections for state-of-the-art engine technology for 2020, Albatross presents extreme improvements in fuel economy and emission levels produced by the engine; however, as will be presented in this proposal, the rotor diameter and mass properties influence the installation of the engines and therefore determine the general aircraft configuration. As a result, Albatross employs the unique concept of over-the-wing open fan engine installation, presenting significant advantages to alternative methods of engine installation explored in various sources of literature. Emphasis is placed on obtaining a fail-safe configuration that complies with industry and

federal regulations for commercial aviation. In order to support the validity of the assumptions made, highly detailed analyses in the fields of transonic aerodynamics, propulsion, aero-acoustics, and weight were performed and these results were compared to values presented in literature. The resulting design presents tremendous improvements over today's state-of-the-art commercial aircraft technology as a result of integrating these novel concepts into the aircraft. It is realized, however, that by incorporating a substantial amount of new technology, a certain increase in project risk may occur. Efforts are therefore made to ensure that the increase in risk is financially justified and, in case of a delay or failure in any step of the relevant technological development, the adverse effects are minimized, considering both the changes of the future market, speculated to be dominated by aircraft with lower fuel burn, and emission levels, given the ever rising price of aviation fuel and the introduction of a carbon tax in the years to come.

Utilization of open fan engines presents difficulties with respect to far field and near field acoustics and vibration. Special attention is given to identifying techniques in literature that can assist in the reduction of both far field and near field noise while also accounting for weight increments associated with solutions, such as extra acoustic insulation installed to prevent propagation of open fan noise inside the passenger cabin. Given the limited amount of technical information available in the public domain regarding the performance and characteristics of developing open fan engines, such as Rolls-Royce RB-3011, detailed analysis and design work was conducted to create a basic open fan engine configuration with the goal of obtaining weight and performance data for use in the design of Albatross.

Given the performance increase achieved and the relatively high order analytical tools, it is the unilateral belief of the USC Advanced Commercial Concepts (UACC) that Albatross represents a configuration with the greatest potential as a replacement for presently operational, mid-haul commercial jetliners.

Requirements Matrix

Table 1. Selected design parameters

Parameter	Requirement	Albatross	Section
RFP			
Take-Off Distance	8,200 *ft.*	7,300 *ft.*	11.1
Landing Speed	< 140 KCAS	137 KCAS	11.5
Cruise Speed	Mach 0.8	Mach 0.81	13.1
Max Operating Speed	Mach 0.83/ 340 KCAS	Mach 0.84/ 498 KCAS	11.3
Initial Cruise Altitude	>35,000 *ft.*	39,000 *ft.*	13.1
Max Cruise Altitude	>41,000 *ft.*	42,000 *ft.*	13.1
Max Range	3,500 *nm*	3,500 *nm.*	11.4
Nominal Range	1,200 *nm.*	1,200 *nm.*	11.4
Payload Capability	37,000 *lbs.*	37,000 *lbs.*	2.7
Alternative Fuel Capabilities	Compatible	HRJ related algae based biofuel	5,10.1
Passengers	~175	174	2.2,2.7
Seating Pitch	32 *in.*	32 *in.*	2.7
Seating Width	17.2 *in.*	17.2 *in.*	2.2
Cabin Height	>7.25 *ft.*	7.25 *ft.*	2.2
Cabin Width	>12.5*ft.*	12.6 *ft.*	2.2
Cargo Volume	1,240 $ft.^3$	1,410 $ft.^3$	2.2
Materials	Composites 787	Carbon laminated composites	8.1
Cruise L/D	18.2 (737-800) (used as baseline)	23.6	4.7
FAR			
§25.810 & §25.117 Emergency Egress	Emergency door sizing	Satisfied	2.2
§25.903 Blade Loss	1/20 Rule Angular Blade Clearance	Satisfied	5.8
§25.121 Climb Performance	1.2%	1.9%	11.2
§25.111 OEI Climb Gradient	1.2%	1.9%	11.2
§25.105 Transition Phase Climb	2.4%	2.8%	11.2
§25.335 Gust Loading	50 *ft./sec.* max	50 *ft./sec.* max	8.2
§25.925 Propeller Clearance	7 *in.* above the ground	Satisfied	2.6

1. Design Process

1.1 Design Methodology

The general design philosophy of Albatross has been substantially influenced by methodology presented by *Jan Roskam*[1] and *Ed Heinemann*[2]. It should be noted that these methods are often quite extensive and cover technical aspects of the analysis in great detail. The majority of calculations performed and referenced within the proposal use published graphs and tables in order to determine the constants and parameters, often consisting of multiple time-consuming permutations. While the theoretical backgrounds of these methods are discussed in various parts of this proposal, many of the mathematical models and statistical data used in the design process are not presented in their entirety in the interest of brevity.

Design Structure Matrix (DSM), a modern method of development management, was used in order to determine the optimum design process. This method, described by *Eppinger et al.*[3], is used to organize interrelated tasks in the design process in a way that minimizes feedback cycles and determines possible parallel analyses. The PSM 32 code, developed by Blitzkrieg Software, was utilized to implement the DSM in the routine process of developing Albatross. Utilizing this code, the entire design process was re-ordered based on the degree of dependency of each sub-process on the outputs of others. As a result, the design approach presented by *Roskam* has been slightly modified so as to allow for additional parallel processes, as dictated by specific needs of the Albatross' concept, and consequently, improved development speed.

Specific emphasis was placed on addressing particular issues brought on by over-the-wing installation of the engines, as to enable a comprehensive engineering evaluation of all the aspects of this configuration. Issues such as transonic interference between the wing and the engine intake, as well as shock-rotor interferences, were investigated thoroughly to ensure the viability of over-the-wing engine installation. Moreover, complex Computational Fluid Dynamics (CFD) tools were used to verify the feasibility of the acclaimed Natural Laminar Flow (NLF).

2. Configuration Description

2.1 Wing

The wing planform for Albatross has an equivalent area of 1530 $ft.^2$ and a span of 147.1', resulting in an aspect ratio of 14.1. The quarter chord sweep of the wing is 5.9° while the leading edge sweep is 8.1°. The taper ratio of the wing is 0.28, selected to optimize the Oswald's Efficiency factor for the wing at cruise. Choices surrounding planform are driven by aerodynamic trade studies and optimizations that are highly influenced by the concept of NLF. The low sweep of the wing planform, combined with custom designed NLF airfoils, allows for extensive laminar flow (approximately 45%) on upper and lower surfaces of the wing, drastically reducing the friction drag of the configuration at cruise conditions. Sections 4.2 and 4.4 of this proposal present the justification for the NLF characteristics and wing planform optimization, respectively. To further increase the efficiency of the wing planform, a 6' high winglet is canted from the vertical at 15°. The wing planform also features a yehudi from the side of body to the location of quarter the total wingspan, allowing for easier integration of the landing gear. This also increases the local chord of the wing, resulting in a larger internal wing box volume dedicated to fuel tanks. The outboard 19.5' of the wing is capable of folding via an internal electric folding mechanism in order to maintain compatibility with the current worldwide standard gate size of 118' for medium-haul aircraft. Figure 1 presents the wing planform using this configuration.

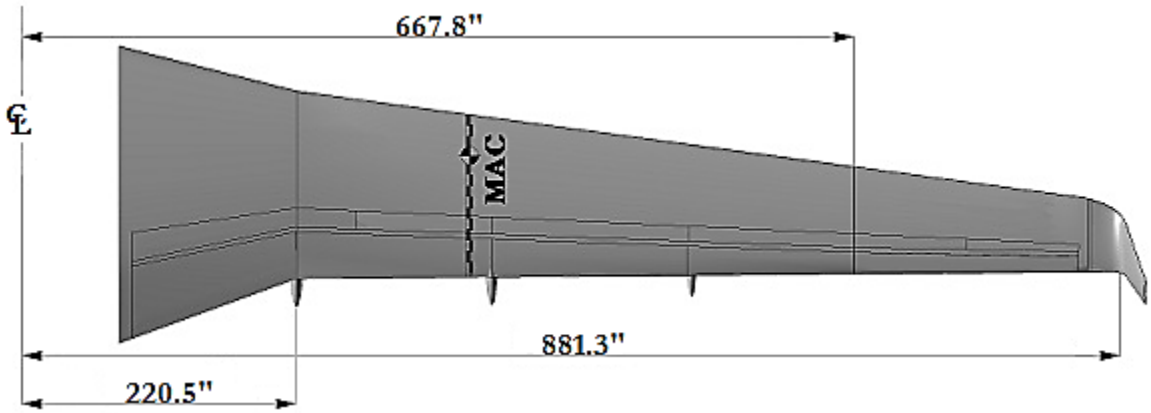

Fig. 1 Wing planform

The wing is equipped with four sets of double slotted Fowler flaps on the trailing edge extending up to 74% of the total wingspan, coinciding with the location of the folding line of the outboard wing. On the trailing edge of the folding section of the wing a flaperon surface extends from the folding line to the inner edge of the wingtip. The wing also accommodates spoiler surfaces that are used for auxiliary control in flight and reducing the speed of the aircraft on the ground.

The trailing edge of the wing features a slight sweep of -0.8° which causes the effectiveness of the trailing edge high lift devices to increase tremendously[4]. To prevent the flow from being tripped by slightly misaligned external surfaces near the leading edge of the wing, no leading edge high lift devices were utilized, as recommended by *Edi* and *Fielding*.[5] The wing structure consists of two main spars passing through the fuselage at 15% and 65% of the chord. Ribs are placed perpendicular to the spars and spaced from 23.5" to 15.2" depending on their span-wise location. The main wing structure is connected to the fuselage through the central wing box which is fixed to reinforced frames and a keel beam inside the fuselage. The fuel is housed inside the wings from the central wing box to the folding line of the wing. The outboard folding section of the wing does not carry any fuel due to the presence of the folding mechanism and complexity of having fail-safe flexible fuel piping throughout this section. The estimated total wing fuel volume is approximately 740 $ft.^3$, resulting in about 5,540 U.S. gallons of fuel. Figure 2 presents the wing structure and high lift systems.

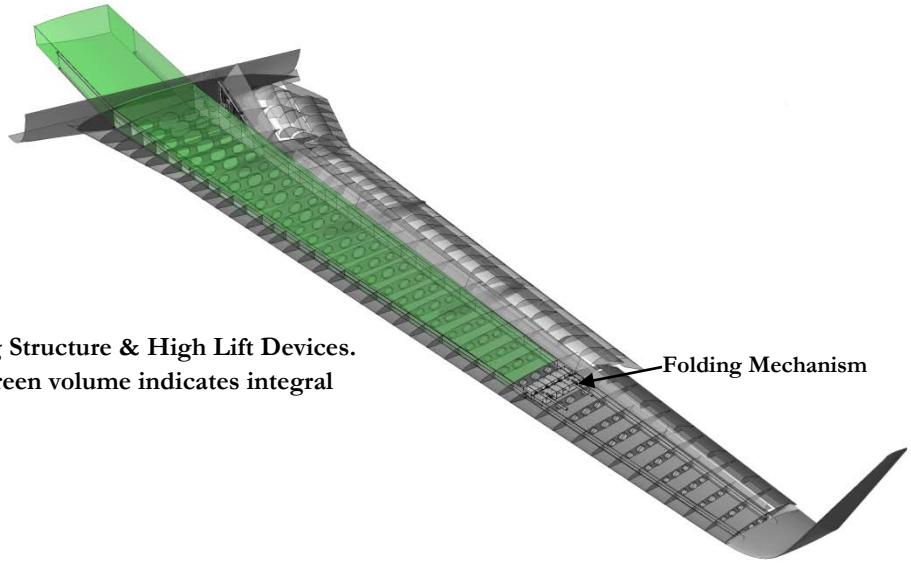

Fig. 2 Wing Structure & High Lift Devices. Note that green volume indicates integral fuel tanks

2.2 Cabin Design

Albatross features an elliptical cross-section with exterior semi-major diameter of 159.4" and semi-minor diameter of 155.5". The pressurized section of the fuselage is 1,372" long and is capable of housing 174 passengers in a single class, single aisle arrangement with a seat pitch of 32" and seat width of 17.2" as outlined by the Request for Proposal (RFP). The interior cross-section designed for Albatross is presented in Fig. 3. As requested in the RFP, the interior dimensions of the cross-section were selected such that after integration of structures and systems, the cabin width is greater or equal to 151" (12.6') and cabin height is 87" (7.25'). The cargo compartment is designed to house containerized cargo with maximum dimensions of 45" x 95". Overhead bag racks are designed to provide 2.7 ft^3 of volume for the passengers in a seating arrangement with a seat pitch of 32". Albatross has the capability of carrying a maximum of 1,410 ft^3 of containerized cargo and 180 ft^3 of bulk cargo on the lower deck.

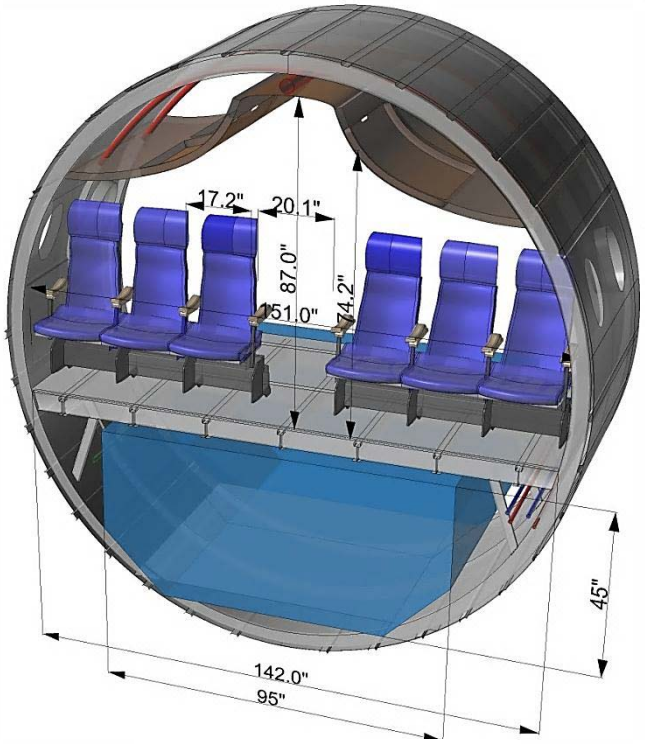

Fig. 3 Fuselage Cross-section

The fuselage is designed based on requirements presented by the Federal Air Regulation (FAR) §25.810 and the amendment §25.117 to this regulation, which requires a 20" clearance row in front of the Type III emergency exits. The main exits and emergency exits designed for Albatross are estimated to support an emergency egress of 247 passengers within 90 seconds from the aircraft, allowing for a further expansion of passenger capacity in case of an increased market demand for an extended version of Albatross.

2.3 Fuselage Geometry

The forebody of the fuselage features a smooth manifold surface with an ESDU Type I top profile[6] and a customized side forebody profile with a bluntness ratio of 0.73. This is mainly driven by the optimization efforts to minimize the pressure drag, as well as increase the extent of laminar flow on the forebody, as will be discussed in Sec. 4.1. The upper sides of the forebody are modified in order to minimize curvature, making the integration of cabin transparencies easier. The forebody possesses an overall fineness ratio of 1.25. The aftbody of the fuselage presents a closure angle of 14^{o} and a fineness ratio of 2.5. The main landing gear is of the tricycle type and is mounted on a gear beam, which is attached to the fuselage and the rear spar of the wing, allowing it to fold into the fairing between wing and fuselage. The fairing size has been kept to a minimum in order to reduce the excrescence and pressure drag.

(a)

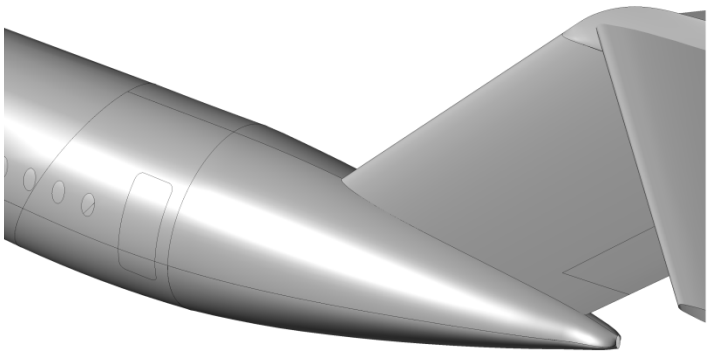

(b)

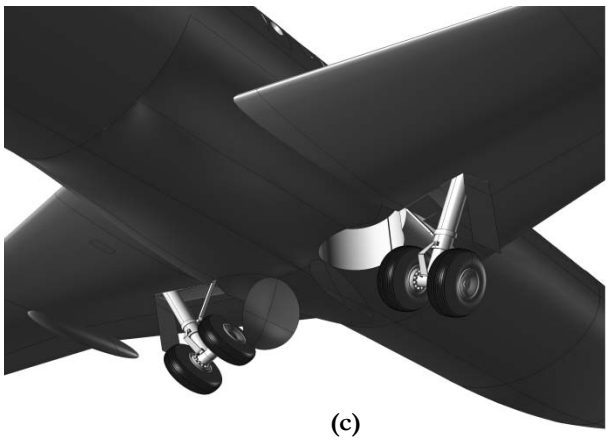

(c)

Fig. 4 (a) Fore body geometry.
(b) Aft body geometry
(c) Wing-fuselage fairing showing the main landing gear folding mechanism and landing gear well.

2.4 Engine Type and Installation

Albatross utilizes a three spool core, geared with two sets of contra rotating, high advanced-ratio, high efficiency propellers with a diameter of 150.6", installed in a pusher configuration. The bypass ratio (BPR) of the engine is estimated, using the GasTurb analysis package, to be around 35. This engine has been designed to demonstrate state-of-the-art open-fan engine technology and therefore uses the published projections with regards to combustor efficiency, compressor efficiency, and turbine inlet temperature. This open-fan engine has been designed to meet the performance requirements set by the RFP and is capable of generating 4,900 lb_f of thrust at 40,000' and Mach 0.8. The requirement, dictated by thrust at cruise, to maintain the maximum speed of Mach 0.83 was the limiting factor in the design of the engine, especially when considering the significant thrust lapse expected as a result of very high BPR. As a result, the engine is designed to be capable of producing 31,500 lb_f of thrust at sea level and static conditions; however, it is recommended that the engine be electronically de-rated to 19,200 lb_f. in order to reduce takeoff fuel burn and noise. Initial weight analysis of the engine indicates a weight of 7,530 *lbs.* which is considerably higher than any comparable turbo fan engines in terms of thrust. Figure 5 illustrates the engine for Albatross. The configuration philosophy of Albatross dictates that such massive fixed items have to be installed near the aircraft's center of gravity so as to allow for the creation of extended versions of the aircraft (to carry more passengers), avoiding a need for increasing the tailplane surface areas or redesigning the wing-to-fuselage joint. Given the large diameter of the propellers, which makes an under-the-wing installation impractical, it was decided to install the engine on a high pylon over and aft of the wing.

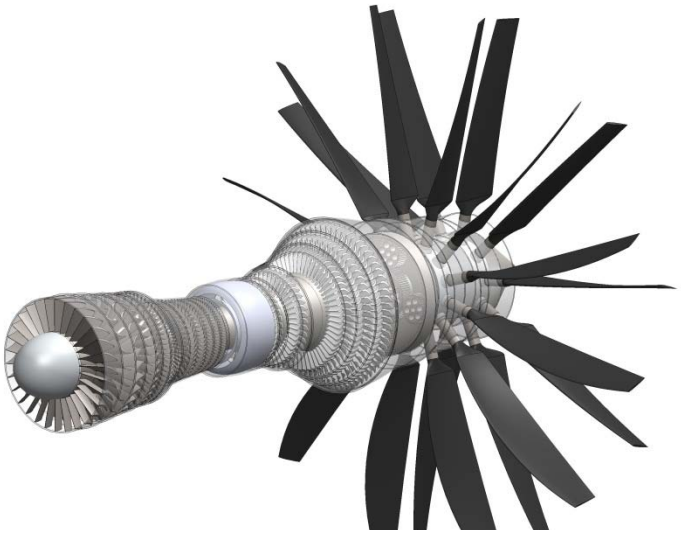

Fig. 5 Open fan engine, pusher configuration

A detailed analysis of the engine and justification for over-the-wing installation is presented in Chapter 5 of this proposal. Figure 6 presents the pylon integration of the engine on the wing.

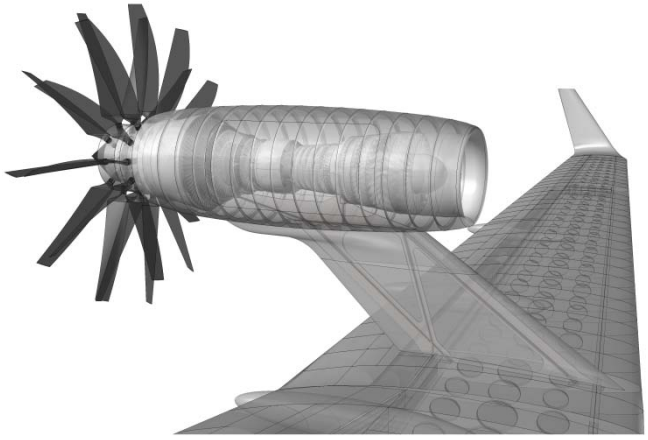

Fig. 6 Engine integration

2.5 Empennage

The empennage of Albatross consists of a T-tail configuration selected to keep the horizontal tail planform away from the intense prop wash produced by the open fan engines. The horizontal tail has a planform area of 342 ft^2 and a span of 36.5', resulting in an aspect ratio of 3.9. The quarter chord sweep of the horizontal tail is 36° while the leading edge sweep is 18.7°. The vertical tail has an aspect ratio of 1.1 and does not feature any taper in order to maximize the tip chord length, therefore maximizing the volume available for the installation of the variable incident horizontal tail on top of the vertical tail. The vertical tail surface is swept aft by 35° to increase the horizontal tail moment arm, effectively reducing the horizontal tail planform area needed to initiate takeoff rotation. The horizontal tail is equipped with elevators on the trailing edge extending up to 93% of the tail span. The structures of the horizontal and vertical tails are conventional, semi-monocoque, composite elements that are fixed on the upper side of the fuselage frames.

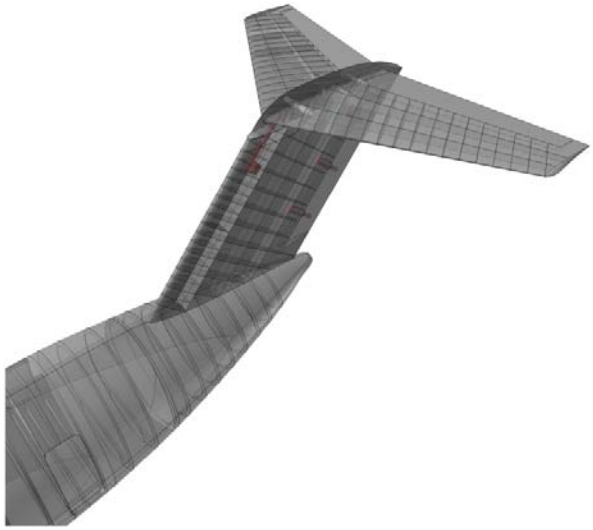

Fig. 7 Empennage and aft body integration of aircraft

Albatross

	Wing	Horizontal Tail	Vertical Tail
Area	1530 ft.^2	342 ft.^2	310 ft.^2
AR	14.1	3.9	1.1
Taper	0.28	0.45	1
C/4 Sweep	5.9 deg.	36 deg.	35 deg.
LE Sweep	8.1 deg.	18.7 deg.	35 deg.
Dihedral	3 deg.	-3 deg.	N/A
Root t/c	11 %	9 %	10 %
Tip t/c	9.5 %	9 %	10 %
Twist	-4 deg.	0 deg.	0 deg.

Values in this table were obtained from trapizoidal simplifications and do not match the geometry shown.

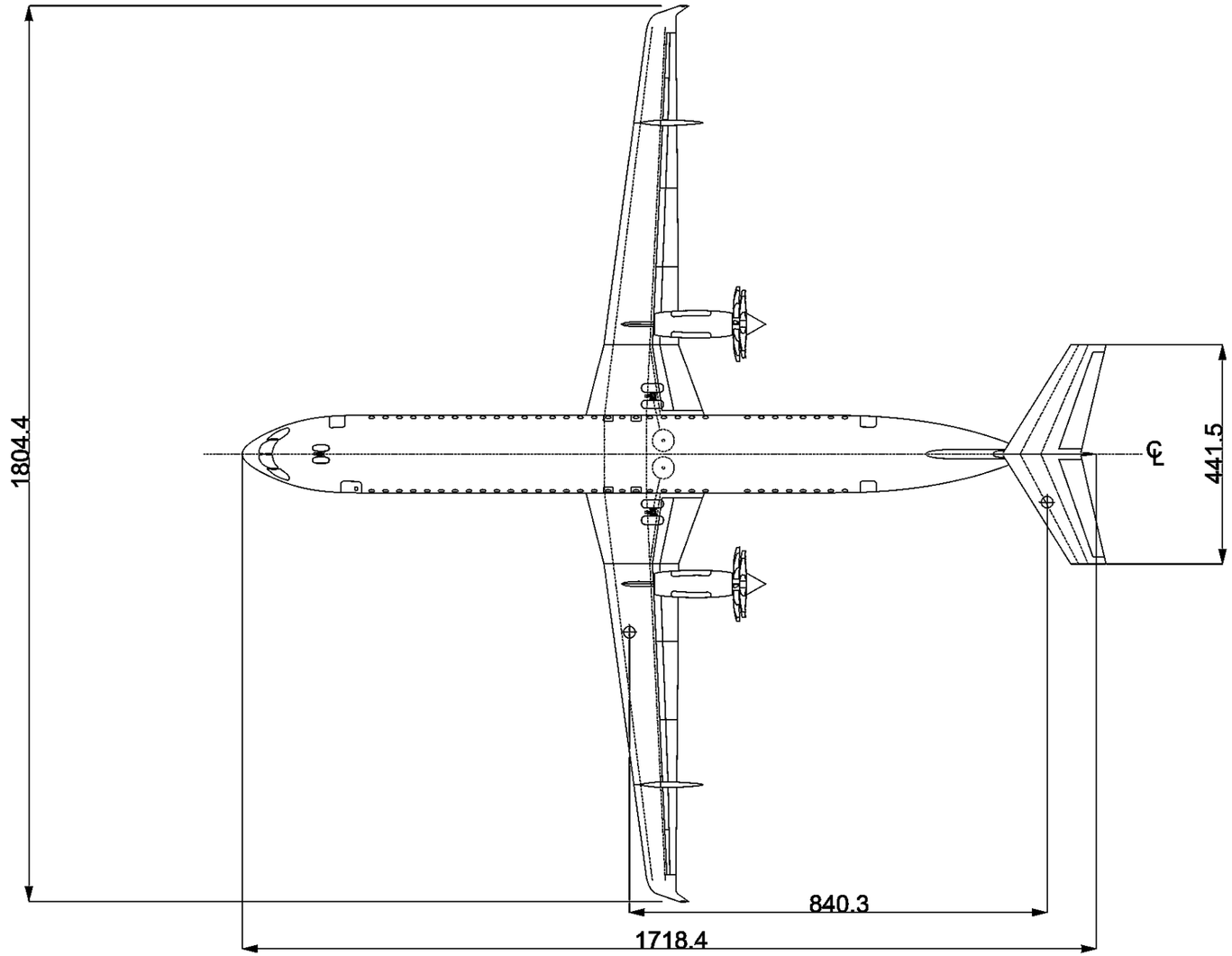

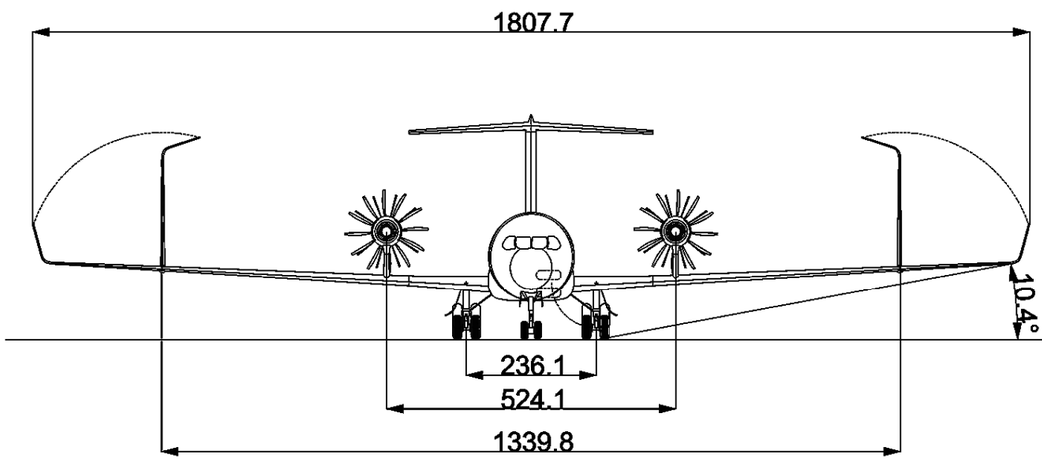

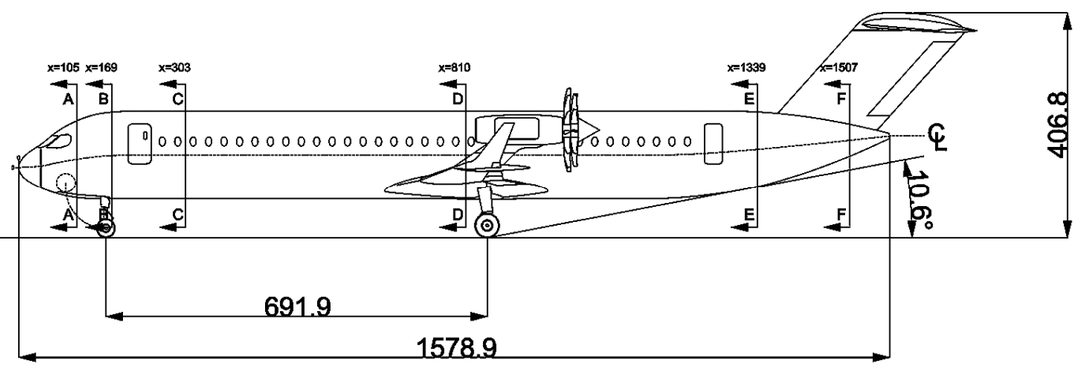

Inboard Profile (Top) and Interior Arrangement of Albatross (Bottom). Views of the interior design of galleys and lavatories are also presented

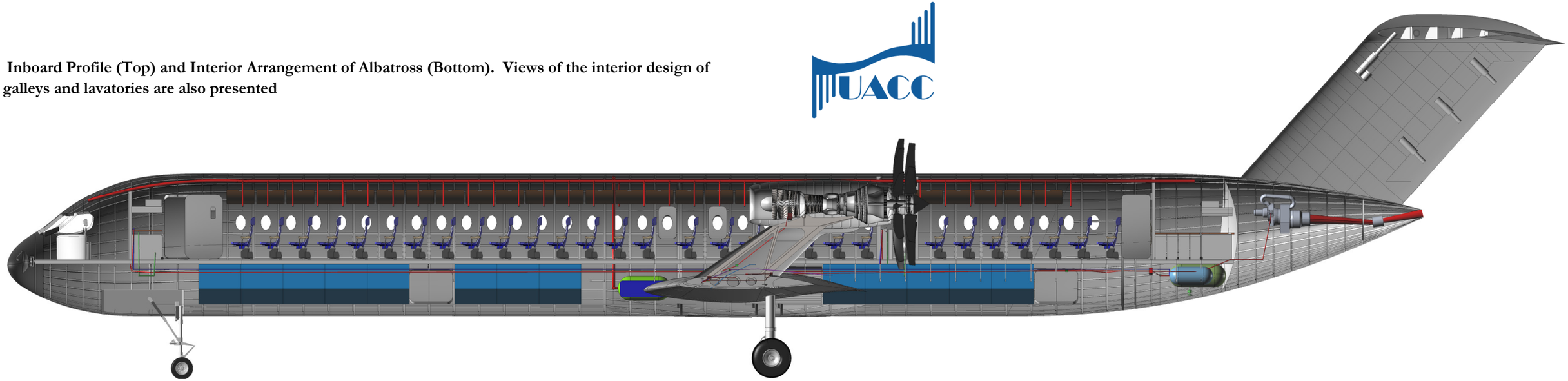

1372"

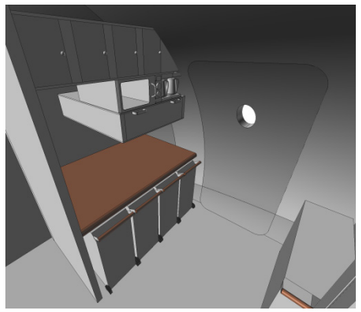

Type B Door
32" x 72"
x = 193"

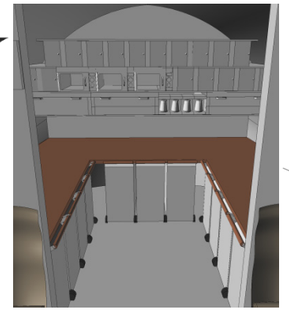

Type A Door
42" x 72"
x = 217"

4 x Type III Exit
20" x 36"
x = 735"
x = 790"

2 x Lavs.

2 x Type B Door
32" x 72"
x = 1260"

1580"

Albatross

3. Sizing

3.1 Initial Laminar Flow Technology Assessment

In reviewing literature relevant to technology developed for high Reynolds number laminar flow airfoils, and in examining studies on delaying the transition to turbulent flow by reducing the leading edge sweep of the wing surface, it was decided that NLF technology will be a viable technology available in the timeframe of 2020. In particular, papers published by *Redeker et al.*[7] and *Lehner et al.*[8] expressed favorable opinions on the availability of NLF technology within the 2020 timeframe. Significant performance improvements are achievable by careful application of these concepts for future aircraft configurations; however, a paper published by *Holmes*[9] suggests that the proposed aerodynamic benefits obtained by application of NLF are limited by the roughness of the manufactured aircraft surfaces. Performing a case study analysis, details of which can be found in Sec. 4.4, to serve as a rough estimate of L/D benefits obtained by having half of the upper surface in laminar flow, it was concluded that an 8% improvement in cruise L/D would serve as a reasonable estimate for the preliminary mission analysis of Albatross[10].

3.2 Mission Analysis and Preliminary Weight Estimations

A typical mission profile was adopted from AIAA[11] and is presented below in Fig. 8.

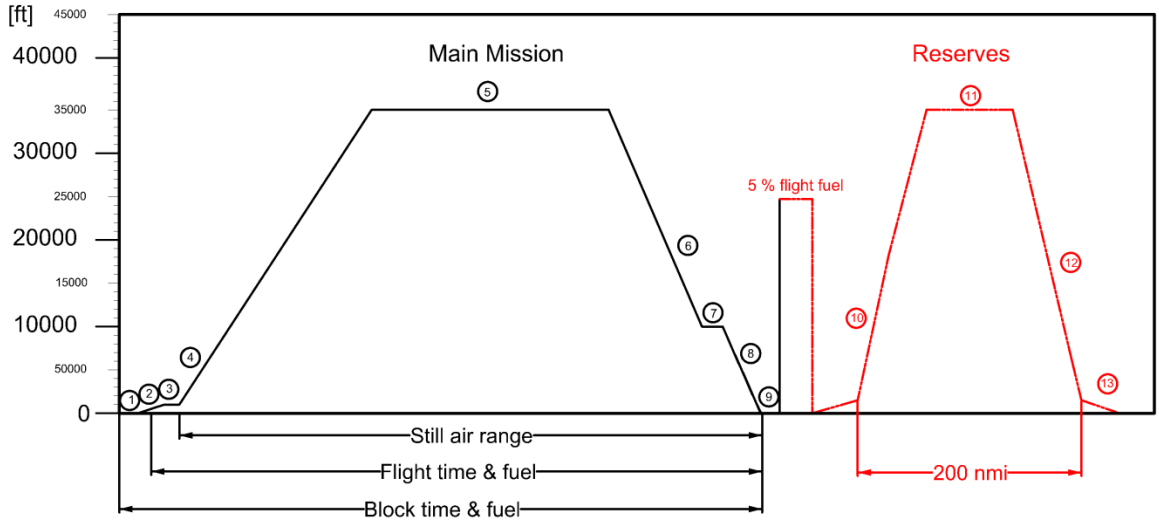

Fig. 8 Mission profile of Albatross. Note that the red portions indicate the reserve mission

Using the methodology presented by ESDU Performance Data Items 73018[12], 73019[13], and 74018[14], combined with *Roskam's*[15] low order statistical weight estimation methods, the mission analysis was performed. Table 2 presents the results for Albatross. It was assumed that the target improvement in L/D specified by the RFP (25%) was obtained and Boeing 737-800 was selected as a comparable baseline airplane for the purpose of this mission study. Considering the use of open fan engine concepts, the specific fuel consumption of the engines was reduced by 35%, as claimed by *Godston & Reyolds*[16].

Table 2. Preliminary Mission Analysis Results.
Note the green segments indicate the reserve mission profile

Mission Segment	Altitude (*ft.*)	Mach	Distance (*nm.*)	Time (*min.*)	SFC (lb/lb-hr)	$\Delta W_{F\,used}$ (lb)
1-Warm up	0	0	0	5	0.19	1,450
2-Taxi Out	0	0	0	4	0.19	1,430
3-Takeoff	150	0.12	0	1	0.23	7,010
4-Climb	1,000-36,000	0.3	33	8	0.31	440
5-Cruise	36,000	0.8	3,500	380	0.46	20,210
6-Descent	36,000-10,000	0.5	33	8	0.31	1,200
7- Loiter	10,000	0.2	0	2	0.28	220
8- Descent	10,000-0	0.2	10	2.5	0.28	1,200
9- Land/Taxi	0	0	0	5	0.19	900
10- Climb	0-15,000	0.3	20	4.5	0.31	207
11- Cruise	15,000	0.5	180	30	0.36	1,290
12- Descent	15,000-0	0.2	50	15	0.31	1,160
13- Land/Taxi	0	0	0	5	0.19	915

Using the weight fractions obtained from *Roskam*[8], as well as the results for the mission analysis, initial estimations for empty, takeoff, and required fuel weight of the aircraft were performed. Table 3 presents the results of this analysis. Note that these results only reflect the statistical trends in commercial aviation and are later refined in Ch. 7 using higher order methods of estimating weight.

Table 3. Summary of initial weight analysis

W_E	74,750 *lbs.*
W_{TO}	149,382 *lbs.*
M_{ff}	0.7842
W_{Fused} (max)	37,632 *lbs.*

3.3 Preliminary Drag Polars

Initial empirical drag polars were obtained using 2nd order regression methods presented by Roskam[17,18] as well as results from the preliminary weight and mission analyses of Albatross. ESDU Performance Data Item 73019[19] was consulted to choose the critical parameters with the highest influence on fuel burn. Three parameters were chosen to determine the optimal lift coefficient for the aircraft when operating at cruise: C_L/C_D, $C_L^{0.5}/C_D$ and $C_L/C_D^{3/2}$. ESDU 73019 suggests $C_L/C_D^{3/2}$ to be maximized, which corresponds to the maximum Specific Air Range (SAR) at a fixed cruise Mach of 0.8. SAR represents the sensitivity of the air range of the aircraft to its takeoff gross weight and, therefore the amount of fuel burned during cruise. As it can be seen from Fig. 9b, the SAR is maximized if the aircraft is operating at a lift coefficient of 0.58, which is significantly lower than the lift coefficient corresponding to maximum L/D (0.79). However, one could observe that the C_L/C_D curve in Fig. 9b is relatively flat around a lift coefficient of 0.58; therefore, the reduction in maximum air range as a result of optimizing the aircraft for maximum SAR is minimal.

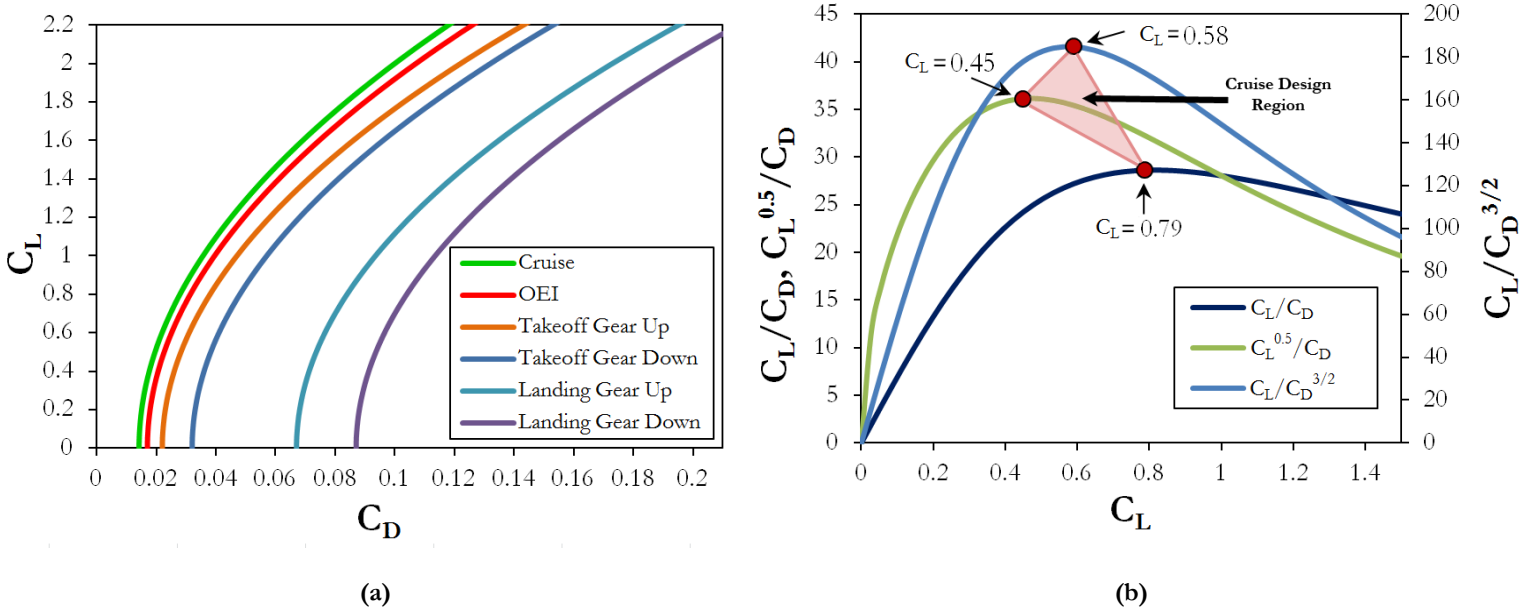

Fig. 9 Results of the preliminary aerodynamic projections. (a) Preliminary drag polars for different mission segments of the aircraft. (b) Parametric analysis of lift and drag data. C_L corresponding to maximum C_L/C_D maximizes the range at constant Mach number. C_L corresponding to maximum $C_L^{0.5}/C_D$ maximizes the range at constant altitude. Parameter $C_L/C_D^{3/2}$ maximizes the SAR of the configurations and was selected based on the recommendations made by ESDU 73019 as a measure of merit, defining a design region for the cruise C_L of the aircraft.

3.4 Performance Sizing

The initial performance sizing of the aircraft was completed based on the performance requirements presented by the RFP, summarized in Table 1, and methods presented by *Roskam*[20]. The wing loading and thrust-to-weight ratios were obtained by solving performance boundary equations. Based on ESDU Aerodynamics 95021[21], it was assumed in this analysis that a maximum lift coefficient of 2.2 is achievable by using stand-alone double slotted Fowler flaps and no leading edge high lift devices. Weight figures obtained from preliminary weight estimates were used in conjunction with lift and drag characteristics obtained from preliminary aerodynamic analysis, which are presented in Sec. 3.2 and 3.3, respectively. A matching plot was constructed by overlaying the performance boundary graphs to identify the acceptable design space for wing loading and thrust-to-weight ratio for Albatross. The result of this analysis is presented in Fig. 10.

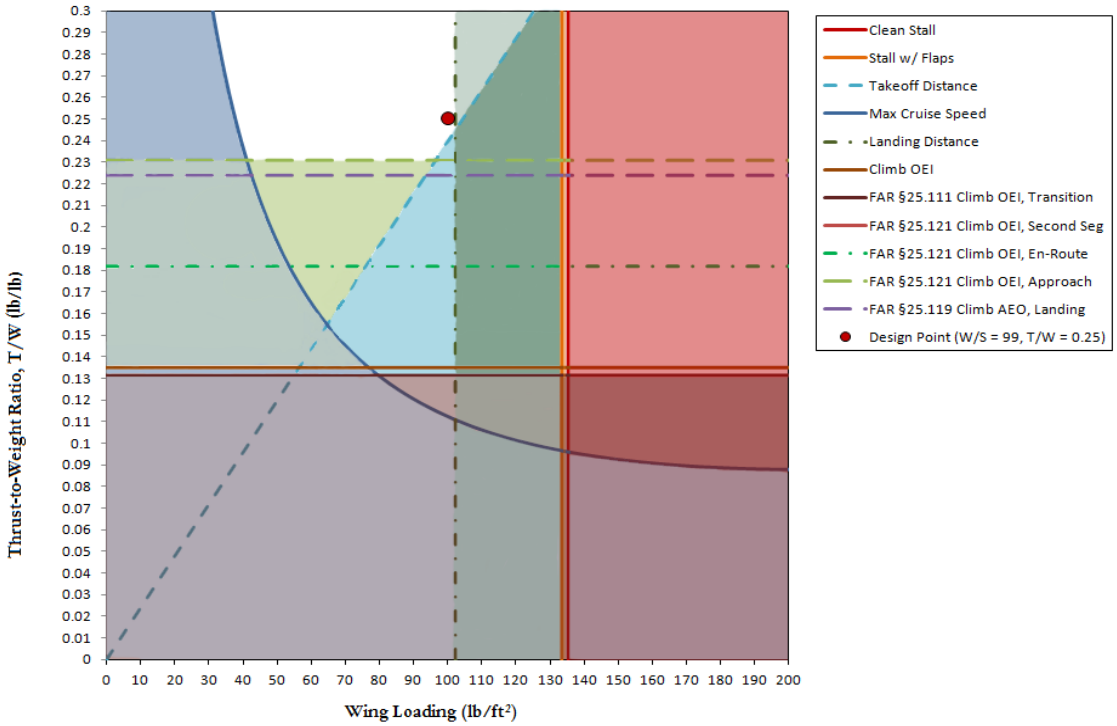

Fig. 10 Preliminary Aircraft Sizing. Design space is indicated by the white area.

As can be seen in Fig. 10, the thrust-to-weight ratio and wing loading of Albatross is limited by the critical performance requirements for takeoff and landing distance. It should be noted that these requirements supersede the climb requirements set by FAR-25 regulations, which is typically the limiting case for aircraft performance sizing in aircraft with typical high-lift devices.

4. Aerodynamics

4.1 Fuselage Forebody Transonic Optimization

To minimize the wave drag of the forebody section of the aircraft, ESDU data item 74013[22] was used to select the optimum length-to-diameter ratio given the maximum cruise Mach number specified by the RFP (0.83). Figure 11 presents the results of this analysis, which indicate that a forebody length to diameter ratio of 1.25 would correspond to a drag rise Mach number of 0.83. A parametric study was performed using the equations presented in ESDU Data Item 83017[23] in order to determine the optimal bluntness ratio that minimizes wave drag penalties on the forebody, the results of which can be seen in Fig. 12. Efforts were spent to maximize the symmetry of the side profile of the forebody, thus maximizing the extent of NLF[24]. A three dimensional CFD analysis was conducted using COSMOS FloWorks in order to investigate the extent of laminar flow on the final forebody geometry, the result of which can be seen in Fig. 13.

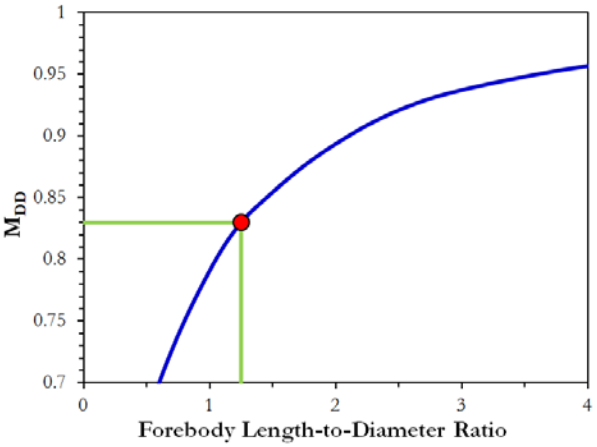

Fig. 11 Drag Divergence Mach Number vs. Forebody L/D

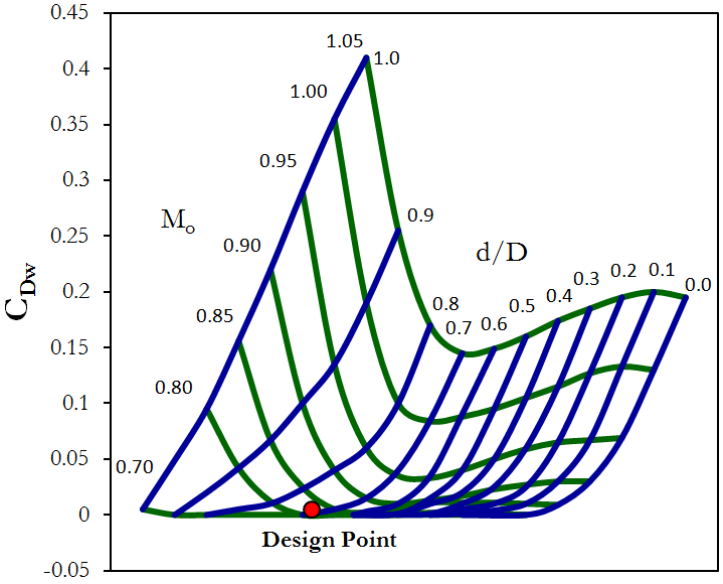

Fig. 12 Forebody Wave Drag Coefficient Vs. Cruise Mach Number (M_o) and Bluntness Ratio (d/D). The bluntness ratio corresponding to the lowest wave drag coefficient was chosen as the design point.

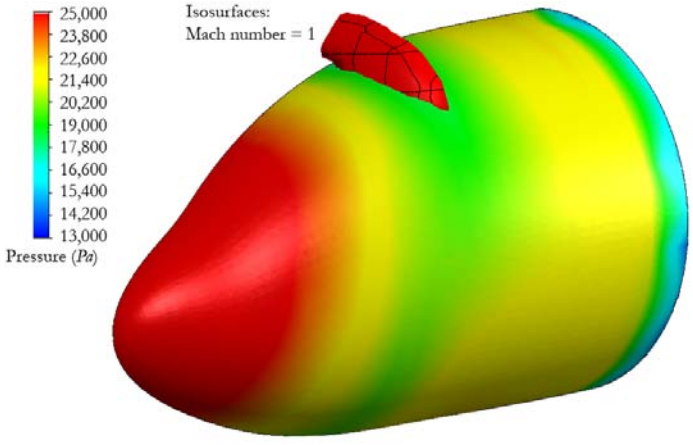

Fig 13 Total pressure contour on the forebody geometry suggests that a favorable pressure gradient is achieved up to the green areas, therefore allowing for possible maintenance of laminar flow. A slight shock is observed on the crown.

4.2 Detailed Analysis of Laminar Flow

Based on the review of general literature, it was decided that laminar flow technologies should be incorporated into the configuration design of Albatross if the substantial 25% increase in L/D required by the RFP is to be achieved. Given the substantial increase in weight and complexity cited for hybrid laminar flow* devices by *Edi* et al.[5], as well as the favorable opinions expressed in regards to the feasibility and benefits of NLF concepts by authors such as *Lee* et al.[25] and *Lehner* [8] et al., the decision was made to incorporate modern NLF concepts into the aerodynamic design of Albatross. Two general strategies were adopted to maximize the extent of NLF. First and foremost, airfoils were to be designed in such a way as to minimize the extent of adverse pressure gradients on the upper surface of the wing, thus extending laminar flow on the wing surface[5]. This strategy will be discussed in Sec. 4.3. Secondly, it was concluded that by implementing a wing planform with very small leading edge sweep, the effects of cross flow instability†, which contribute greatly to the transition to turbulence[5], could be minimized. It is also realized that by reducing the sweep of the wing, one might expect an increase in the compressibility component of the aircraft's drag. Considering the fact that the total drag of a commercial aircraft is dominated by friction components at transonic speeds[26], it can be argued that a tradeoff exists between increasing the sweep of the wing to reduce compressibility drag and decreasing the sweep to increase NLF at the expense of slightly greater compressibility drag. The general consensus in literature is that predicting the location of transition to turbulence is an incredibly sophisticated task requiring complex numerical tools or extensive transonic experimentation, which is beyond the capabilities of UACC. In order to investigate this tradeoff, the analytical method presented by *Lehner*[27] to estimate the transition location for a transonic wing was used. Equation 1 presents the *Lehner* equation that

* Hybrid laminar flow refers to the concept of inducing suction on the upper or lower wing surfaces in order to keep the flow attached and delay the transition to turbulence.

† Cross flow instability refers to transition to turbulence caused by the component of the streamwise flow that travels in the spanwise direction and trips the adjacent flows into increased turbulence levels; therefore increasing the friction drag of the surface.

predicts the Reynolds number corresponding to the chordwise transition to turbulence as a function of leading edge sweep.

$$\mathrm{Re}_{tr} = 24 \cdot 10^6 - \mathrm{atan}\left(\frac{\Lambda_{LE} - 13}{13} \cdot 1.6\right) \cdot \frac{28 \cdot 10^6}{\left(2 \cdot \mathrm{atan}(1.6)\right)} \quad (1)$$

This model was incorporated into the general aerodynamic analysis and used to perform the wing planform optimization, which will be presented in Sec. 4.4. Extensive CFD studies later verified the results for the chordwise percentage of laminar flow obtained by *Lehner*'s equation.

4.3 Airfoil Selection/Optimization

The method for selection of airfoil profiles was dictated by two main elements. First, in order to maximize the extent of NLF on the upper surface, a favorable "rooftop" shape pressure coefficient distribution[7] was sought. Second, the airfoil geometry must be of sufficient thickness to house the wing structure. The limits for thickness-to-chord ratio were set to 15% for root, 11% for mid-planform, and 10% for the outboard wing airfoil. In order to obtain a reasonable baseline airfoil, a study of 30 transonic airfoil geometries, available on the University of Illinois Urbana-Champaign's web portal, was conducted. The airfoils were analyzed using the DesignFoil software on the merit of the maximum extent of laminar flow at C_L 0.58 (selected in section 3.3). From the initial 30 airfoils studied, eight airfoils were selected for the design. Using the eight final airfoils, 40 combinations of upper and lower surface curves were analyzed in order to select the best performing airfoils. NASA Langley's NLF-415 was selected as the root airfoil profile, the BAC NLF airfoil as the upper profile, and the lower profile of RAE 2822 and SC2110 airfoils as quarter span and tip airfoils, respectively. Camber adjustment was performed on the quarter span and tip airfoils to increase their section cruise L/D. CFD analysis using ANSYS CFX was performed to verify the location of transition to turbulence. Figures 14 and 15 present a summary of the results of the transonic CFD analysis performed on the root and tip airfoils.

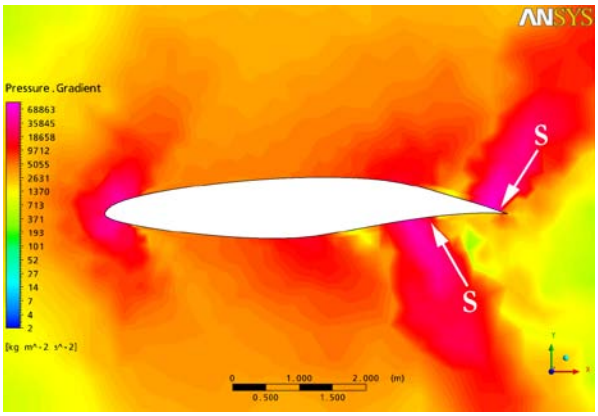

Fig. 14a Pressure Gradient for wing root airfoil

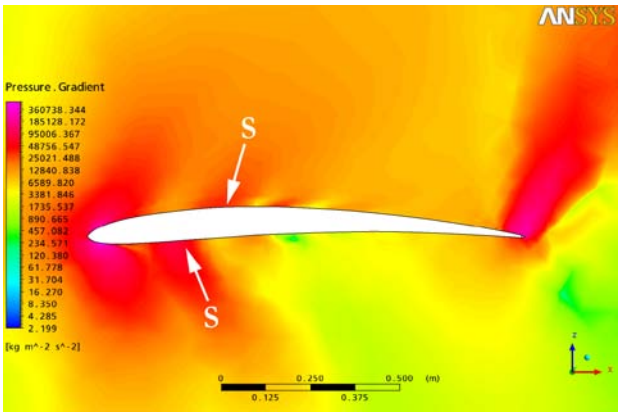

Fig. 15a Pressure Gradient for wing tip airfoil

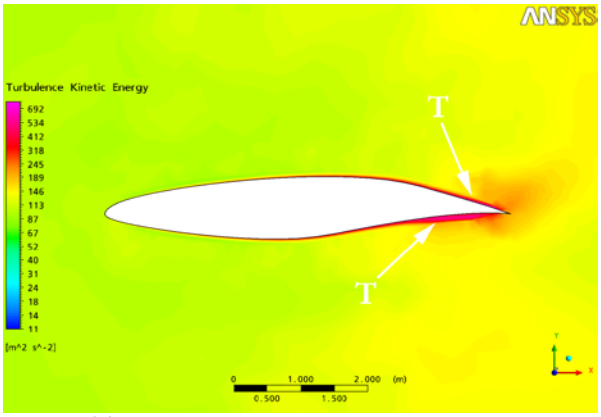

Fig. 14b Turbulence Kinetic Energy for wing root airfoil

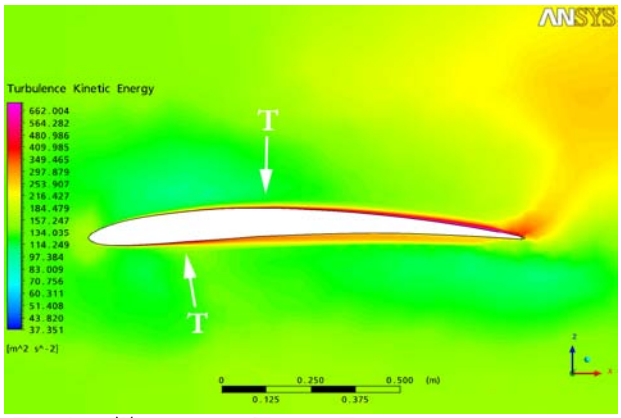

Fig. 15b Turbulence Kinetic Energy for wing tip airfoil

Transonic CFD analyses were performed on tip and root airfoil profiles to determine the location of the transition to turbulence. The analyses are simulating the stream wise flow speed of 0.8 Mach with the ISA atmospheric conditions at 36,000'. The chord length selected for the analysis corresponds to the final wing planform geometry. Pressure gradient contours indicate the existence of normal shocks at points marked by "S" and turbulence kinetic energy contours show transitions locations marked by "T". Averaging the location of transitions on top and bottom sides of the root and tip airfoils yields a 50% laminar flow for the wing.

4.4 Wing Planform Optimization

Based on the NLF method presented in Sec. 4.1, parametric studies were performed in order to obtain the optimal aspect ratio and quarter chord sweep angles that would maximize the L/D of the aircraft, assuming level flight at the cruise condition with a lift coefficient of 0.58. A procedure was developed to compute the percentage of laminar flow on the wing as a function of wing area, aspect ratio, and quarter chord sweep angle using *Lehner's* equation (Eqn. 1).

A parametric analysis was performed by varying the aspect ratio of the wing from 9 to 15 and the quarter chord sweep angle of the wing from 0° to 25°. Considering the results presented in Sec. 4.3, which indicate that an average 50% laminar flow is achievable* (between upper and lower surfaces of root and tip wing profiles), this analysis was normalized to 50%. Figure 16 presents the results of this parametric study.

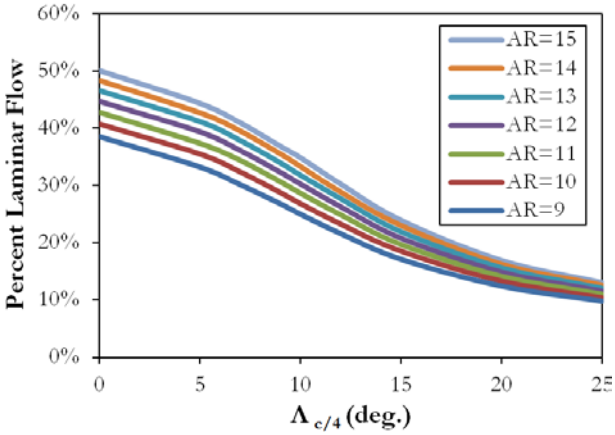

Fig. 16 Extent of Laminar Flow vs. Quarter Chord Sweep of the wing.

In order to perform this analysis, a dynamic configuration file was generated in Advanced Aircraft Analysis (AAA) software. Using the result for the relationship between the extent of the laminar flow and the basic geometry of the aircraft, as well as the inherent geometric and performance sizing capabilities of AAA, a parametric analysis was performed in order to observe the effects of the changes in sweepback angle on the cruise L/D of the configuration. This parametric study was constrained similarly to the laminar flow analysis presented in Fig. 16 so as to preserve consistency. Figure 17 indicates that for any given aspect ratio, there exists an optimal sweep angle that will maximize the cruise L/D. As it can be seen, no particular improvement in cruise L/D is observed as a result of increasing the aspect ratio from 14 to 15; therefore, the aspect ratio was selected to be ~14. The optimal quarter chord sweep angle, accounting for NLF effects, was observed to be ~7-8°.

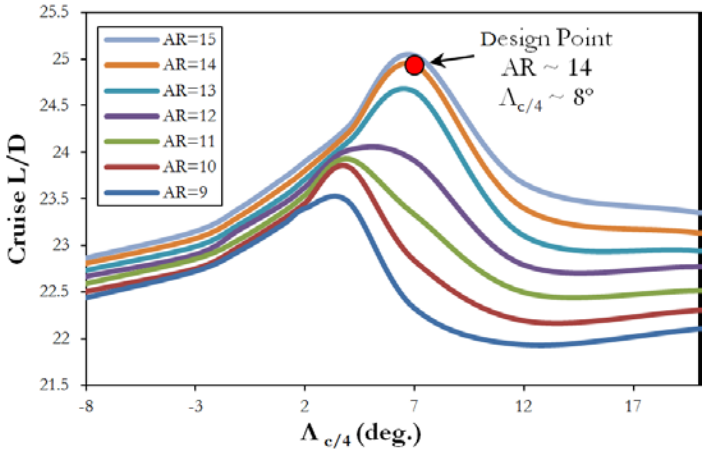

Fig. 17 Parametric study of cruise L/D vs. quarter chord sweep of the wing at various aspect ratios. Design point optimal at AR ~ 14 and $\Lambda_{c/4}$ ~7-8°.

* This result also agrees with the suggestions made by *Lehner*[8] regarding normalization of the percentage of laminar flow on wing surfaces.

4.5 Numerical Verification of Laminar Flow

To ensure that the wing geometry is capable of sustaining laminar flow on its upper and lower surface, two main elements are required. First, a favorable pressure gradient has to be maintained over a significant portion of the wing planform, starting at the leading edge. Second, no shock should exist in the region that laminar flow is expected to be maintained. To verify the capability of Albatross' wing planform to satisfy these conditions, a transient CFD analysis of the flow field around the wing was performed using COSMOS FloWorks for which the results are presented in Figs. 18-20. From this analysis, it was concluded that a favorable pressure gradient (i.e. decreasing pressure in the streamwise direction of the flow) exists on the wing upper surface. The shock on the upper surface does not occur until the 80% chordwise station. The lower surface of the wing is shock free; however, the extent of favorable pressure gradient is smaller than the upper surface

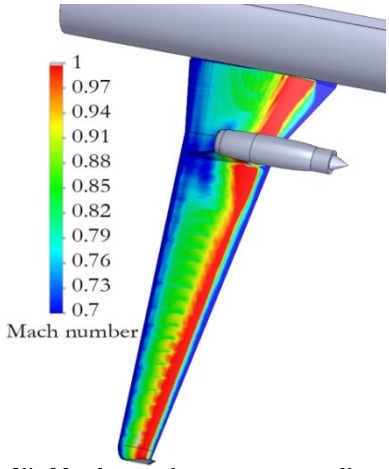

Fig. 18 Mach number contours adjacent to the upper surface of the wing

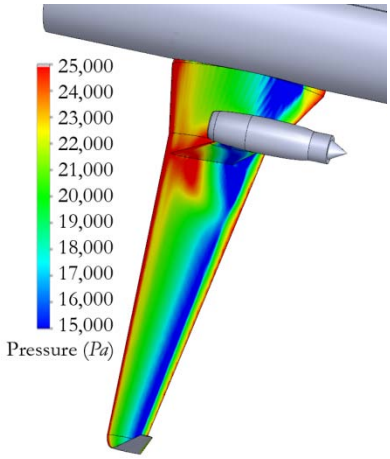

Fig. 19 Pressure contours adjacent to the upper surface of the wing

Figs 18-20 Transient CFD analyses were performed using COSMOS FloWorks on the upper and lower surfaces of the wing to ensure the potential of the surfaces to maintain laminar flow along the chord. The initial conditions replicate ISA atmosphere at a Mach number of 0.8 at 35,000'.

As it can be seen from Figs. 19 and 20, a favorable pressure gradient exists along the chordwise direction on the wing. Figure 18 also confirms that there exist no shocks in the region extending from the leading edge to approximately 85% of the chord.

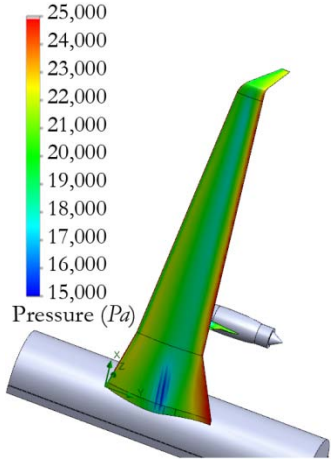

Fig. 20 Pressure contours adjacent to the lower surface of the wing

4.6 High Lift Device Sizing

The strategy to maintain maximum laminar flow on the wing surfaces dictated that no moving part on the leading edge should be incorporated. This led to the decision to incorporate only the most efficient trailing edge devices that can generate a C_{Lmax} of 2.2, as was assumed in Sec. 3.4, given that the flap will extend to 74% of the wing half-span*. Reviewing the ESDU Data Item 95021[21], it was determined that a set of Fowler flaps would generate sufficient lift for this purpose. Using the *Roskam*[28] method for sizing flaps, a parametric study was performed to determine the required flap chord to wing chord ratio that will generate sufficient C_{Lmax} at takeoff. Figure 21 shows the results of this analysis for flaps having a streamwise extent between 15% and 35% of the wing chord. . Efforts were made to define the geometry of the flap segments to ensure attachment of fast moving air to the upper surface of each segment with the flaps deployed. A low speed, transient CFD analysis was used to verify the attachment of flow at landing conditions with a flap deflection of 35°, the result of which can be seen in Fig. 22.

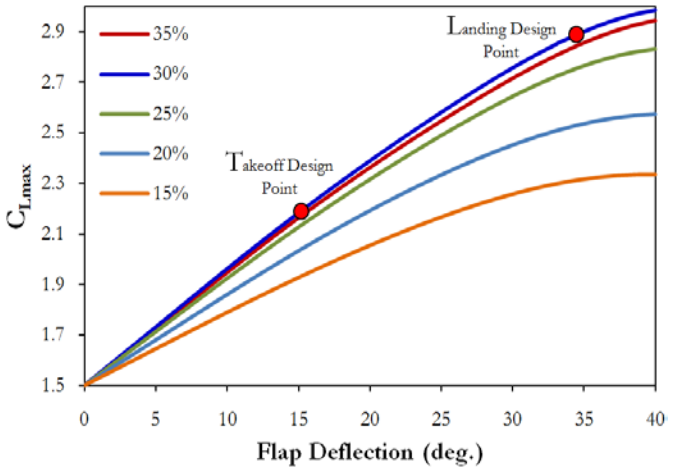

Fig. 21 Aircraft maximum lift coefficient vs. flap deflection for different flap chord to wing chord ratios. The takeoff position of 15° and landing flap setting of 35° is indicated.

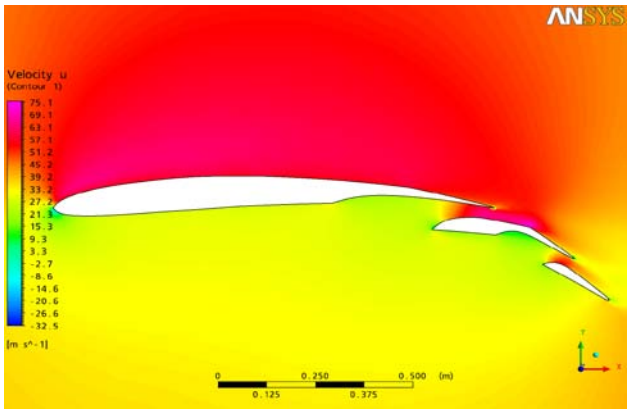

Fig. 22 CFD results for verification of flow attachment for fully deflected double slotted Fowler flap, performed using ANSYS CFX transient CFD model.

From Fig. 21, increasing the flap chord to wing chord ratio decreases the maximum C_L attained by the high lift device system above a flap chord to wing chord ratio of 30%; therefore a 30% ratio was chosen. CFD analysis, presented in Fig. 22, was used to determine the wideness of the slot by performing geometric optimizations.

* As dictated by the location of the folding line on the wing

4.7 Detailed Drag Polars and Breakdown

To obtain a more accurate estimate of the lift and drag forces acting on the aircraft, a more detailed analysis of the aerodynamics of the aircraft was performed using the methods presented by *Roskam*[29]. The methodology used to determine cruise drag polars accounts for compressibility effects by taking advantage of the corrections presented in ESDU Transonic Aerodynamic Data Items[*]. The low speed drag polar methodology is adopted from *Torenbeek*[30]. The results of the CFD analysis related to the verification of the extent of laminar flow on the wing and fuselage, presented in Sec. 4.1 and 4.5, were used to compute the drag acting on the wing and fuselage at transonic speeds. It was assumed that all empennage surfaces would have 15% of their wetted area exposed to laminar flow. Figure 23 presents the results of detailed drag analysis using 5th order drag polar equations, which will be used later in Sec. 11.1-11.6 to verify the satisfaction of performance requirements. Figure 24 presents the drag breakdown of Albatross at cruise conditions.

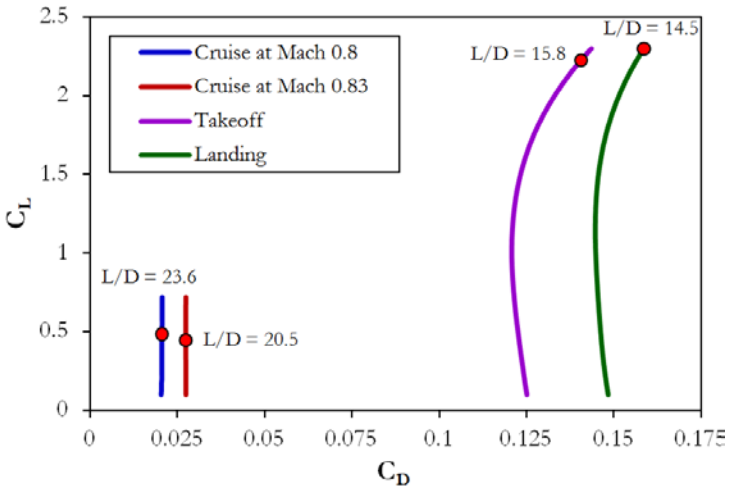

Fig. 23 5th order Drag Polars at Cruise, Max Cruise, Takeoff, and Landing Conditions.

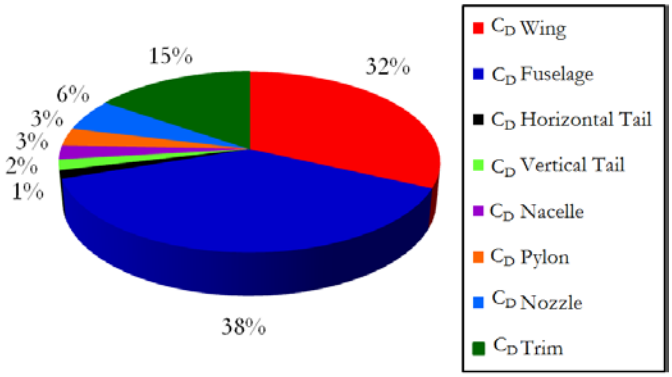

Fig. 24 Drag breakdown at cruise.

The drag polars for cruise and max speed conditions are computed using 5th order methodologies for a range of lift coefficients from 0.1-0.75. Higher lift coefficients were deemed unnecessary for cruise conditions. The lift coefficients selected for cruise, max speed, takeoff, and landing are 0.48, 0.46, 2.2, and 2.3 respectively. From the drag breakdown at cruise, it is observed that the drag of the wing constitutes 32% of the drag for the entire aircraft. This number is substantially lower than the conventional 50% wing drag at cruise, due to the utilization of NLF.

[*] The following data items have been used: 6407, 71019, 79004, and 83017

4.8 Drag Rise Characteristics

Given the low wing sweep resulting from planform optimization, it was critical to verify the drag divergence Mach number (M_{DD}) of the configuration. Drag rise analysis was performed using the method presented by *Roskam*[31]. The M_{DD} was defined as the Mach number at which the rate of change of total drag of the aircraft exceeds 0.1. Figure 25 presents the results of this analysis.

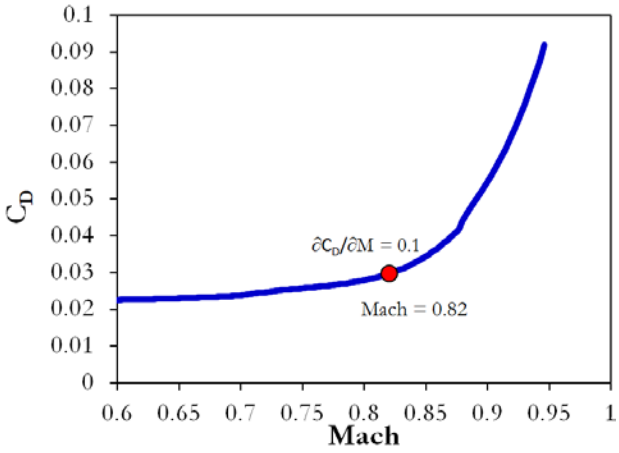

Fig. 25 Result of drag divergence analysis on Albatross indicating a M_{DD} of 0.82, according to the criteria of $\partial C_D/\partial M$ of 0.1.

4.9 Drag Verification

To verify the accuracy of the methodology used to model the high speed drag of Albatross, experimental data was obtained with regard to the high speed aerodynamic performance of the DC-10-40[32]. This data was compared to the results of a case study analysis of the DC-10-40 using the drag estimation methods of Albatross. Figure 26 presents this comparison. As it can be seen, the drag polars intersect in the neighborhood of $C_L = 0.5$, indicating the agreement of *Roskam*'s method with experimental data at typical cruise lift coefficients.

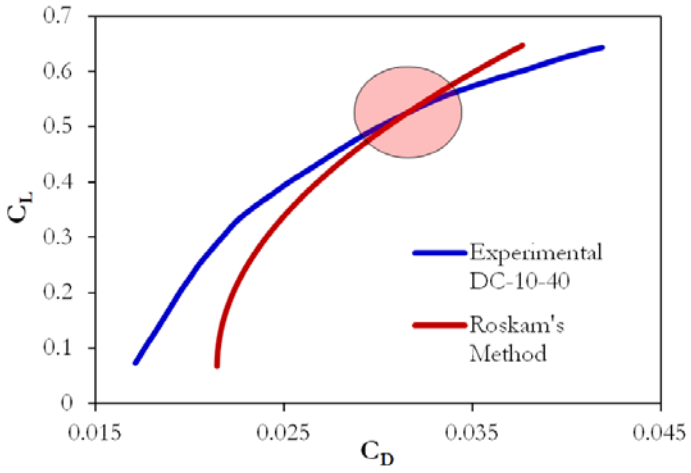

Fig. 26 Comparison of experimental data regarding the lift and drag characteristics of the DC-10-40 with results obtained by applying Roskam's method to estimate drag.

5. Propulsion

5.1 Engine Technology Tradeoff

Albatross' propulsion system was especially designed to satisfy the RFP's guidelines regarding environmental footprint, fuel burn, and aircraft operating cost. Two main available propulsion technologies were explored during initial configuration design: geared turbofan and open fan engines. Modern turbofan technologies, including geared turbofans such as the Pratt & Whitney PW1000G and direct drive fans such as CFM's LEAP-X, were explored to observe their benefits and drawbacks. Advanced turbofan technology presents fewer development risks within the timeframe set by the RFP[33], but arguably represents today's propulsion technology rather than that of an aircraft entering into service in 2020.

Open fan engine concepts, which are considered novel at present, have been under development since the early 80's and may be service ready by 2020. Furthermore, there exists a business case for the implementation of such engines due to their tremendous potential to reduce specific fuel consumption[33]. Although open fan concepts promise significant reductions in fuel burn and emission levels, they present a new set of issues that need to be addressed if such propulsion concepts are to be used in the near future. According to *Holste&Neise*[34], the novel arrangement of these engines introduces new sources of acoustic disturbance which contribute greatly towards an increase in noise levels. The potential to have low noise open fan engines has been greatly increased by advancements in aero acoustics, acoustic blade treatment[35] and rotor induced broadband noise[36]. Takeoff and landing trajectory optimization has also been suggested as a viable method to reduce open fan noise by increased climb and descent gradients, therefore maximizing the effect of atmospheric attenuation on the engine noise[37].

Aside from acoustic concerns, the size and weight of these engines are believed to cause engine design and integration issues in the configuration design. Given the large propeller diameters historically associated with open fan concepts, locations for engine installation have been limited to

the rear fuselage. This concentrates a substantial portion of the empty weight of the aircraft at the rear end, causing the CG of the empty aircraft to be fairly aft. Subsequently, the wing has to be relatively far aft, causing the CG of the freight and payload (i.e. passengers) to be located significantly ahead of the CG of the empty aircraft. This causes a large range of CG travel, making a modular expandable aircraft design (in terms of payload capacity) financially infeasible[*,38]. Considering that, historically, all preceding medium range aircraft have been expanded over time to create larger versions of the baseline aircraft according to market needs, UACC has identified the integration/configuration design of an open rotor engine is the most critical to the conceptual design of the aircraft. This proposal presents the details of the over-the-wing engine installation method, which offers potential for further configuration expansions.

While resolving structural/weight distribution issues experienced with the aft-mounted, open fan engine installation, over-the-wing installation presents a new set of issues, mostly pertaining to the high speed aerodynamic interferences between the nacelle/rotor assembly and the wings. Given the configuration design benefits obtained by utilizing wing-mounted, open fan engines and considering the tremendous reductions in fuel burn and emission levels offered by the open fan engine concepts, UACC chose to develop an open fan engine configuration in sufficient detail, mimicking the present day developments undergone by the Rolls-Royce Company for their RB-3011 engine. It was necessary to develop the engine configuration with a substantial level of detail in order to enable the full evaluation of the technical questions regarding engine thrust lapse performance and weight penalties associated with both the engine/transmission module and structural integration of the engine.

[*]This is caused by a need to redesign a larger empennage as the length of the fuselage and the passenger capacity is increased in later models. This is not only extremely costly for the manufacturer, but it may also reduce the aerodynamic efficiency of the aircraft as a whole since larger tail planforms cause significant increases in drag, therefore diminishing the fuel economy of the baseline aircraft.

5.2 Engine Core Design

Following the on-going trend in the core size of modern high BPR, turbo fan engines*, a three spool core configuration was selected for development. Three spool configurations allow for an increase in compressor stage efficiency by allowing each stage to operate at its optimal RPM. Under cruise conditions, GasTurb was used to perform detailed analyses of various engine core designs and optimizations in order to minimize fuel burn, NOx emissions, and the core diameter of the engine. Assuming that the turbine inlet temperature is limited to 1,440 *K* (2,140 °*F*), modern technology can achieve burner efficiency of 0.9995[39], which was applied to the design of Egret's engine. The mechanical efficiencies of the three spools were assumed to be 0.997, 1, and 0.995 for the high, intermediate, and low pressure spools respectively[40].

A GasTurb geometric model was constructed and a detailed analysis of the engine core was performed to obtain a basic cycle for the core as shown in Fig.27. Due to a lack of statistical information regarding the weight and mass distribution characteristics of an open fan core, generic compressor and turbine blade profiles were used to construct a parametric CAD model of the core, allowing weight and mass characteristics to be estimated. Figure 28 presents the cross section of the CAD model, as well as the turbo-mechanical model produced by GasTurb.

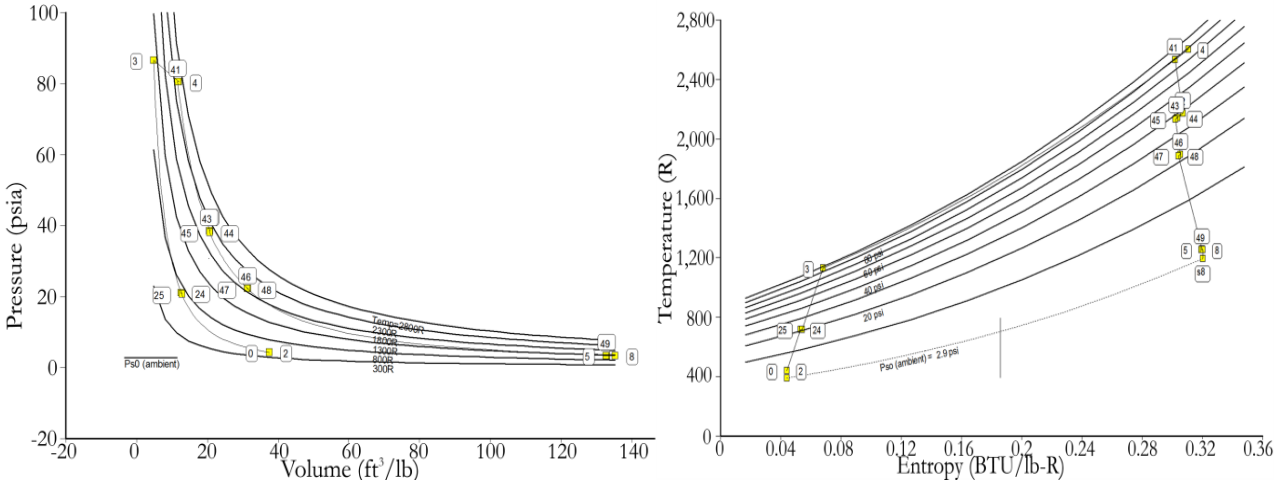

Fig. 27 T-S (Left) and P-V (Right) Diagrams for core cycle.

* Modern high BPR, turbo fan engines, such as Rolls-Royce Trent 1000, employ a three spool configuration to increase the efficiency of each compressor stage.

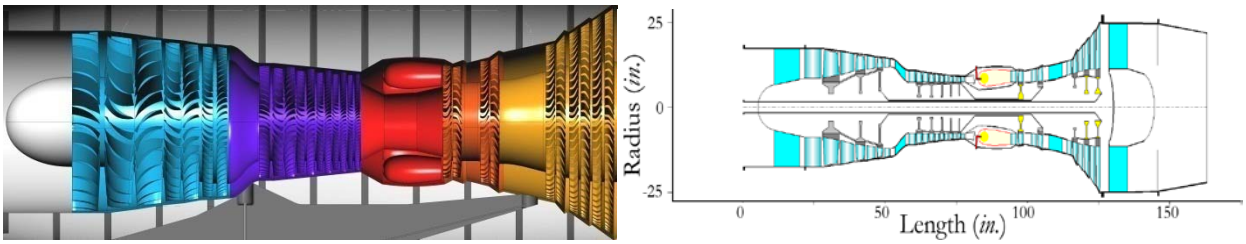

Fig. 28 CAD model cross section (Left) and GasTurb Core Configuration (Right).

5.3 Rotor Power Transmission Design

A large rotor diameter was selected to obtain a high BPR for the engine. Analysis shows that this large rotor provides the majority of the engine's thrust, while only a small contribution is produced by the core stream as will be discussed in Sec 5.6. UACC decided that a contra rotating system would maximize the rotor propulsive efficiency by minimizing net flow circulation. The two main methods to achieve such a system are a direct drive turbine stage and an epicyclical gearbox. The simpler method utilizes two contra rotating turbines to directly drive each rotor stage. While this system operates optimally at cruise RPM, such a system is not as efficient at other flight conditions such as takeoff because of differing exhaust flow velocity. However, an epicyclical gearbox utilizes a series of gears to generate contra rotating torque and therefore its efficiency is constant and does not depend on the exhaust flow of the turbine. Considering this tradeoff, an epicyclical gearbox system was chosen to create the required contra rotating motion, extracting power from a traditional low pressure turbine shaft as shown in Fig. 29. Analysis using GasTurb indicates that the turbine exhaust temperature will be approximately 700 *K* (800 °*F*), which is sufficiently cooled to substantiate the design of a heated structure for a blade root mechanism using high strength, heat resistive steel alloys[41].

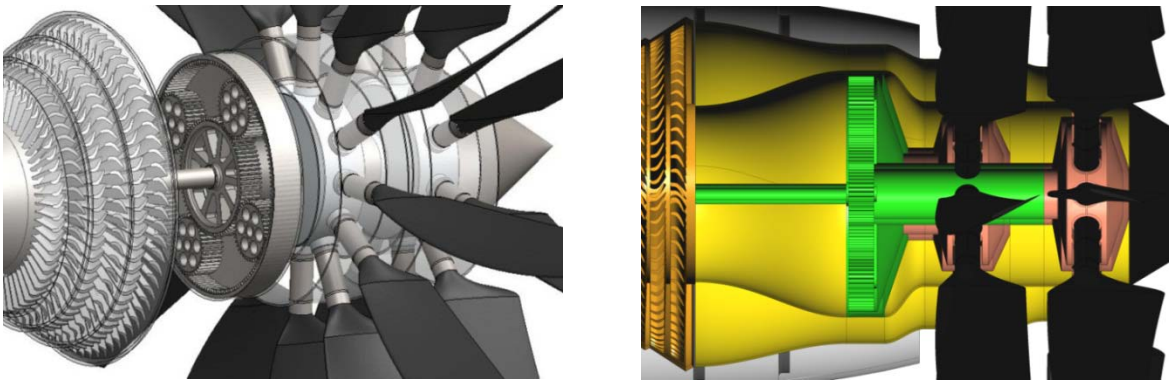

Fig. 29 Isometric view (Left) and cross section view (Right) of integrated epicyclic gearbox.

5.4 Bleedless Architecture

As stated by *Collie et al.*[42], the fuel burn of high BPR, small core engines can be significantly reduced by eliminating their bleed air system. Removing this system from the high pressure compressor stage can significantly improve the local compressor efficiencies. Analysis using GasTurb was used to model the effects of the variations of the overboard bleed mass flow on the TSFC of the engine, the results of which can be seen in Fig. 30. By reducing the overboard bleed mass flow from five to zero *lb/sec*, the TSFC varies significantly from 0.485 to 0.454 *lb/(lb-hr)* (causing a 6% reduction). Because of this substantial reduction in TSFC, a bleedless architecture was integrated into Albatross.

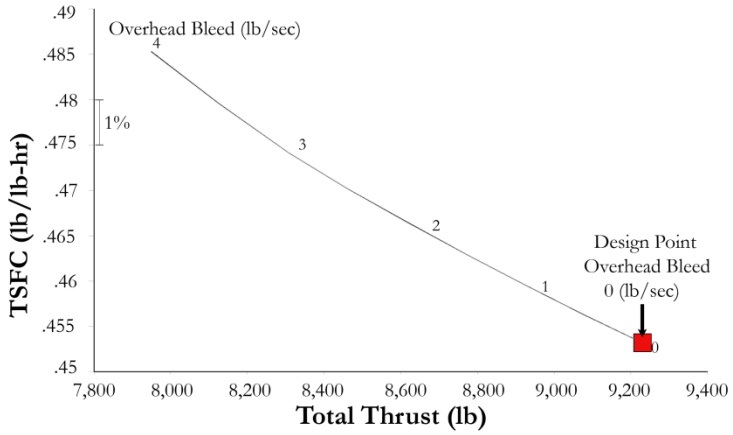

Fig. 30 TSFC vs. total thrust at mass flow overhead bleeds from four to zero *lb/sec*. Design point suggests minimal TSFC at no overhead bleed

5.5 Engine Optimization

To determine the design parameters that have the most significant effects on the engine's TSFC and NOx emission levels*, a sensitivity analysis was performed using GasTurb, varying a number of engine design and operational variables. Table 4 presents the results of this analysis.

Table 4. Sensitivity analysis results.

Design Parameter	Basis	ΔBasis	ΔTSFC	ΔNOx Intensity
Burner Exit Temperature *[°R]*	2605	+10, -10	+0.10, -0.08	0.00, 0.00
Burner Press. Ratio	0.93	+0.01, -0.01	-0.33, +0.35	0.00, 0.00
Compr. Interduct Press. Ratio	0.985	+0.01, -0.01	-0.31, +0.33	+0.40, -0.41
Altitude *[ft.]*	39,000	+100, -100	0.00, 0.00	-0.19, +0.19
Mach Number	0.8	+0.1, -0.1	+8.73, -9.48	+14.31, 0.00
Prop Diameter *[ft.]*	12.5	+0.1, -0.1	-0.48, +0.60	0.00, 0.00

* NOx intensity levels are measures of emissions that will be discussed in Section 5.11 of this proposal.

As shown in Table 4, some design parameters can increase TSFC while decreasing NOx intensity, and vice versa. Accordingly, it would be beneficial to optimize those parameters that only influence either the TSFC or NOx intensity, independently of each other. A multivariable optimization using a Monte Carlo selection strategy was employed to find an optimal combination of the previously mentioned parameters. The restrictions placed by the RFP on cruise Mach number and altitude for which the engine is to be designed were also considered in this optimization. According to this analysis, the cruise altitude should be maximized while the cruise Mach number should be minimized in order to minimize NOx intensity. Additionally, the prop diameter was found to have the largest effect on TSFC and NOx intensity, and therefore was maximized. This maximization was limited by sonic velocities on the propeller blade tips. Therefore, a diameter of 12.5' was selected. These aforementioned engine parameters were chosen for the optimization since the sensitivity of TSFC and NOx intensity values was higher than the other parameters considered.

5.6 Engine Analysis

Open fan engines' performances are best modeled by a turboprop engine with a modified propeller map due to their high BPR and turbine-driven core. Using a sample propeller map presented by *Grieb et al.*[43], a generic, eight blade, high efficiency propeller map was scaled to obtain a power coefficient of 1.0 and an advance ratio of 1.8 at a propeller efficiency of 0.9 at cruise. This propeller map generated by GasTurb (Fig. 31) was used to analyze the engine's performance. From the analysis, it was determined that 9,030 *lbs.* (98%) of thrust was generated by the propeller, while only 200 *lbs.* (2%) of thrust was generated by the core. As was previously mentioned, open fan engines present particularly high thrust lapse* characteristics,

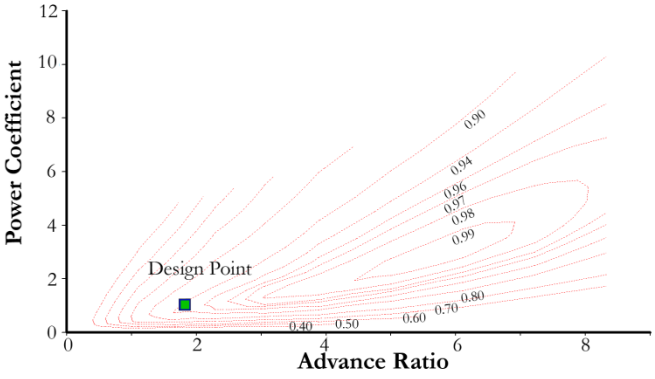

Fig. 31 Propeller map used for engine performance analysis

* Thrust lapse refers to reductions in the available thrust of the engine as altitude and Mach number increase.

resulting from a high BPR, which leads to cruise altitude and Mach number becoming the engine's limiting factor. Using the limits of a Mach number of 0.8 and cruise altitude of 39,000', in addition to the computed drag polars, the engine geometry was optimized to provide the required thrust at those conditions. The engine performance evaluation was repeated to obtain a full engine map characterizing TSFC and available thrust, assuming a 250 *kW* mechanical power offtake. Figure 32 presents this engine map.

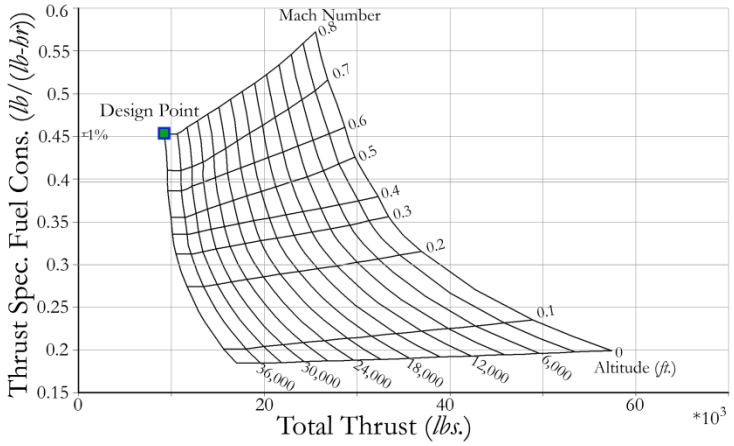

Fig. 32 Engine map used for engine performance analysis. Net thrust of the plane is multiplied by 2 to account for two engines on the Albatross

As seen in Fig.32, in order to maintain sufficient thrust at cruise, the takeoff thrust of the engine is significantly higher than comparably-sized aircraft, such as the Boeing 737[44]. Therefore, in order to decrease fuel burn and reduce noise, the engines installed on the aircraft may undergo automated derating* depending on operational altitude and speed.

5.7 Engine Integration

As discussed in Sec. 2.4, the integration of the open fan engine is a significant element in the configuration of Albatross. In order to effectively integrate the engine, a weight analysis was performed based on parametric CAD models created for the engine. From these, the weight of the engine determined by GasTurb was found to be 7,400 *lbs.*, of which 5,500 *lbs.* belong to the engine core and 1,900 *lbs.* belong to the power transmission and rotor system. A mass distribution analysis

* Derating refers to the reduction of the maximum available installed thrust of the engine by electronically imposing limitations on the fuel flow of the engine.

also indicated that the CG of the core-rotor system is located 49% behind the reference point of the engine, which is fairly aft of the well-established 40% convention for turbo fan engines[45]. The open fan engine concept developed for Albatross (mimicking Rolls Royce RB-3011) is considerably heavier than turbo fan engines of the same thrust class. This increase in weight presents difficulties in terms of the structural design of the pylons, as well as the adjacent structure on which the pylons are to be attached. A double spar stabilized pylon was designed in order to install the engine over the wing. Figure 33 presents the designed structure, confining the geometry of the pylon to a NACA 0009 airfoil.

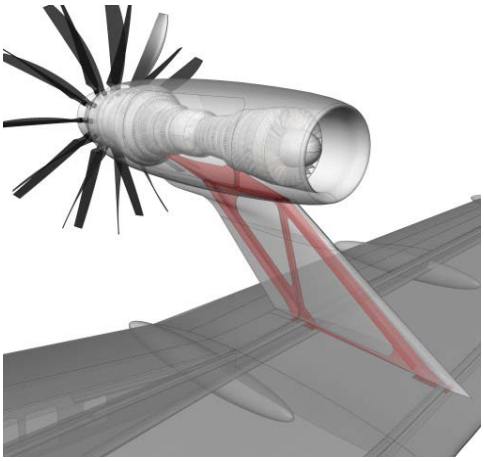

Fig. 33 Engine integration for over-the-wing installation performance map

This weight of the pylon structure was minimized by performing finite element analysis accounting for the weight of loads imposed by the mass of the engine and inertial loads from a 2-g pull-up, including simultaneous maximum thrust. Figure 34 presents the final results of the finite element analysis showing contours of factor of safety (FOS) and maximum displacement (URES).

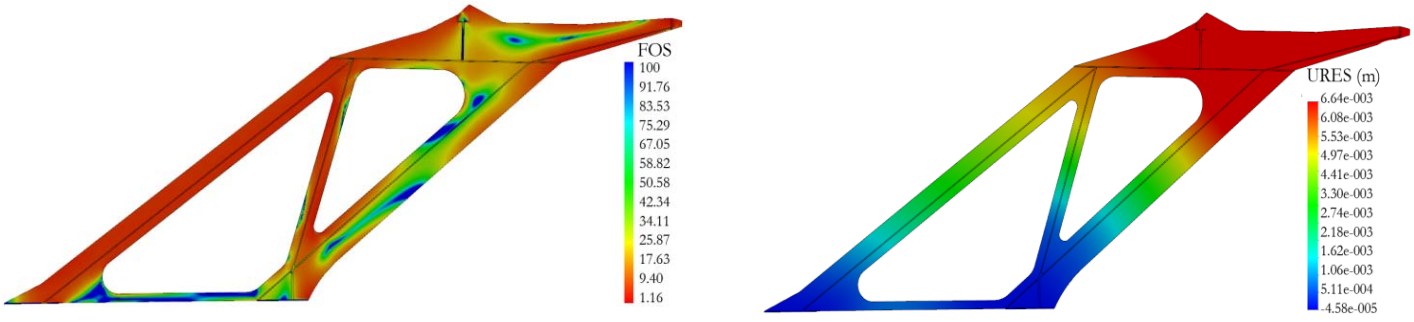

Fig. 34 FEA of wing mounted engine pylon showing contours of factor of safety (left) and maximum displacement (right)

To assess the possible structural weight benefits obtained by using an over-the-wing engine installation, a comparative study was performed by designing and analyzing a comparable pylon supporting an aft-mounted open fan engine. Using ESDU Data Item 79020[46], it was determined that a 34" blade clearance from the fuselage would be sufficient to offset the fuselage boundary layer in

order to avoid the interference of low energy boundary layer with the fan tips. This structure was designed using the same constraints as the over-the-wing installation and similar FEAs were performed, the results of which are shown in Fig. 35. The mass properties analyses indicate that the aft-mounted pylon will have a total weight of 1,090 *lbs.* while the over-the-wing installation will weigh 490 *lbs.* This case study indicates a significant structural weight reduction obtained by loading the pylon structure in compression as opposed to bending*.

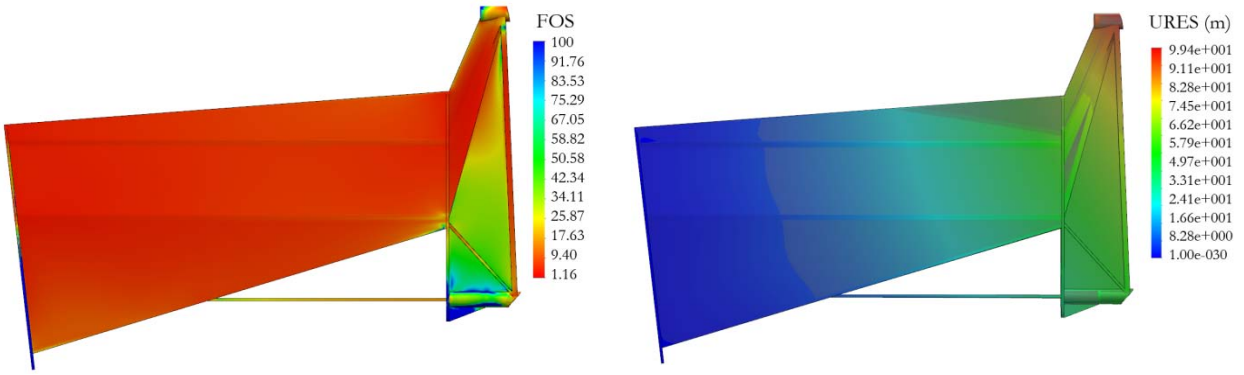

Fig. 35 FEA of aft mounted engine pylon showing contours of factor of safety (left) and maximum displacement (right)

5.8 Blade Loss Considerations

As required by FAR §25.903, the engine installation has to be done in a manner so that no flight critical items are adjacent to the plane of the propeller or high pressure turbine. This regulation recommends 5° of clearance for rotor blades and 15° for high pressure turbines. Using an analytic model for blade loss, differential equations were developed to model the motion of a blade released from the engine rotor. The analysis goal was to estimate the maximum required clearance angle to investigate the applicability of FAR §25.903 to the Albatross configuration. Using the model for drag force acting on the blades, UACC has extracted the following differential equation for the velocity of the blade,

$$m_b \dot{v} + Pv^2 = 0 \tag{2}$$

where $P = 0.5 C_{d_{blade}} A \rho$, which has solution $v = \left(\frac{1}{v_0} + \frac{Pt}{m_b} \right)^{-1}$. (3)

Solving for blade motion in two dimensions yields the following equation that models the impingement angle behind the plane of rotation of the rotor,

* As is the case that aft-mounted engines are loaded in bending and over-the-wing mounted engines are in compression.

$$\Omega = arctan\left(\frac{m_b}{P_2 D_p} ln\left(\frac{P_2 v_{0,plane}}{P_1 v_{0,prop}}\left(e^{\frac{P_1 D_p}{m_b}} - 1\right) + 1\right) - \frac{m_b v_{0,plane}}{P_1 D_p v_{0,plane}}\left(e^{\frac{P_1 D_p}{m_b}} - 1\right)\right). \quad (4)$$

Inserting relevant values for takeoff, this model indicates that the maximum clearance angle necessary is slightly greater than 1° aft of the plane of blade rotation. Figure 36 presents the impingement angle as a function of average drag coefficients acting on the propeller both in radial and transverse directions for takeoff conditions, as well as a CAD representation of the blade impingement arcs.

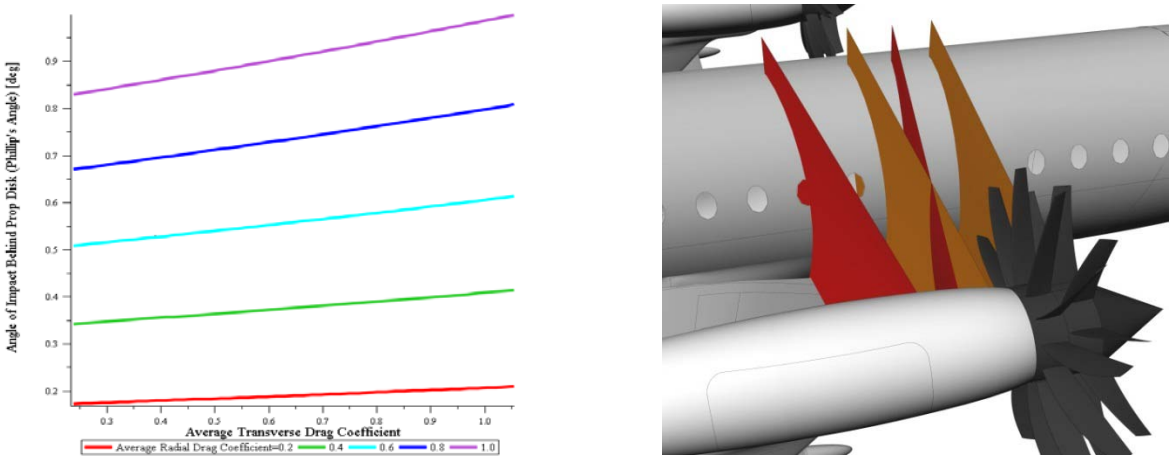

Fig. 36 Impingement angle as a function of radial and transverse drag coefficients, for takeoff conditions(left) CAD illustration of blade impingement angles(right)

This analysis assumes that it is extremely unrealistic that the blade can change its orientation enough to acquire an average radial drag coefficient greater than 0.3 during the fraction of a second it has to make it to the fuselage. This assumption was verified by performing a high speed transient CFD on the blade geometry to investigate the bounds of aerodynamic coefficients (namely C_L and C_D) for the blade. A similar analysis to the takeoff scenario was performed after inserting appropriate values for cruise conditions. The maximum realistic impingement angle was found to be approximately 4.5° aft of the plane of rotation of the blades. Figure 37 presents the impingement angle as a function of average drag

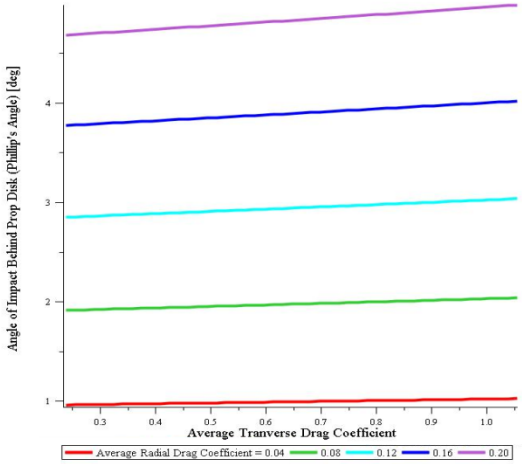

Fig. 37 Impingement angle as a function of radial and transverse drag coefficients, at cruise conditions

coefficients acting on the propeller both in radial and transverse directions for cruise conditions. Additionally, the analysis shows that there are no likely conditions under which the blade would impact forward of the plane of rotation, which was considered in the design of the wingtips of the planform of the wing.

5.9 Shock-Inlet Interferences

Considering the proximity of the engine installation to the upper surface of the wing, it is necessary to insure that there is no significant aerodynamic interference between the wing upper surface normal shocks and the internal flow of the engine inlets. Bearing in mind the sensitivity of the efficiency of low pressure compressors[47] to the uniformity of the incoming flow, significant effort was spent to determine an optimal location above the wing for the installation of the engine to minimize such aerodynamic interference. Given that similar aerodynamic interferences were investigated thoroughly as a part of the configuration design of the HondaJet[48], it was decided that similar investigations made lead to minimization of the intensity of the shock created adjacent to the wing and pylon surfaces. The results in the literature showed an increase in M_{DD}[48] and a decrease in the trim drag of the aircraft. The reduction in trim drag is caused by the local reduced downwash on the horizontal tail. According to literature, the over-the-wing method of engine installation is not only feasible, but also can be advantageous over the usual engine installation methods[49]. Detailed 3-dimensional CFD analyses were performed to verify the shock geometry and its lack of interference with the inlet, the result of which can be seen in Figs. 38 and 39.

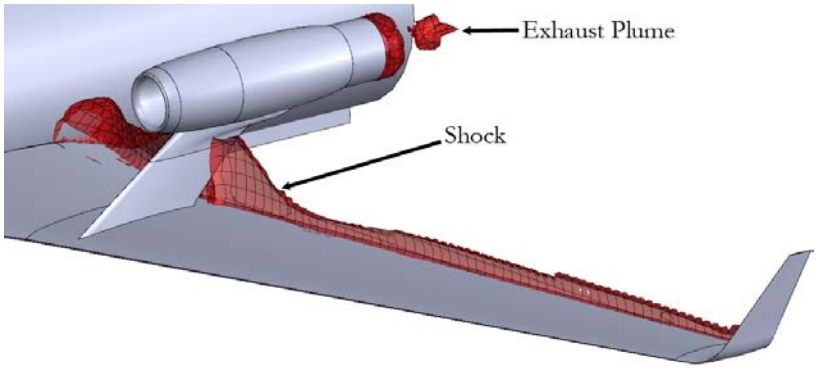

Fig. 38 Shock geometry on the proximity of the nacelle. It can be seen that the shock does not intersect the inflow path of the engine inlet.

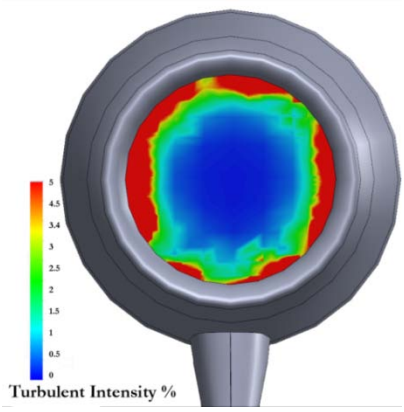

Fig. 39 Turbulent intensity on engine compressor face

5.10 Shock-Rotor Interferences

As was determined in Section 5.6, almost 98% of the engine's thrust is produced by the rotor. Given this large contribution to the performance of the entire engine, it is critical to ensure that the normal shock oscillations are fairly isolated from the rotor and have minimal influence on flow distortion levels as defined by *Seddon* and *Goldsmith*[47]. Due to the complex geometry of this problem, the only feasible approach to verify the quality of the flow approaching the fan was to perform a high-accuracy transient CFD analysis of the wing-pylon-engine assembly. The analysis was performed at cruise conditions of Mach 0.8 and an altitude of 37,000', and mesh refinement was performed near the model surfaces to capture unsteady variations in the boundary layer development of the wing, pylon, and nacelle. Results have verified that the flow approaching the fan maintains a reasonable level of distortion coefficient and has minimal swirling characteristics. In addition, the length of the nacelle is shown to assist in reducing the swirl levels induced as a result of the general spanwise outwash of the wing. Figures 40 &41 present a summary of the results of this flow simulation.

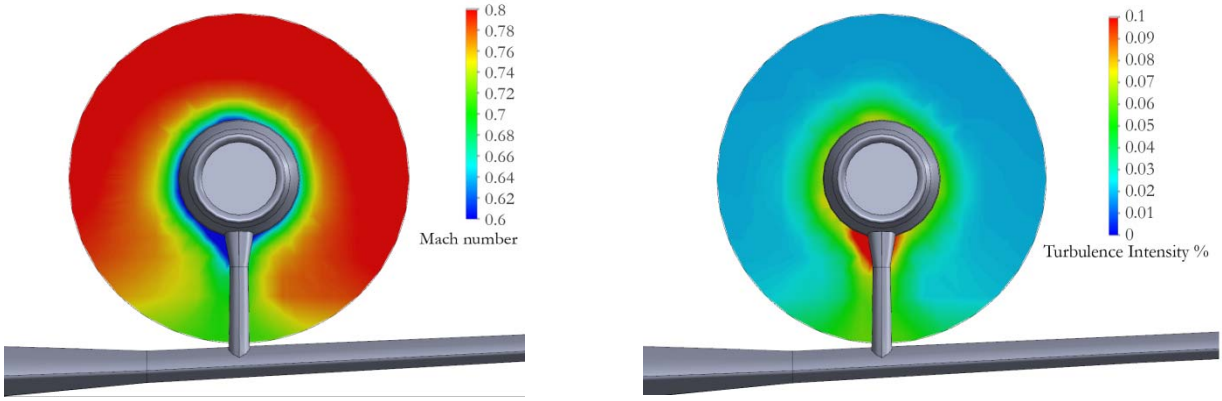

Fig. 40 Mach (left) and Turbulent Intensity (right)

Transient CFD analyses are performed using COSMO Flowworks at 35,000' and Mach 0.8. K-epsilon model is used to model turbulence. From the turbulent intensity contour (upper right), it is observed that the majority of rotor tip segments are exposed to time-averaged turbulence levels below 0.1%. Pylon and nacelle's boundary layer increases the turbulence level in the center of the rotor disk slightly.

The streamlines presented in Fig. 41 indicate that the direction of the flow near the center of the rotor disk is not significantly affected by the presence of the nacelle. Additionally, no swirl is observed.

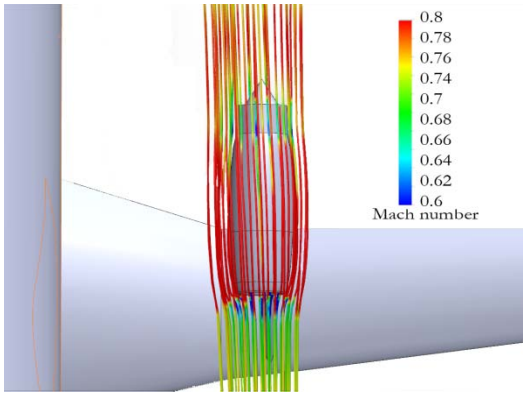

Fig. 41 Airflow streamlines representing local Mach number

5.11 Emissions

In the design of Albatross, emissions were particularly important to consider, given the possible introduction of carbon taxation in the near future. It has been suggested that such taxation would be implemented as a part of the tax imposed on the sale of aviation fuel, increasing the cost of fuel for operators of high-emission aircraft. The future market will thus be financially motivated to procure lower emission aircraft.

UACC has addressed the market demands concerning low emission aircraft by using more advanced propulsion technology, flight path optimization, alternative fuels, and general fuel burn enhancements. The modern propulsion concept of open fan engines was selected due to its significant potential to reduce TSFC, thus reducing the fuel burn and general emission levels of the aircraft. Engine design parameter optimization (see Sec. 5.5) was also performed in order to minimize the cumulative effect of NOx emissions and fuel burn of the aircraft on the environmental footprint of Albatross. The NOx intensity factor was chosen as a measure of merit for the production of NOx emissions, as defined by the Committee of Aeronautical Technologies,[50] and is presented in Equation 5,

$$S_{NO_x} = \left(\frac{P_3}{2965kPa}\right)^{0.4} e^{\left(\frac{T_3 - 826K}{194K} + \frac{6.29 - 100\,war}{53.2}\right)} \quad . \tag{5}$$

An analysis was performed using GasTurb to evaluate the NOx severity factor over the flight envelope of the engine of the aircraft, the result of which is shown in Fig. 42.

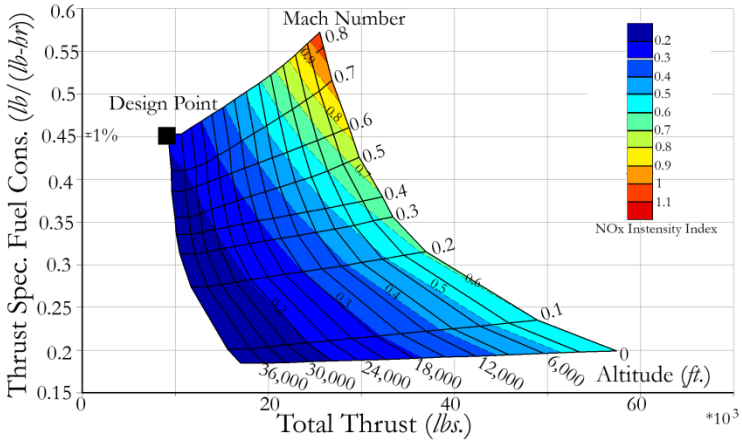

Fig. 42 NOx intensity contours plotted over engine performance map

From this analysis, it was determined that 5.75 grams of NOx is generated per every kilogram of fuel burned at 39,000' altitude. Emphasis was placed on optimizing the flight path of the aircraft[51] in order to reduce the fuel burn and corresponding emission levels by accurately determining the optimum cruise Mach number and altitude (within the range specified by the RFP). Utilizing modern structure and NLF technology contributed to reductions in weight and an increase in the L/D of Albatross, consequently providing a significant reduction in the fuel burn and emissions of the aircraft.

5.12 Maintenance

In the design of the novel engine integration used for Albatross, issues regarding maintenance and accessibility of the engine were addressed. Due to the height of the installation of the engine, special equipment will be required to remove the engine from the airframe during overhaul operations. However, the engine is not installed much higher than a conventional aft-mounted turbo fan engine and, therefore, does not present significant disadvantages to such a configuration. The weight of open fan engines increases the difficulty of engine removal. To enhance the accessibility to the installed engine, it is suggested that additional hatches to engines and accessories be provided. Figures 43 and 44 show accessibility through service hatches as well as the general method to detach the engine core from the pylon.

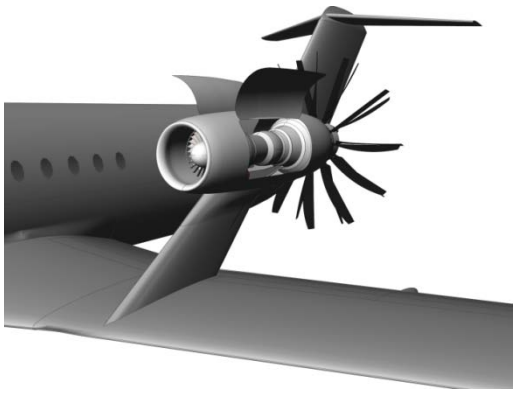

Fig. 43 The engine core accessibility

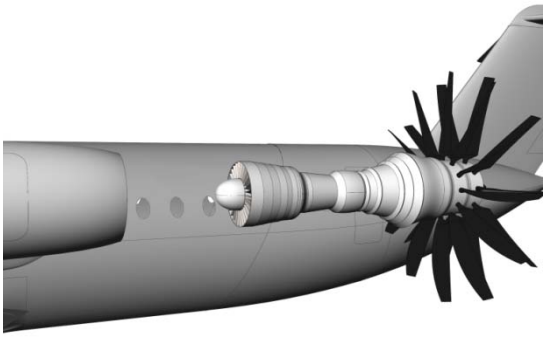

Fig. 44 Engine core detachment

6. Systems Integration

6.1 Electrical Distribution System

Commercial aircraft are gradually replacing hydraulic and pneumatic subsystems with lighter, cleaner, and more efficient electrical architecture*,[52]. The Albatross is engineered to take advantage of this potential for simpler, safer, and more fuel efficient, electrically dominant aircraft subsystems. Six starters/generators (two per engine and two on the APU) provide an estimated 740 kW to the subsystems of Albatross, based on the power consumption trends of commercial aircraft over the last two decades[53]. Each starter/generator provides a three-phase, variable frequency 230 V_{AC} to the aft electrical/electronics (E/E) bay, where 230 V_{AC}, 115 V_{AC}, and 28 V_{DC} loads are controlled by computer managed Remote Power Distribution Units (RPMUs). An additional ± 270 V_{DC} is used within the liquid cooled electrical distribution power cabinets located in the forward and aft E/E bays[54]. The larger and innovative 230 V_{AC} and ± 270 V_{DC} satisfy the needs of the higher power consumption systems, such as the electrical environmental control and pressurization system. The smaller 115 V_{AC} and 28 V_{DC} are required for traditional electrical subsystems, such as lighting and galley operations. Figure 45 demonstrates the basic power distribution hierarchy used by Albatross. More detail regarding the electrical distribution system can be found in the accompanying large scale drawing SY – 3.0.

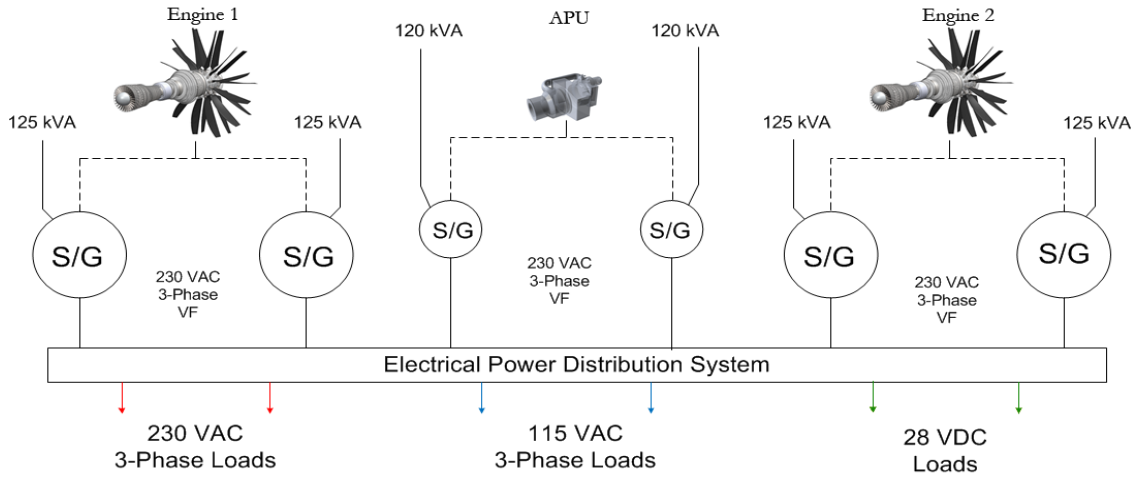

Fig. 45 Electrical power generation architecture. S/G denotes starter/generator units installed on the engines and APU. V/F denotes variable frequency.

* The Albatross generates 250 kW per channel via its starters/generators. Comparatively, the Boeing 747-400 produces 120 kW and the Boeing 787 produces 500 kW per channel. The Boeing 787 is unique in that it is the first jetliner to incorporate a bleedless architecture and thus requires large amounts of electrical power. Similarly, the Albatross' electrical systems that replace its hydraulic and pneumatic functions require greater amounts of electrical power compared against other aircraft in its class.

6.2 Electrical Pressurization and Environmental Control System

UACC has fashioned Albatross' electrical pressurization and environmental control system (ECS) after the Boeing 787 bleedless architecture. Considering that Albatross contains half the payload of the Boeing 787, UACC projects that the ECS and pressurization systems will require 250 *kW* of electrical power, as compared to the 500 *kW* for the Boeing 787[55]. The all electric environmental control system integrated into Albatross takes advantage of greater fuel efficiency by nearly eliminating bleed air and thus reducing the weight associated with traditional bleed air architecture. Ram-air inlets and variable speed, electrically driven compressors allow Albatross to expend only as much energy as required to pressurize and ventilate the cabin[56]. In a bleedless architecture[57], energy is not leached from the engine's thrust, improving the TSFC of the engine, whereas traditional bleed architecture would have adverse impacts on engine performance. Once compressed, the hot air from the electrical compressors mixes with the cool air in the mixing chamber before being distributed throughout the aircraft, as seen in Fig 46. The avionics equipment utilizes the aircraft's cool skin surface temperature and the flight deck's conditioned, uncirculated air to dissipate excess heat. Conditioned air is mixed with filtered, recirculated cabin air after passing through the dual environmental control system packs. Air that is circulated to the cabin returns to the mixing chamber via the forward cargo bay. More detail regarding the electric air conditioning system can be found in the accompanying large scale drawing SY – 2.0.

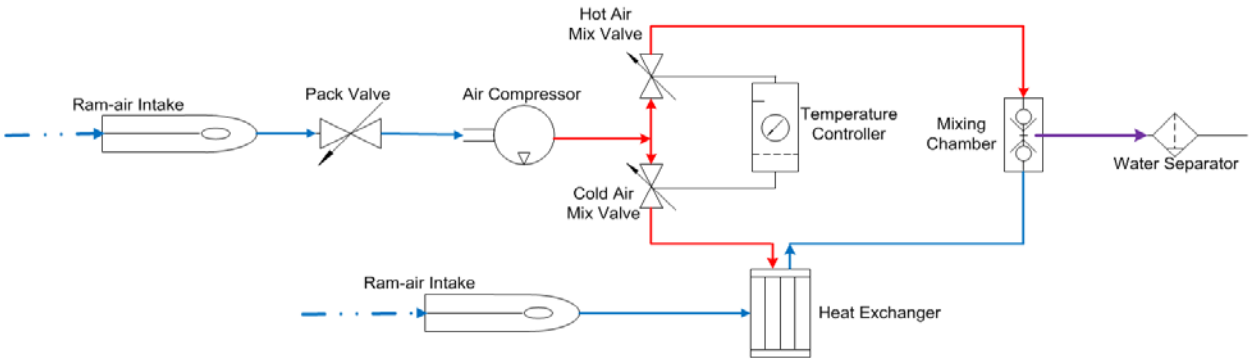

Fig. 46 Air conditioning pack flow diagram. Notice that the recirculation/filtration system is not shown here to be concise.

6.3 Electrical Flight Controls System

The Albatross employs a historically novel flight control system that replaces traditional hydraulic systems with electro-mechanical actuators. The placement of the actuators on the wing surfaces is shown in Fig. 47. The unique fly-by-wire and power-by-wire systems are operated in conjunction with three Primary Flight Control Computers (PFCC) and two airplane information management computers. The "pipelines" through which the system communicates are composed of a triple redundant, high bandwidth fiber optic network. Pilot inputs are converted into primary and secondary control surface movements through the PFCCs. Once the input is calculated by the PFCCs, commands are sent to the Actuator Control Electrics units (ACE). The ACE units control the movement of the actuators in the spoilers, flaperons, tailplane horizontal stabilizer, elevators, and rudder. The ACE units also receive feedback information on the actuator positions, which is sent back to the PFCCs for further processing. In landing and takeoff conditions, the flap positions are controlled by redundant Flap Electronics Units, which communicate with three Autopilot & Flight Director Computers, while the flaperons are controlled directly by the ACEs and PFCCs. The flight control system loop is completed when the pilots receive tactile feedback via "feel" actuators located in the flight deck. A major advantage of this all-electromechanical system is that it reduces weight by replacing traditional hydraulic systems[58]. Additionally, maintenance is simplified because individual actuators can be replaced without draining hydraulic fluid, which increases the aircraft's utilization time[59]. More detail regarding the electrical flight controls can be found in the accompanying large scale drawing SY – 4.0.

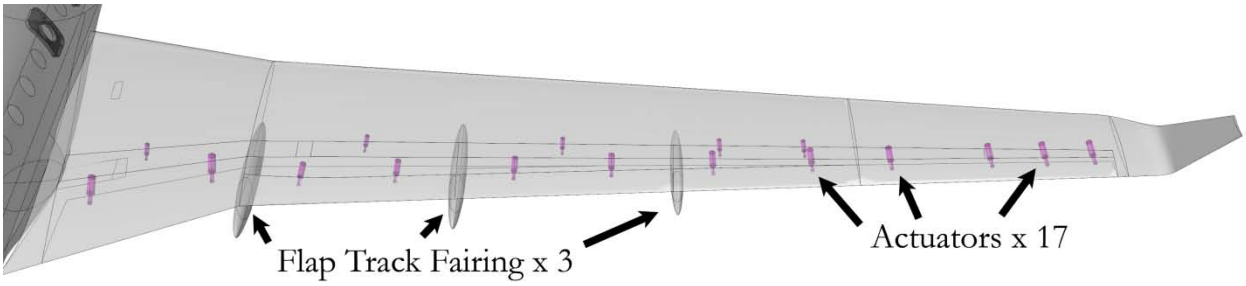

Fig. 47 Location of control surface actuators and flap track fairings

6.4 Landing Gear/Tire Spray

The nose landing gear is of the self-contained hydraulic shock absorber type and is equipped with a steer-by-wire system that is actuated electrically by a link to cockpit controls. It is retracted forward by a drag-brace-member that is electrically actuated. Nose landing gear doors are mechanically linked to the system to allow deployment. The large portion of the nose landing gear bay is sealed by the landing gear doors to reduce the airframe noise and drag of the aircraft and is only opened during the retraction/deployment process. Figure 48 presents the nose landing gear integration. The main landing gear is attached to the wing via a gear beam and a trunion. The main landing gear bay has outboard and inboard doors, the latter of which is closed except during the retraction/deployment process to reduce airframe noise and drag. The doors are operated by electric motors and the retraction/deployment mechanism is done through a side brace electric actuator. Main shock absorption is done using a self-contained hydraulic oleo. Figure 49 presents the main landing gear. Both the main and nose landing gears can be mechanically unlocked; therefore, allowing them to fall onto their own weight and achieve down lock as a result of kinematic air pressure acting on their surfaces. Using the method presented by ESDU Data Item 83042[60], the maximum depth of contaminates on the surface of the runway, at which the takeoff of the aircraft will be impacted by the impinging tire spray released from the nose landing gear, was determined to be 3/8", corresponding to a side spray elevation angle and a plan view angle of 14º each.

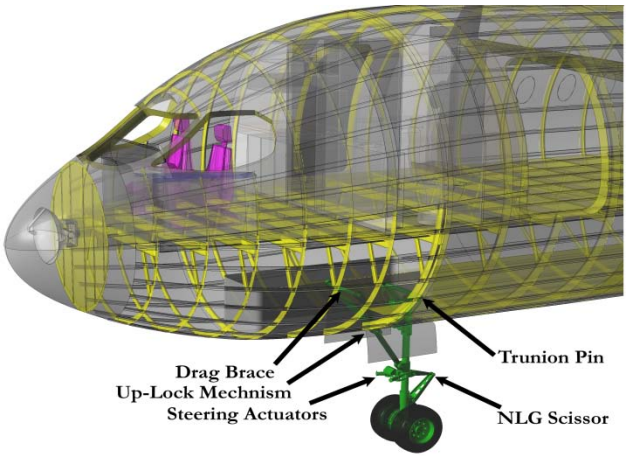

Fig. 48 Nose landing gear

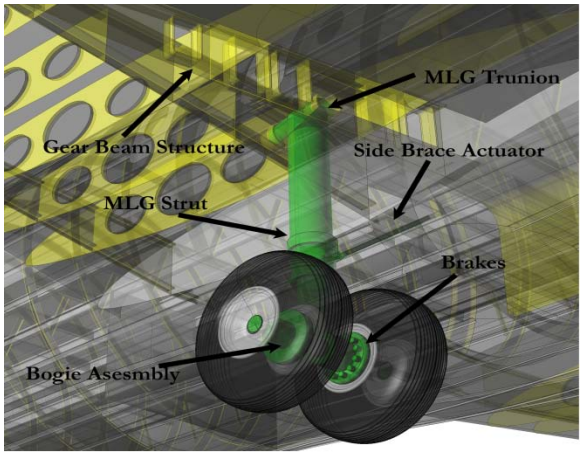

Fig. 49 Main landing gear

Tire spray analysis was performed in order to determine the compatibility of the engine installation configuration with a spray pattern that could potentially damage the engine core or fan blades if it contains mud or ice. Notice that the critical design case will not be the occasional exposure to this material, rather a continuous occurrence of foreign object debris ingestion.

Fig. 50 Tire spray analysis results

6.5 Avionics and Cockpit Integration

The main avionics and computational task are performed by two Aircraft Information Management Computers (AIMC). Communication with the Data Localizing Units (DLU) and the Remote Power Management Units (RPMU) is performed by the redundant, high speed, fiber optic information network. The DLUs gather analogue, digital, and serial data from remote avionics and aircraft systems sensors. The RPMUs control and distribute power loads from electrical cabinets located in the forebody and mid fuselage sections based on information received from remote hardware. That information is processed by the AIMCs and fed into the cockpit instrument panel. The location of the E/E bays is shown in Fig. 51. There are five 15" diagonal main display units in addition to two Multi-Function Interactive Display Units (MIDUs). Both the pilot and first officer have individual Head Up Displays (HUD) with their own control units located in the mid console beneath the landing gear lever. Information displayed on the HUDs and five main displays can be customized according to the pilot and first officer's preferences. More detail regarding the instrumentation of the cockpit can be found in the accompanying large scale drawing SY – 7.0.

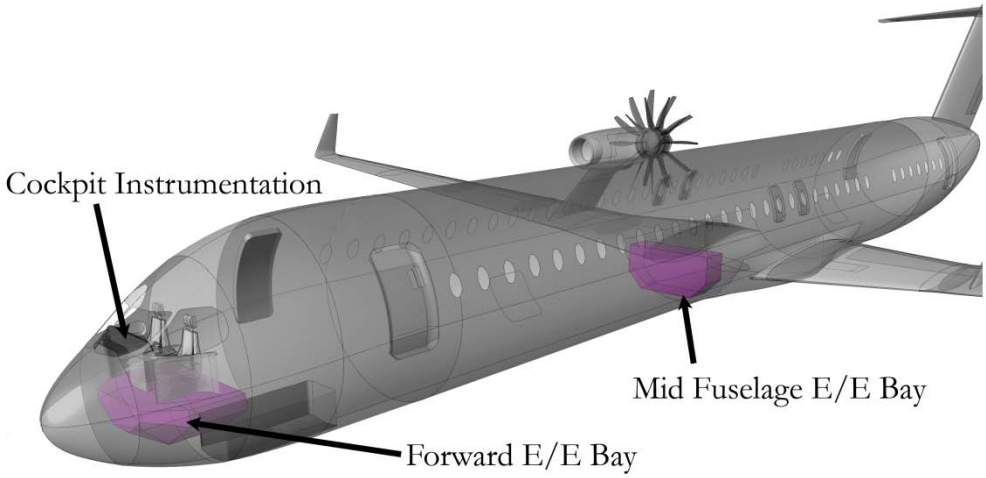

Fig. 51 Location of E/E bays along with Cockpit Instrumentation

6.6 Fuel System

The Albatross' fuel system is comprised of three main fuel tanks, each supplying the engines with two fuel pumps, located in the wings and lower center fuselage. In the event of any one or two fuel tank failures, the aircraft can maintain operation through a single fuel supply pump. Once at cruise altitude, engines are suction-fed and fuel pumps can be turned off, reducing energy requirements during flight. Albatross is also equipped with a fuel jettison system that can quickly dump fuel through valves located in the outboard wings in the event of a need for a rapid emergency landing, therefore reducing the landing weight of the aircraft so that landing gear structure remains intact.

6.7 Inert Gas Generation System

Safe oxygen levels in the fuel tanks have been more rigorously enforced in the 21th century since the 1996 Trans World Airlines Flight 800*. Oxygen in the fuel tanks is a potential explosive hazard that becomes more and more dangerous as the empty space in the fuel tanks increases. Considering this safety hazard, the fuel vapor-laden volume within the wing and center tanks (also known as ullage) is replaced by a 95% nitrogen rich gas until the oxygen levels are between 9% - 12%†. The Albatross' inert gas generation system collects air from the plane's underbelly space via pumps. The air is then compressed using an electric motor and the Air Separation Module (ASM) membrane separates the oxygen from the rest of the gas. The now nitrogen rich gas is pumped into the fuel tanks to reduce the oxygen content of the respective ullages to 12% levels. Figure 52 presents the inert gas generation system.

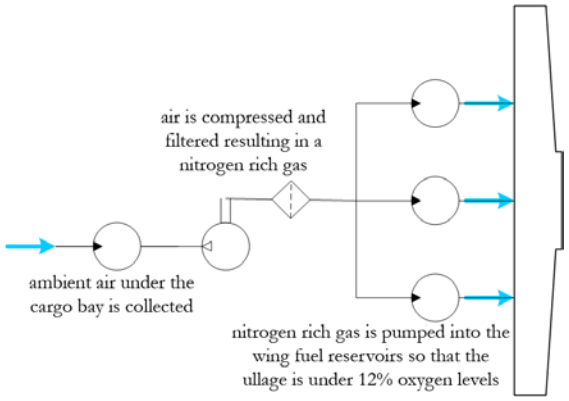

Fig. 52 The architecture of the inert gas generation system providing a nitrogen-rich gas mixture to wing fuel tanks

* TWA Flight 800 in 1996 was an airplane disaster off the coast of Long Island. It is speculated that unsafe oxygen levels in the fuel tanks led to a catastrophic explosion.

† For reference, combustion is not considered possible below 9% oxygen levels. The standard for commercial aviation fuel safety is 12%, at which the chances for combustion are significantly reduced. Atmospheric air has an oxygen level of 21%.

6.8 Auxiliary Power Unit Integration

To provide the power needs of the aircraft on the runway, as well as to supply the aircraft's power grid at the instances of significant power use, an auxiliary power unit (APU) was integrated into the tailcone. This system was equipped with two 120 *kW* alternating current, three phase, variable frequency generators producing the electric power needed by the grid. The APU fuel flow is provided from the central wing tank through a dedicated pump/valve system. Given the proximity of the location of the installation of the APU to the empennage of the aircraft, and in compliance with FAR §25.903, the vertical tail was equipped with a three spar structure to ensure the redundancy in case of a blade loss occurring at the APU. The APU's exhaust is directed to a muffler via high temperature resistant ducting, and after suppression it is disposed of at the apsis of the tailcone contributing towards reducing the intensity of the fuselage wake. Figure 53 presents the location of the installation of the APU and the recommended zones by FAR §25.903 for clearance maintained from the critical structure of the vertical tail.

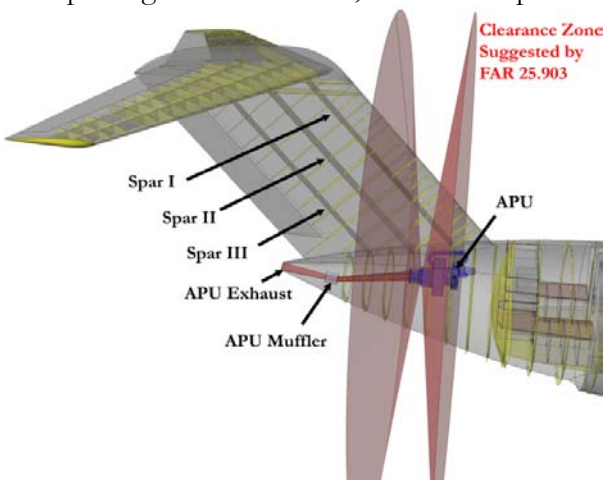

Fig. 53 APU installation showing the FAR §25.903 clearance zone for turbine equipment. In the event of turbine blade loss, there are at least two spars to keep the empennage intact.

6.9 Lightning Protection

Since Albatross uses composite structures which are non-conductive material, there exists a need to implement a mesh of highly conductive material to conduct electricity near the surfaces of the aircraft in the event of a lightning strike. Due to machine-aided process used in manufacturing Albatross, such conducted mesh can be laid during the process of manufacturing of the composite outer skins. If such a system is not implemented, local accumulation of charge on the non-conductive fuselage during a lightning strike will cause significant structural damage to the aircraft, as a result of the melting of structural elements located near the location of lightning impingement.

6.10 Water & Waste Management

The waste and water system distributes, stores, and disposes of potable and black water between the galleys, lavatories, storage tanks, and service ports. The potable water is pressurized by an electric pump and distributed to the galleys and lavatories from a 200 L storage tank located behind the aft cargo compartment. Due to the possibility of the operation of the aircraft in the areas in which the potable water contains bacterial and mineral contamination, Albatross was designed with a water filtration system. Water running through the potable water lines is filtered continuously by a dedicated water pump and filtration unit and is returned to the potable water tank. Used potable water or wastewater from the galley and lavatory sinks is disposed overboard via pressurized anti-icing ports. A vacuum generator forces the black water from the lavatory toilets into a 170 L waste tank also behind the aft cargo compartment. Black water is properly disposed of once the Albatross has landed.

The architecture of the water and waste system consists of pipes, valves, ports, tanks, and low power hardware. Traditional 115 V_{AC} and 28 V_{DC} powers the electrical components of the water and waste system including sensors, heaters, valves, vacuum generators, controllers, and compressors. The Albatross' unique all-electric architecture avoids unnecessary weight penalties and power losses by replacing the bleed air with electrical pumps. The new system is simpler, easier to maintain, and more fuel efficient without stealing thrust from the engine to pressurize the water. Figure 54 presents the inboard profile of the aircraft showing only the water and waste systems connecting the galleys and lavatories to their respective storage tanks.

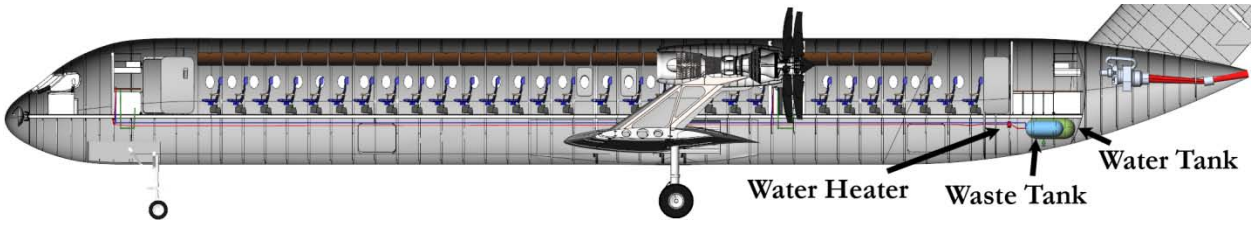

Fig. 54 Inboard profile of Albatross featuring water and waste systems along with piping.

6.11 De-Icing and Anti-Icing System

Ice detectors work in conjunction with the de-icing and anti-icing subsystems at the engine inlets and leading edges of the wings, empennage, nosecone, and cockpit windshields. Electro-thermal heating blankets are secured within the interior of the leading edge of the wings and tail, and are used for both icing prevention and removal. The move from bleed air architecture to an electrical icing subsystem is highly advantageous for its previously mentioned savings in weight, complexity, upkeep, and fuel efficiency, as well as improvements in drag and noise from the removal of the exhaust ports. UACC predicts that the electrical icing subsystem will require a relative 50 kW based on the power needs of the Boeing 787[61]. Additionally, the engine internal de-icing makes use of the engine's own bleed air from a fan casing valve. The use of the engine bleed air for its own icing protection is the most effective method at the present time and will probably not be changed in the near future because it does not have the weight penalties of most other pneumatic architecture.

6.12 Cargo Handling

The cargo in Albatross is carried in both containerized and bulk cargo form. Cargo is stored in Albatross on the lower deck in three main compartments. The front cargo compartment can house 867.3 ft^3., equivalent to 12 LD-W unit load devices (ULDs). The aft cargo department can house 542.1 ft^3. of containerized cargo, equivalent to 5 LD-W ULDs, as well as 181.6 ft^3. of bulk cargo aft of the cargo door. Both cargo doors are of the 48" x 35" type, allowing rapid loading of containerized or bulk cargo into the aircraft, reducing the turn-around time for the carrier. The cargo floor is equipped with uni-directional rollers and ball rollers in front of the cargo loading doors. 5" lifting power rollers in front of the cargo doors provide both lateral and longitudinal movements for the containerized cargo being loaded. The cargo handling system is controlled by control panels installed near each cargo door.

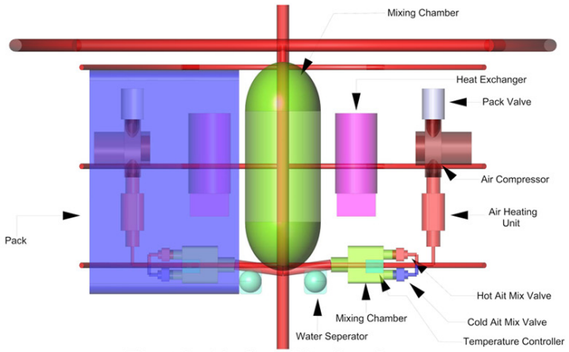

Electric Air Conditioning System

Systems Integration Drawing. A view of the cockpit instrumentations is also presented (right).

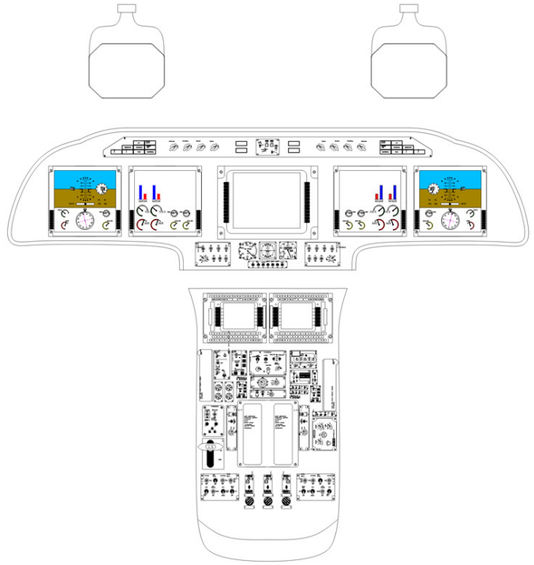

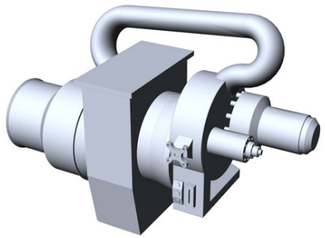

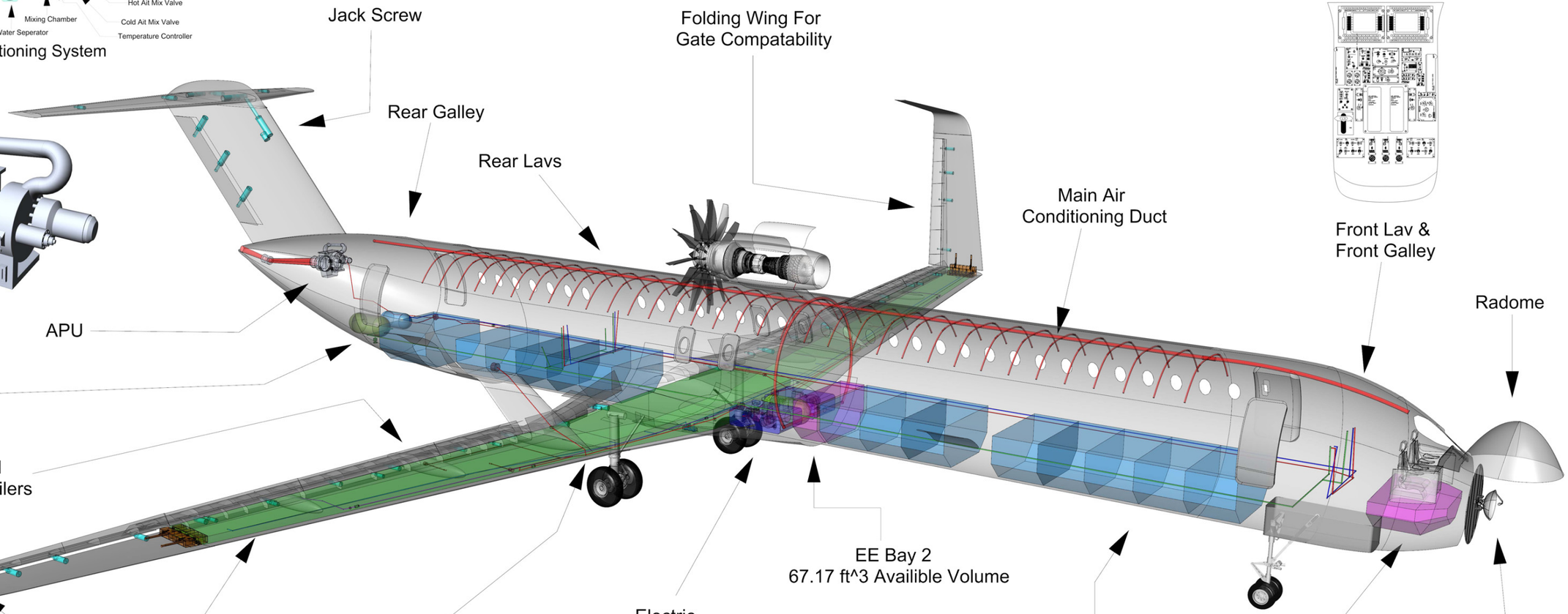

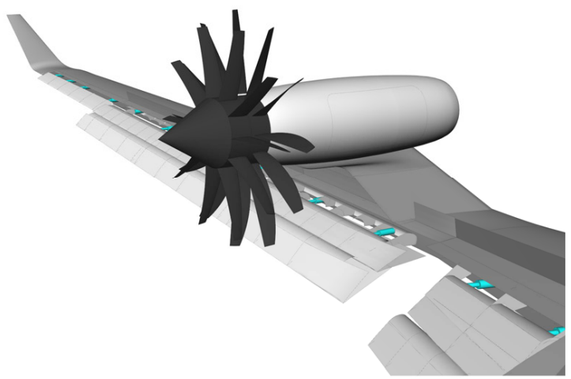
Deployed
Flaps & Spoilers

7. Weight Justification & Analysis

7.1 Folding Mechanism Weight Increment

As requested by the RFP, in order to maintain compatibility with worldwide conventional airport infrastructure, Albatross was equipped with a folding wing mechanism, as shown in Fig. 57. The outboard 19.5' of the wing can be folded on the tarmac to reduce the overall span of the wing to 118', making it possible for Albatross to dock in present-day style terminals designed for mid-haul commercial jetliners, such as the Boeing 737 and Airbus A320, with no need for further modification of existing infrastructure. This was accomplished through a multi-lug folding mechanism, separating the outboard wingbox from the inboard wingbox and secured on the surfaces of the front and rear spars of the wingboxes, as well as the upper and lower skin panels. The folding is operated using electro-motors equipped with a worm-geared mechanism and it folds between the direction of the dihedral of the wing and the direction perpendicular to the ground. The folding mechanism is secured before taxi and takeoff by electrically operated latch pins that are inserted into the connector plate installed on both sides of the folding mechanism. Figure 55 shows the operation of the folding mechanism and Fig. 56 presents a close-up view of the locking mechanism. The weight increase associated with the folding mechanism of the wing was estimated using data obtained from the folding wing version of the Boeing 777 prototype. The weight increase figures were normalized to the Boeing 777's empty weight and applied to the weight estimations of Albatross, resulting in an 800 *lbs.*[62] weight increase in the wing structure.

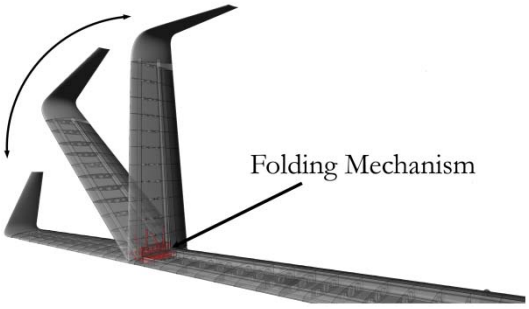

Fig. 55 The operation of the folding mechanism

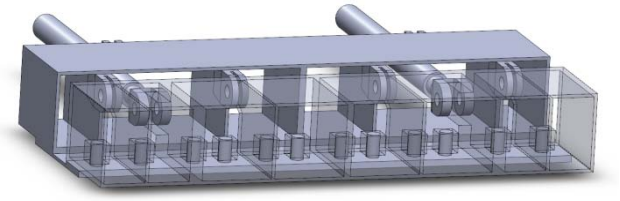

Fig. 56 A close-up of the folding mechanism showing the two electric actuators

7.2 Fuselage Acoustic Insulation Weight Increment

In light of data obtained from the NASA PTA project overview[63], it is expected that, due to the proximity of open rotor blades to the cabin of the aircraft, excessive interior noise levels are to be expected in the cabin. To remedy this, additional noise insulating material will be required inside the wall lining of the cabin to absorb the acoustic energy radiated from the adjacent rotor blades. The method presented by *Willby* et al.[64] was used to approximate the weight penalty from additional noise insulation in the mid fuselage section. This weight increment was added to the averaged weight figures for the fuselage structure.

7.3 Electrical System Architecture Weight Decrement

As was presented in Chapter 6 of this document, the full electric architecture of Albatross allows for significant weight reductions, as a result of simplification of the systems and elimination of heavy subsystems pertaining to hydraulic and bleed air power supplies. The Albatross' all-electric architecture saves considerable weight by eliminating the unnecessary bulk and materials associated with hydraulics and pneumatics. Multiple NASA/Lockheed case studies[65,66]analyze the potential weight, fuel burn, and cost reductions of the all-electric architecture against conventional subsystems. One case study estimated an uniterated 2,700 *lbs.* weight reduction in a plane with a operating empty weight of 238,000 *lbs*. Simpler and cleaner electromechanical subsystems cut out the unnecessary weight from the aforementioned parts. Additionally, the electrical hardware is made more efficient and simpler via the RPMUs.

A NASA/Lockheed study[67] predicted a 22% net empty weight reduction from flight controls, APU, instruments, hydraulics & pneumatics, electrical hardware, avionics, air conditioning, and anti-icing systems in a generic 150 passenger jetliner. The specified system weights were reduced or eliminated except for slight increases in the APU, electrical hardware, and avionics. These small weight increments were more than compensated from the elimination of the hydraulic & pneumatic piping and over 40% reduction in the air conditioning weight, due to the removal of a bleed air

architecture. The Albatross' weight reductions from all-electric architecture were based on the projections of relevant literature. The reductions were compared individually to the Albatross' weight iterations and computed as either a ratio or flat difference. Each change to the empty operating weight was normalized with respect to the payload of the Albatross in order to promote a more thorough and accurate projection. Figure 57 presents the weight adjustments for Albatross due to an all-electric architecture.

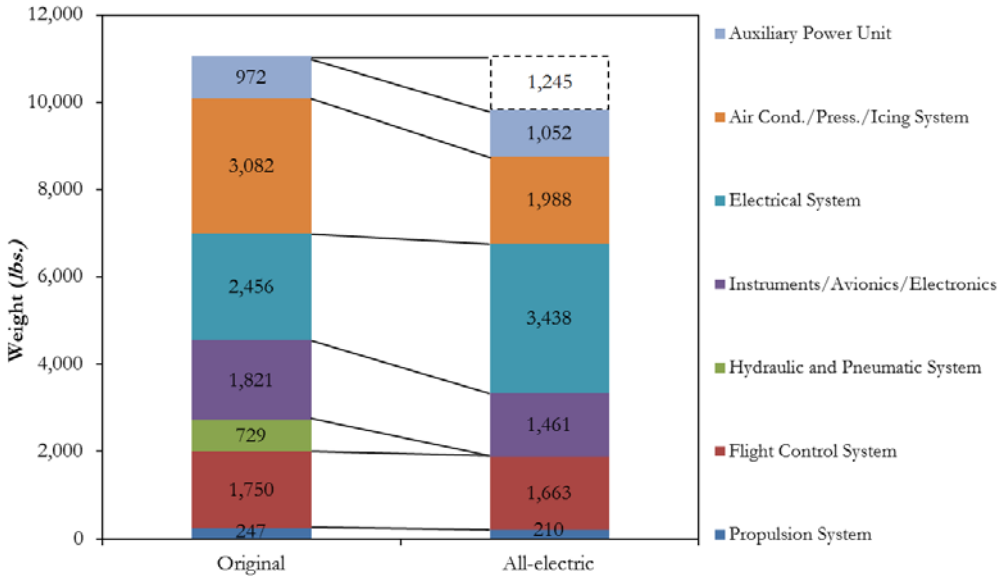

Fig. 57 Albatross' weight adjustments due to all-electric architecture. Note that net weight reduction is indicated above the right hand weight column.

7.4 Final Weight Analysis

The Albatross' weight was estimated from its mission design requirements and geometry comparable to similar aircraft. The initial estimates were averaged against the General Dynamic and *Torenbeek* methods[68], and then fed into an iterative algorithm. The impact of lightweight composites was estimated by comparing the reduced weight of Boeing 787 components against the components of similar-sized aircraft. The differences were calculated as a percent reduction shown in Table 5. The additional weight penalties due to unique aircraft components, such as the folding wingtips and open fan noise insulation, were normalized with the weight reductions that resulted from an all-electric architecture, verified by the appropriate literature, and then applied to Albatross.

Table 5. Weight Correction

Empennage	-15 %
Wing	-20 %
Fuselage	-17 %
Nacelle	-10 %
Landing Gear	-3%
Fixed Equipment	-7%

Table 6 presents the detailed empty weight estimation using General Dynamics, *Torenbeek*, and statistical methods. The corrected average values were obtained by averaging the aforementioned methods and applying the weight corrections of Table 5.

Table 6 Detailed Empty Weight Estimation

Components	GD Method (*lbs.*)	Torenbeek Method (*lbs.*)	Statistical Results (*lbs.*)	Corrected Avg. Values (*lbs.*)
Wing	14,578	24,150	13,324	11,812
Folding Wing Components	-------	-------	-------	800
Horizontal Tail	1,097	1,383	1,950	1,261
Vertical Tail	1,020	1,238	1,671	1,121
Fuselage	8,609	15,292	15,511	10,960
Predicted Sidewall Penalty	-------	-------	-------	1,181
Nacelles	2,975	2,366	1,845	2,156
Nose Landing Gear	656	931	810	784
Main Landing Gear	3,664	5,199	4,520	4,396
Engines	-------	9,886	9,979	15,344
Fuel System	-------	372	376	266
Propulsion System	374	232	305	210
Flight Control System	1,949	2,557	1,508	1,663
Instruments/Avionics/Electronics	1,944	2,272	1,411	1,461
Electrical System	1,753	4,079	1,952	3,438
Air Cond./Press./Icing System	4,556	2,737	2,441	1,988
Oxygen System	269	247	173	218
Auxiliary Power Unit	-------	1,246	751	1,052
Furnishings	7,539	8,621	5,408	6,912
Cargo Handling Equipment	-------	2,391	1,442	1,820
Operational Items	-------	6,785	4091	5,165
Other Items	-------	467	282	384

Table 7 Detailed CG location and moments of inertia of Albatross

Component	Weight *(lbs.)*	X_{CG} *(ft.)*	Z_{CG} *(ft.)*	$\lvert L_{xx} \rvert$ *(lb.-ft.)*	$\lvert L_{zz} \rvert$ *(lb.-ft.)*
1-Wing	11,812	74.91	-2.51	884,837	29,648
2-Horizontal tail	1,261	136.88	21.21	172,606	26,746
3-Vertical tail	1,121	113.15	17.55	126,841	19,674
4-Fuselage	10,960	59.68	1.21	654,093	13,262
5-Nacelles	2,156	113.72	7.52	245,180	16,213
6-Nose Landing Gear	784	17.43	-4	13,665	3,136
7-Main Landing Gear	4,396	79.62	-4	350,010	17,584
8-Engine	15,344	117.62	6.86	1,804,761	105,260
9-Fuel System	266	73.63	-2.54	19,586	676
10-Propulsion System	210	117.62	6.86	24,700	1,441
11-Flight Control System	1,663	77.22	-1.25	128,417	2,079
12-Avionics, Electronics & Instrum.	1,461	9.54	-1.45	13,938	2,118
13-Electrical System	3,438	63.16	4.3	217,144	14,783
14-Air Conditioning/ Anti Icing	1,988	75.03	-1.12	149,160	2,227
15-Oxygen System	218	75.03	-1.12	16,357	244
16-Auxiliary Power Unit	1,052	124.37	4.25	130,837	4,471
17-Furnishings	6,912	70.42	1.88	486,743	12,995
18-Cargo Handling Equipment	1,820	39.67	1.21	72,199	2,202
19-Operational Items	5,165	75.19	5.74	388,356	29,647
20-Other	384	13.79	-1.51	5,295	580

The center of gravity location was estimated based on their internal configurations and respective iterations of the weight analysis. The defined locations of the empty weight components are shown in Table 7, and are also located in the updated side profile for the aircraft in Fig. 58. Tables 8 through 10 show a detailed summary of takeoff and empty weight figures, as well as moments of inertia.

Table 8 Detailed takeoff weight

W_{fix}	24,101 *lbs.*
$W_{Structure}$	34,469 *lbs.*
W_{PP}	15,821 *lbs.*
W_{PL}	36,925 *lbs.*
W_{Crew}	950 *lbs.*
M_{ff}	0.800
M_{tfo}	*0.5%*
$W_{F_{Used}}$	20,100 *lbs.*
$W_{F,\max}$	37,339 *lbs.*
W_{tfo}	746 *lbs.*
W_E	74,390 *lbs.*
W_{TO}	148,729 *lbs.*

Table 9 Empty Weight CG

X_{CG}	71.75 *ft.*
Y_{CG}	0 ft
Z_{CG}	1.66 *ft.*

Table 10 Moment of Inertia

I_{xx_B}	71,033 slug-ft^2
I_{yy_B}	2,086,613 slug-ft^2
I_{zz_B}	2,015,580 slug-ft^2
I_{xz_B}	222,095 slug-ft^2

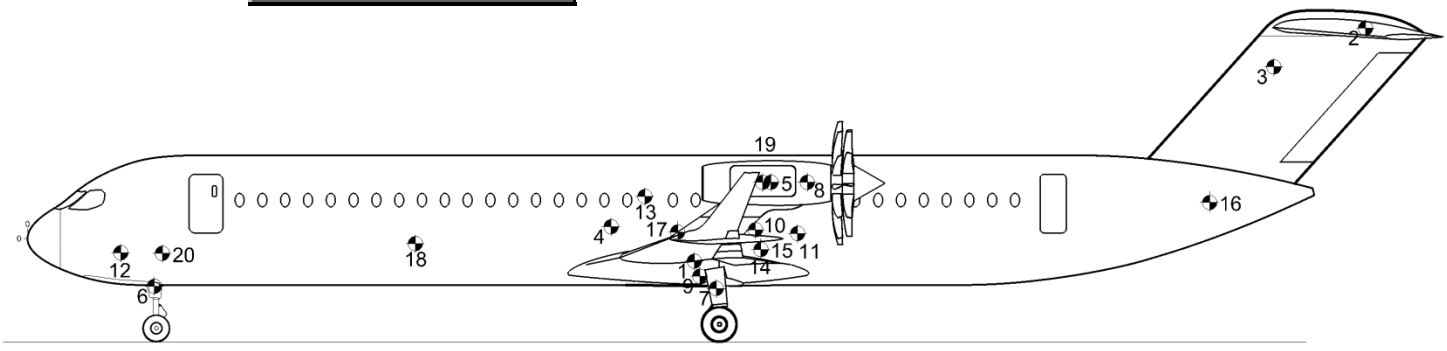

Fig. 58 The location of the main items listed in Table 7

8. Structures

8.1 Material Selection

The UACC determined that the optimum structural material for the Albatross should be composites after considering the three main factors of weight, manufacturing methods, and near-field acoustic fatigue tolerance. The weight reduction due to aggressive utilization of advanced materials will improve the general fuel economy performance by reducing the overall mass as well as the induced drag of the aircraft due to less required lift to maintain steady flight. Manufacturing methods, which will be discussed in greater detail in Section 8.6, are important when determining material selection when one considers the argument presented by *Raman Raj et al*[69] comparing the "buy-to-fly" ratio of aircraft using 65% modern aluminum alloys with highly composite-based aircraft. "Buy-to-fly" ratio is defined as the weight of the purchase material to the weight of the finished structure. It is argued that given the large quantities of wasted raw materials created in the process of manufacturing metal structures, a very high-tech composite structure can be a more cost-effective way to manufacture primary airframe structures due to the significant reduction in raw materials consumed and thus reducing the manufacturing costs. Open-fan engines present a unique element when considering material selection due to near-field acoustic fatigue tolerance, which is not present in enclosed-rotor turbofans. Given the high level of near-field acoustic disturbances associated with open-fan engines[34], acoustic fatigue of structures adjacent to the rotor-blades is critical in the design of the airframe. The ESDU Data Item 84027[70] demonstrated that aluminum laminate-based composites, such as GLARE, have the required tolerance when exposed to continuous, random acoustic loading.

Carbon-laminated composites were selected for the fuselage, wing structure and surface, and empennage due to the potential for significant reduction in structural weight, as discussed in Section 7.4. UACC considered comparatively less cost-effective carbon sandwich composites due to their high strength for the engine nacelle, winglets, and control surfaces of the aircraft because these thin

surfaces must withstand a wide range of loads while maintaining a thin profile. Titanium alloy Ti-8Al-1Mo-1V was used in the design of the pylon main structure due to its extremely high modulus of elasticity, yield strength, and heat tolerance. GLARE laminates were selected to be used on the skin of the surfaces near the engine rotor, such as the engine pylon and nacelle structures, due to their acoustic fatigue resistance characteristics. Glass fiber reinforced polymers are considered for the construction of parts that have been manufactured in a single piece and have complex geometric features and high surface curvatures, such as the radome and wing-to-fuselage fairings. The distribution of materials over the surface and substructures can be seen on the structural isometric foldout.

8.2 Load Estimation for the Wing

A maneuver envelope was constructed using guidelines provided by FAR §25.335 to determine the critical case load factors for the structural design process of Albatross. This study indicated that the airframe is to be designed for a positive pull-up load factor of 2.5 g to occur at 260 *keas* at 37,000' and a negative push-over load factor of -1 g to occur at speeds between 235 and 260 *keas*. It was determined that the maneuver speed of Albatross is 228 *keas* and the maximum safe flight speed in a 50 *ft/sec* gust is 239 *keas*. The dive speed at cruise altitude is computed to be 330 *keas*. The final V-n diagram is shown in Fig. 59.

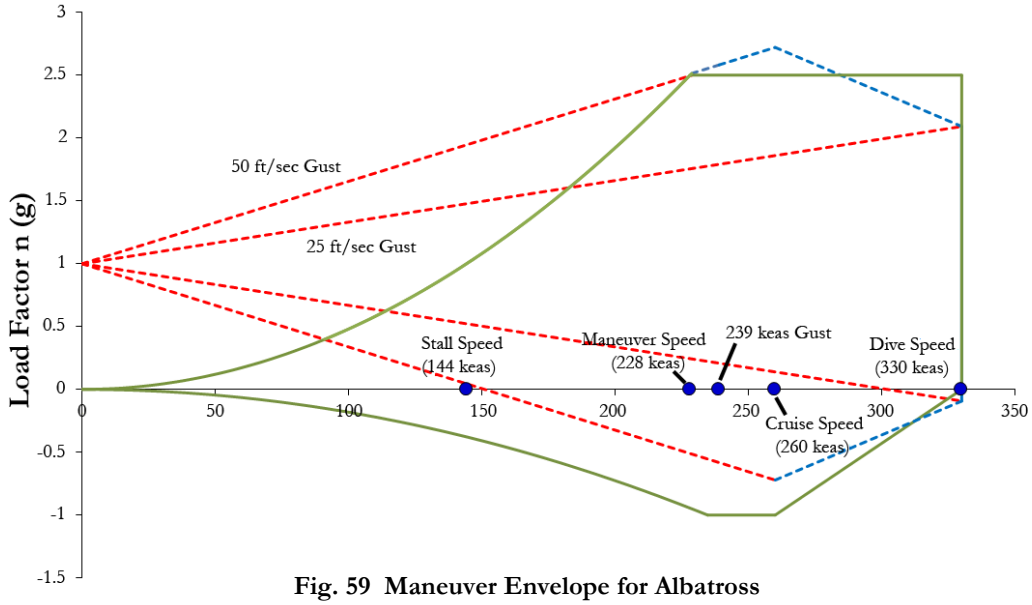

Fig. 59 Maneuver Envelope for Albatross

The shear and bending moment diagrams for wing and fuselage were computed along *Libove*'s principal axes[71] to perform structural analysis and sizing using AAA's load module, which computes the total load by taking into account aerodynamic and dynamic loads in addition to concentrated and distributed weight sources on the lifting surfaces and fuselage structures. To accomplish this analysis, the aerodynamic loads acting on the wing structure were estimated using various high order methods presented in ESDU Data Item 83040[72], the result of which is shown in terms of lift, drag, and moment diagrams in Fig. 60. The moment coefficient plotted is computed around the elastic axis of the wing considering both lift and twisting forces acting on the structure.

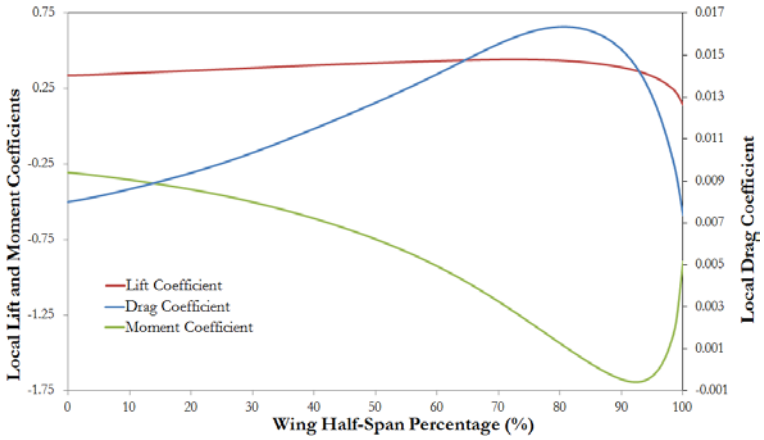

Fig. 60 Lift, drag, and moment coefficients vs. wing half span %

The loads acting on the wing structure were calculated by considering both the derived distribution of lift and drag forces as well as the torsional moment acting on the wing structure. The total acting forces and moments on the wing were computed by summing the aforementioned aerodynamic forces with the concentrated weight of the engines, wing structure, and the distributed fuel weight,. These values were multiplied by a load factor of 2.75 to comply with the critical loading cases predicted by FAR §25.335. Figure 61 presents the final results of the critical wing load case for which the wing structure was designed.

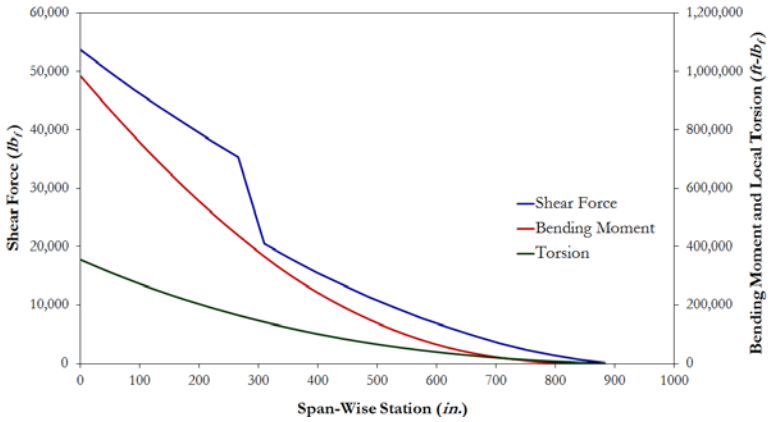

Fig. 61 Wing Loading

8.3 Wing Structure & Flutter

The wing structure of Albatross presents a number of unique features that require novel design solutions. First, Albatross is designed to take advantage of maximum NLF on the surface of the wing to reduce airframe drag. However, slightly misaligned edges can trip the boundary layer causing unfavorable drag-inducing turbulent flow on the surface of the wing. Therefore, the wing skin structure consists of two single-piece skin panels on the upper and lower surfaces to minimize the potential of misaligned skin panel edges, which is more likely to occur with multiple skin panels per surface. Second, the large wingspan of the wing planform can render the Albatross incapable of using much of contemporary airport infrastructure, thus UACC has integrated a wing-folding mechanism to allow the aircraft to dock with gates currently capable of handling Boeing 737 and Airbus A320 aircraft. Lastly, wing flutter was addressed in the design of the high AR wing planform by increasing the number of stiffener elements under the wing skin panels.

Albatross is not affected by the limitations of the manufacturing methods of an aluminum airframe, which restricts the size of the panels to the overall dimensions of the raw material and the tooling machinery. Utilization of composite materials and modern manufacturing technology allows Albatross' wing skin panels to be laid up in two continuous pieces, therefore minimizing the potential for misalignment and the resultant turbulent flow experienced on the surface of the wing. Although this manufacturing strategy increases the size of the tooling and autoclaves needed to cure the composites after manufacturing, it improves the potential for maintaining laminar flow on the wing.

The wing super-structure consists of two primary spars, located at 15% and 65% of the chord length, and a series of composite ribs that are spaced on average 26" apart. The upper and lower wing skin panels are attached to the wing super-structure via reinforced brackets located on skin panel stiffeners that are connected to the wing ribs. The landing gear is installed on a dedicated gear beam, which is connected to the rear spar of the wing as well as a structural hardpoint on the

fuselage. The trailing edge fowler flaps are an independent structure that is installed on the rear spar and landing gear beam. The surfaces of the trailing edge high-lift devices are constructed of machined composite sandwich panels, which results in a high-strength, low-weight structure. Figure 62 presents a detailed breakdown of the Albatross' wing structure.

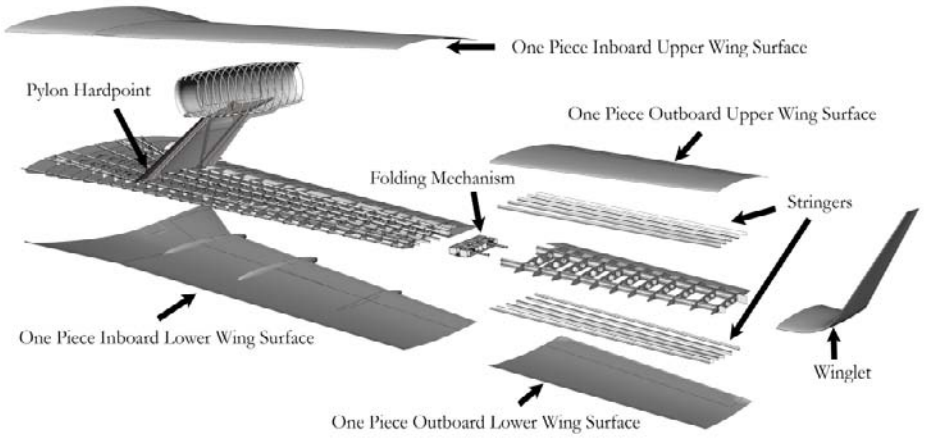

Fig. 62 Wing structure breakdown

Load analysis presented in Section 8.2 was used to perform an estimation of the wing skin thickness and overall area of wing spars. The super-structure was precisely defined by using AAA's software structure module to calculate the total skin cross-section area as well as shear web cross-section area of the at 21 distinct stations along the span of the wing. Figure 63 presents the result of this analysis, which was used to define a detailed parametric CAD model of the wing structure.

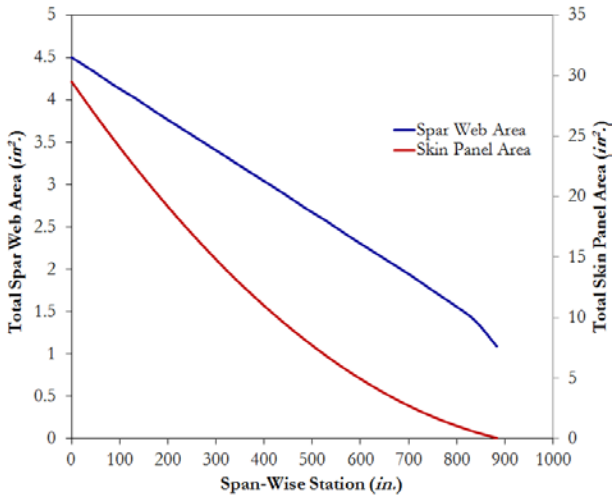

Fig. 63 Total spar and skin panel area vs. span-wise station

A parametric study was performed to investigate the relationship between the occurrence of flutter and wing geometry using the method presented by *Harris*[73] and *Leibeck et al*[74]. In conjunction with the trade study presented in Section 4.4, the decision to utilize a wing planform with an AR of 14.1 was confirmed to be below the flutter limits set by the aforementioned publications and therefore demonstrating an achievable structural solution with integrity. Figure 64 presents the results of this parametric study.

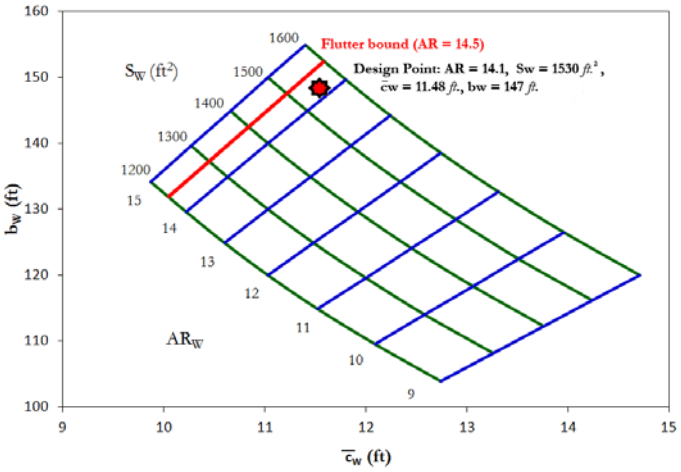

Fig. 64 Parametric study of aspect ratio vs. wing area. The flutter bound for a fully composite wing is shown in red and is equal to an aspect ratio of 14.5.

8.4 Load Alleviation System

To improve safety concerns associated with excess wing loads at high angles of attack, the UACC implemented a system of spoilers to reduce lift produced by the outboard section of the wings at the angles of attack higher than approximately 10°. Electromechanical actuators located in the wing deploy spoilers by the sub-system's ACEs when the PFCC determine the airspeed and angle of attack to broach the predetermined safety limit. This prevents an unintended overload of the wing primary structure therefore increasing the safety and extends the airframe's useful life. More information regarding this system can be found by reviewing the accompanying large scale drawing SY – 4.0.

8.5 Fuselage and Empennage Structure

The structure of the fuselage consists of eight major sections that are manufactured using carbon laminated composites with varying thickness, depending on the curvature of the cross section. The outer skin is stabilized by adhesively-bounded longerons made by the same material. The major sections of the fuselage are connected to each other through titanium links and are sealed to prevent leakage of pressurized atmosphere. The floor panels inside the fuselage are supported by carbon fiber lateral and longitudinal beams, the latter of which contains the seat trails allowing for the installation of passenger seats in any selected pitch by the customer. The wing box structure is extended through the fuselage and is anchored to three reinforced frames that carry the load from the wings to the fuselage structure as seen in Fig. 65. The middle fuselage section contains the

landing gear well, as well as the reinforcing keel beam that increases the stiffness of the middle fuselage structure. The pressure vessel is sealed in the front and back by two pressure bulkheads. The front bulkhead is consisted of a highly reinforced, slightly curved ball that separates the cabin space from the radome, and is sandwiched between layers of the skin of the nose section (referred to as Section 41). The aft pressure bulkhead is a dome-shaped, stabilized structure that intersects the fuselage's inner skin at an angle of 60º and is sandwiched between the skin layers of the aft fuselage section (referred to as Section 47). Figure 65 presents a view of the 3D CAD model constructed for Albatross.

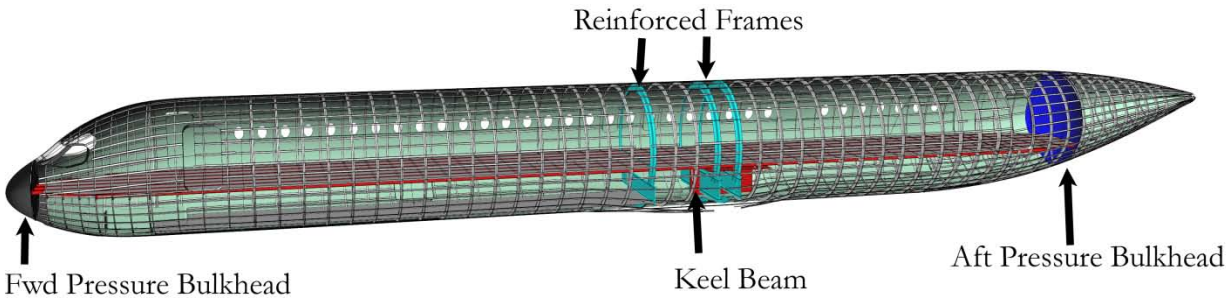

Fig. 65 Fuselage Structure

The carbon laminated composite structure used for the skin of the fuselage allows utilization of larger windows due to the increased tolerance to fatigue brought on by pressurization cycles[75]. Considering the corrosion resistivity of carbon laminated composite panels used for the fuselage structure, the cabin could be kept at higher levels of humidity and lower pressure altitudes with no adverse effects on safety or operational life of the structure. The vertical tail of Albatross features a similar structure to the wing in terms of architecture and composite material application, however, it utilizes three spars to provide fault tolerance in case of an APU blade loss as discussed in Sec. 6.8. The horizontal tail is supported on a trunion which is secured to the upper vertical tail structure. The horizontal tail incident angle is varied by a triple redundant actuation system installed inside the vertical tail of the aircraft. Figure 66 presents the general structural arrangement of the empennage of Albatross.

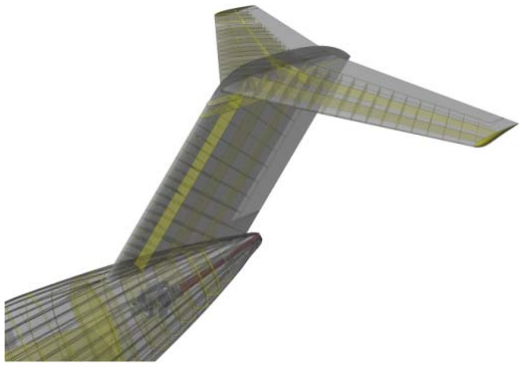

Fig. 66 Empennage Structure

8.6 Manufacturing Methods

Due to the utilization of carbon laminated composites, Albatross is able to be manufactured using modern automated composite laying technology. This technology allows for manufacturing of large, continuous pieces of structure rather than the conventional method that relies on manufactured sub structures to create larger assemblies. The fuselage structure of Albatross is to be manufactured in computer controlled, rotary matrix laying barrels that will be cured with heat and pressure to ensure obtaining the required mechanical properties. Wing skins are to be laid in large, continuous pieces, eliminating the possibility of small surface misalignments. If the wing surfaces of Albatross are manufactured using conventional methods, these common misalignments (present at manufacturing or created during the service life) can lead to the tripping of the boundary layer, therefore making the implemented NLF technology less effective. Compatibility of the structural design of Albatross with modern manufacturing methods allows for higher production rates and buy-to-fly ratios. Higher rates of production allows for substantial reduction in the overhead cost per plane and higher buy-to-fly ratios allow for significant reductions in the cost of raw materials used to build the aircraft.

To allow for distributed manufacturing of the airframe of Albatross, the structural assembly of the aircraft was divided into sub-assemblies. This will allow for a greater manufacturing flexibility, as well as allowing the producer to utilize skilled and diverse sets of labor force, therefore increasing the quality of the product while reducing the ultimate cost. The airframe breakdown was performed in a manner to allow air transportation of sub-assembly parts using regular cargo aircraft, therefore reducing the cost of distributed manufacturing as cargo aircraft capable of transporting oversized cargo will not be needed. The manufacturing breakdown of Albatross is presented in Sec. 8.8.

Albatross

Structural isometric drawing (bottom) and material distribution (right). The structural isometric is false-colored to make the floor beams, main spars and folding mechanisms more visible.

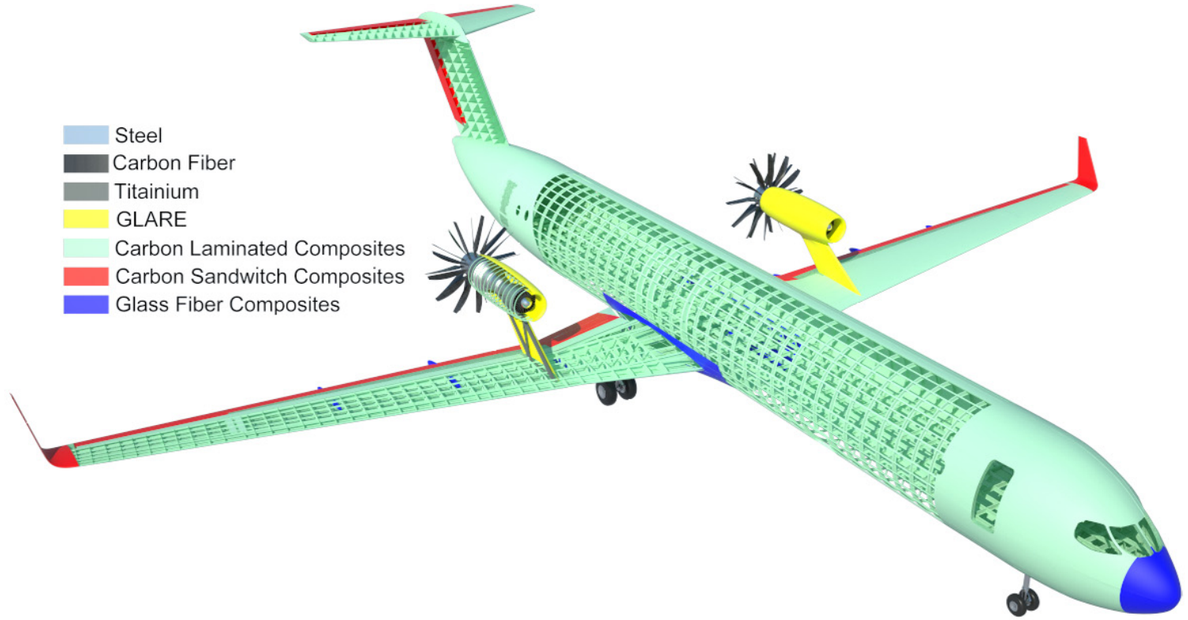

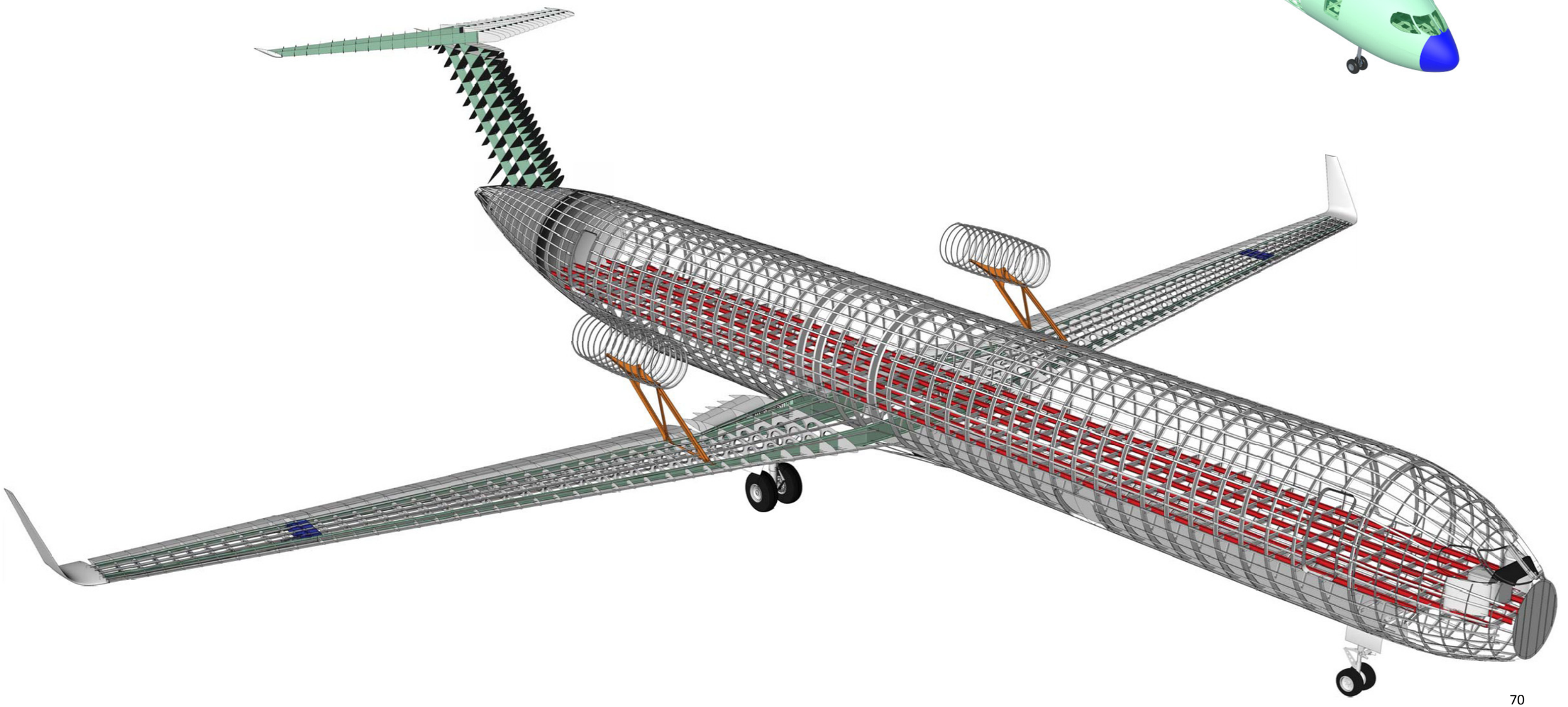

Albatross

Manufacturing Breakdown of Albatross. Naming of the sub-assemblies follows the Boeing's naming convention.

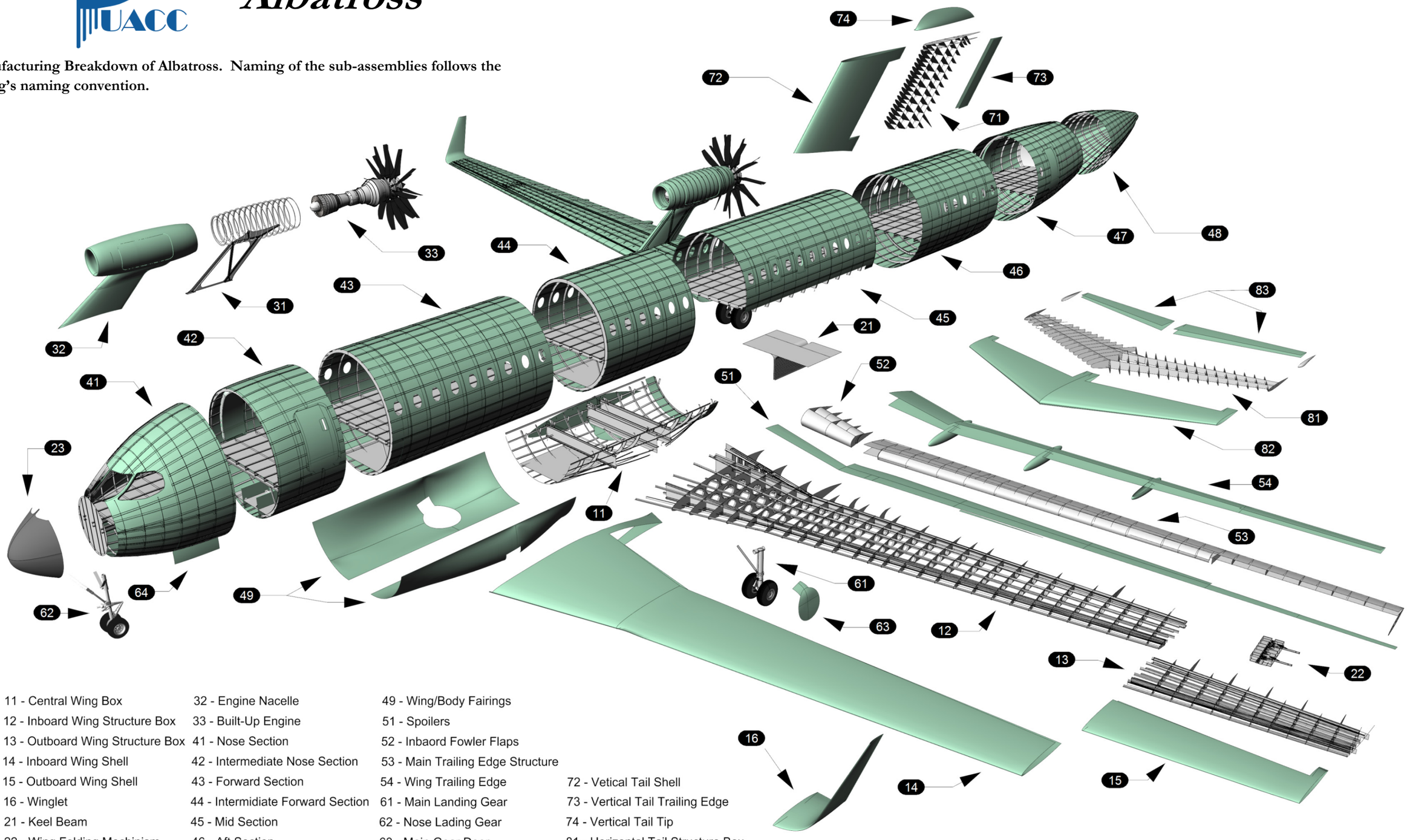

11 - Central Wing Box	32 - Engine Nacelle	49 - Wing/Body Fairings	
12 - Inboard Wing Structure Box	33 - Built-Up Engine	51 - Spoilers	
13 - Outboard Wing Structure Box	41 - Nose Section	52 - Inbaord Fowler Flaps	
14 - Inboard Wing Shell	42 - Intermediate Nose Section	53 - Main Trailing Edge Structure	
15 - Outboard Wing Shell	43 - Forward Section	54 - Wing Trailing Edge	72 - Vetical Tail Shell
16 - Winglet	44 - Intermidiate Forward Section	61 - Main Landing Gear	73 - Vertical Tail Trailing Edge
21 - Keel Beam	45 - Mid Section	62 - Nose Lading Gear	74 - Vertical Tail Tip
22 - Wing Folding Mechinism	46 - Aft Section	63 - Main Gear Door	81 - Horizontal Tail Structure Box
23 - Radome	47 - Intermediate Tail Section	64 - Nose Gear Door	82 - Horizontal Tail Shell
31 - Engine Pylon	48 - Tail Section	71 - Vertical Tail Structure Box	83 - Horizontal Tail Trailing Edge

9. Stability & Control

9.1 CG Travel

Static stability of the configuration was achieved by performing a parametric study of the impact of the longitudinal location of the wing on the magnitude of static margin using the methods presented by *Roskam*[76]. Mass properties analysis of Albatross indicated that a CG travel range equivalent to 19.8% of mean aerodynamic chord of the aircraft is likely in a maximum range mission. A target positive stick free static margin of 15%[77] was selected for the mid-cruise segment of the flight to ensure the inherent static stability of the aircraft considering the variations of the location of the CG during flight. The result of this parametric study can be seen in Figure 67.

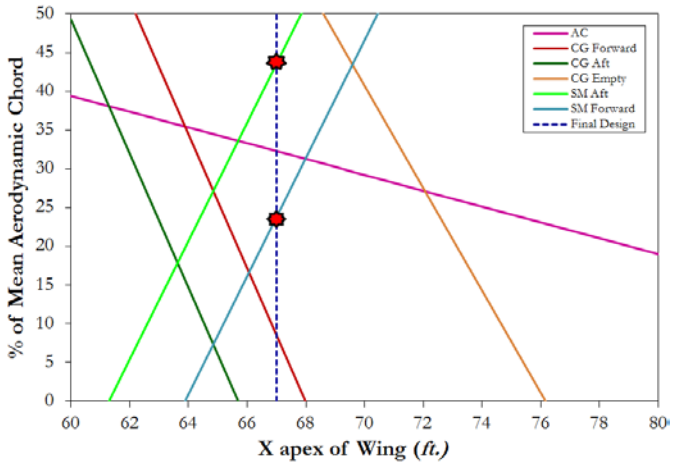

Fig. 67 Wing location trade study

UACC concluded that a longitudinal wing apex of 67' will provide sufficient positive static margin at forward and aft locations of the CG, therefore ensuring the maintenance of the static stability of the aircraft under all loading conditions.

9.2 Tail Sizing and Trim Maintenance

The empennage of Albatross was sized to satisfy basic stability and control requirements set by MIL-F-8785[78] and recommended by *Roskam*[79] as well as being able to initiate the takeoff rotation of the aircraft MIL-F-8785 recommends that in order to maintain static longitudinal stability the air vehicle must possess negative values of C_{m_α} and $C_{m_{\dot{\alpha}}}$ at all flight conditions. A horizontal tail area of 342 $ft.^2$, capable of maintaining a C_{m_α} and $C_{m_{\dot{\alpha}}}$ of at least -0.2 rad^{-1}, was selected by performing a

parametric study that varied the area of a generic horizontal tail planform and then computed the corresponding C_{m_α} and $C_{m_{\dot{\alpha}}}$ using methods presented by *Roskam*[80]. A trim diagram was generated assuming the horizontal tail was capable of varying its root incident angle from -15° to 5° in order to verify the capacity of the plane to maintain trim under all loading conditions. This trim diagram can be seen in Fig. 68.

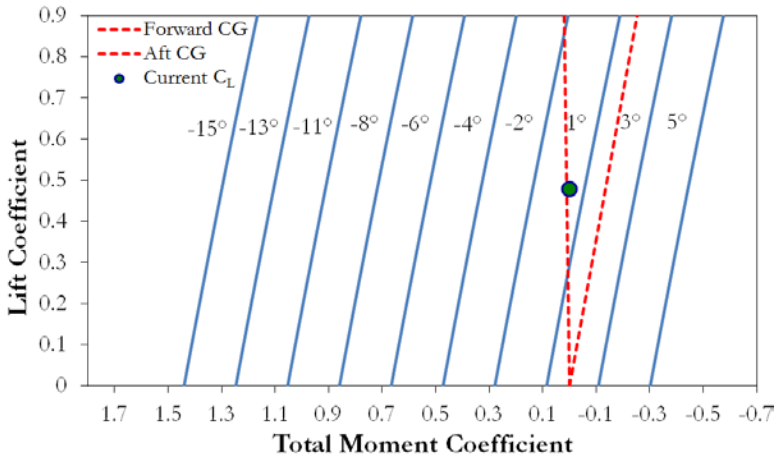

Fig. 68 Trim diagram for Albatross

9.3 Stability & Control Derivatives

MIL-F-8785[81] requires that every aircraft should have a neutral point located behind the most aft center of gravity in order to maintain static longitudinal stability in all flight conditions. The location of the aircraft's neutral point was determined using the method presented by *Roskam*[82]. A selection of the results is presented in Table 11. As it can be seen from this table the location of the free stick neutral point, NP_{free}, in terms of wing chord is always behind the location of the center of gravity in all flight segments.

Table 11 Location of CG, aerodynamic center, and corresponding free stick neutral point at takeoff, cruise, and landing

Segment	Takeoff	Cruise	Landing
$\bar{x}_{cg}$	0.0168	0.0388	0.0884
$\bar{x}_{ac}$	0.1127	-0.0252	-0.0238
NP_{free}	0.4578	0.1902	0.4882

In order for the aircraft to remain statically stable, the pitching moment coefficient due to the angle of attack (C_{m_α}), and pitching moment coefficient due to angle of attack rate derivative ($C_{m_{\dot{\alpha}}}$) both should be negative. In order to verify the lateral and directional static stability of the aircraft, yawing-moment coefficient-due-to-sideslip derivative (C_{n_β}), and rolling-moment-coefficient-due-to-sideslip derivative (C_{l_β}) were computed as *Roskam* suggests to maintain lateral and direction static stability, C_{n_β}, should be positive while C_{l_β} should have a negative value. These derivatives were computed using methods presented by *Roskam*[76] and can be seen in Table 12.

Table 12 Important longitudinal and lateral-directional static stability derivatives

Segment	Takeoff	Cruise	Landing
C_{m_a} [rad-1]	-9.5362	-3.0017	-3.6253
$C_{m_{\dot{a}}}$ [rad-1]	-9.0763	-18.0427	-9.3978
C_{n_β} [rad-1]	0.0022	0.0018	0.0158
C_{l_β} [rad-1]	-0.1707	-0.827	-0.02927

9.4 Aileron Sizing

Due to the acceptability and availability of FAR-25 standards for commercial aircrafts, guidelines suggested by this code are used to estimate the size of the required ailerons for the aircraft. To estimate the size of the ailerons for this aircraft, a theoretical approach presented by Roskam was used. In the interests of brevity, this method is not presented in this proposal. The goal of achieving "level I" rolling qualities in the takeoff flight condition was pursued using the rolling time constants suggested by FAR-25. Assuming an individual aileron has a C_a/C_w equal to 20% starting at 77% of the half-span (following the flap), the outboard station of the aileron was calculated to be located at 98% of the half span. This aileron geometry was validated later during the analysis of the lateral directional flying qualities by fulfilling the rolling requirements defined in FAR-25.

9.5 Dynamic Stability

Considering that the RFP requested only the static stability analysis to be presented in the proposal, the results of the dynamic stability analysis and flight handling are not presented in their entirety in this proposal. Instead, the results of the most important segments of these analyses for takeoff, cruise, and landing are presented. Handling quality analyses performed using the AAA package indicates that Albatross is capable of achieving Level I and Level II flight handling characteristics in all segments of flight. Results are confirming the satisfaction of the regulations presented by FAR-25 and MIL- F-8785 with regard to the time constants and damping ratios, in particular those pertaining to phugoid and short period oscillation modes.

In order to verify longitudinal dynamic stability, dynamic stability derivatives were evaluated along the x, y and z axes to determine the transfer functions and characteristic equations for Albatross. The methods applied were obtained from USAF Stability and Control DATCOM[83]. Natural frequencies and damping ratios for short period oscillations, and phugoid mode, were calculated based on the methods presented by *Roskam*[84]. Values of short period and long period natural frequencies and damping ratios can be seen in Table 13 for takeoff, cruise, and landing conditions.

Table 13. Dynamic longitudinal stability characteristics for various flight conditions

Flight segment:	Takeoff	Cruise	Landing
T_{2_P} sec.	663	-----	370
$T_{1/2_P}$ sec.	-----	1101	-----
$Level_P$	II	I	I
$Level_{\xi,SP}$	I	I	II
$\omega_{n,S.P}$ (rad/sec^{-1})	1.5804	2.5053	1.6082
$\omega_{n_{P,long}}$ (rad/sec^{-1})	0.1747	0.1099	0.2455
ζ_{SP}	0.443	0.377	0.494
$\zeta_{P,long}$	-0.006	0.006	-0.008

10. Environmental Impact

10.1 Biofuel Analysis

Environmental responsibility is a top priority for current commercial aviation. The implementation of an environmental tax requires a solution to reduce the influence of such a tax on the cost of commercial flight. The most significant contributor to the environmental tax is the tax on carbon emissions. Techniques must be developed to mitigate the emission of carbon considering the possible introduction of the environmental tax. Several methods to reduce CO_2 emissions are increasing the efficiencies of the propulsion system and utilizing NLF technologies, both of which are present in Albatross. This already significant reduction can be augmented by the use of low carbon footprint fuels. The use of such fuels can result in an 80% reduction in the net carbon output, and a corresponding reduction in carbon taxation[85].

Of all the alternative fuels, biofuels are the only ones that result in a net reduction of carbon footprint due to the fact that their biological sources sequester CO_2 as they grow. Ideally, this results in a carbon neutral product; however, the use of biofuels represents an 80% reduction in carbon emissions due to fossil fuel use in their production.

For their benefits, biofuels also bring some challenges. If their biological sources are not chosen carefully, they could compete for arable land with food crops, which is not a sustainable option. Additionally, an ideal biofuel would require no modifications to aircraft or infrastructure of the airports. To ensure this, ASTM International established a new framework, known as D 7566, to classify fuel blends containing synthetic* hydrocarbons. D 7566 refers back to the requirements for traditional jet fuels, D 1655. This ensures that all synthetic fuels are "drop in" fuels, i.e. they require no changes to any piece of system or infrastructure[86].

As a result of these requirements, the ideal biofuel would consist of hydrotreated renewable jet (HRJ) derived from sources such as japtropha, camelina, algae, and halophytes[87]. It is created by extracting and filtering the oil from the feedstock and then heating and hydro-treating it to correct

* Synthetic refers to both biologically and fossil fuel derived manufactured fuel, e.g. Coal-to-Liquid and Biodiesel

its molecular structure[88]. After extraction, the feedstock residue can be converted to methane and burned to create the electricity needed to power the process, as well as selling electricity back to the grid[89]. This can bring the carbon emissions reduction up to 100%, or even as high as 124% because the energy that is sold back to the grid offsets energy that would otherwise be produced from fossil fuels[90]. HRJ is chemically similar to traditional jet fuel and is considered a "drop-in" fuel[91]. The small differences between HRJ and traditional jet fuel can actually be beneficial, as the use of HRJ can result in a decreased fuel burn of 3%[92]. HRJ feedstock can be grown in areas not suitable for food crops, thus removing arable land competition. The most promising biofuel is algae derived HRJ due to its ability to be grown in polluted water, salt water, and deserts. A typical alga is shown in Fig. 69. It is also capable of producing fifteen times more oil per square kilometer than other biofuel crops[93], making it the best candidate for large scale production. Also, an algal biofuel facility could be attached to a fossil fuel power plant, and use the power plant's exhaust to feed the algae. Because algae thrive on CO_2, their growth will be encouraged while sequestering the plant's CO_2 emissions[94]. Currently, D 7566 is meant only for fuel blends; however, the Commercial Aviation Alternative Fuels Initiative is working with ASTM International to add HRJ to D 7566 by the end of 2010[95].

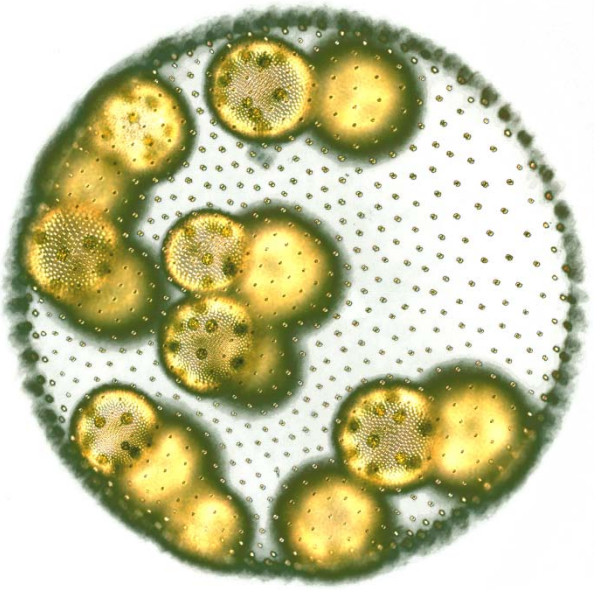

Fig. 69 Microscopic view of an alga

Due to carbon taxes and the emerging potential of algae-based fuel, as well as other technologies that directly convert sugar into jet fuel by use of microbes or catalysts[96], the projected costs of HRJ have a large value of uncertainty. Additional cost analysis of HRJ can be found in section 13.3.

10.2 Environmental Tax Modeling

In order to include the effects of the proposed environmental taxation methods on the aircraft's Direct Operating Cost (DOC) and Cash Airplane-Related Operating Costs (CAROC), a method based on the work presented by *Schwartz* et al.[97] was adopted and used to perform flight path optimizations presented in Sec. 13.1. This method accounts for four main components of the environmental tax. The most significant component is the carbon tax, which is computed as 0.33¢ per gallon fuel burned. *Schwartz* suggests that the carbon emissions, for any given propulsion system, are a linear function of fuel burn, and therefore are independent of altitude*.The combined taxation accounting for NOx emissions, Aviation Induced Cloudiness (AIC), and high altitude cirrus clouds were computed as a multiplier to be added to the baseline carbon tax (as a percentage). Given that *Schwartz* provides values for the variation of the influence of each of these forms of emissions as a function of altitude, her model was adopted to compute the total environmental tax imposed on the operation of the aircraft. Figure 70 presents the variation of taxable pollutants normalized to one, based on CO_2 emissions, which are assumed constant, independent of altitude. Equation 6 is used to compute the environmental tax in U.S. dollars,

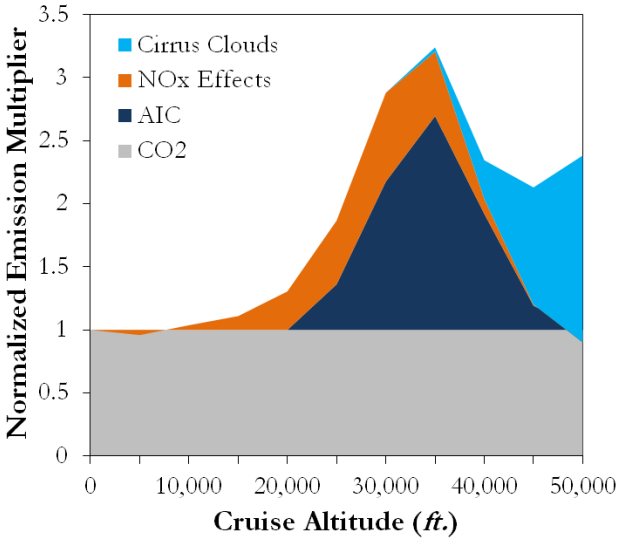

Fig. 70 Environmental multiplier vs. altitude

$$C_{ENVTAX} = \underbrace{0.33}_{\substack{carbon \\ emissions}} \cdot \left(1 + \sum_{1}^{3} M_i\right) \quad , \qquad (6)$$

where M_i is the corresponding normalized emission multiplier as shown in Fig. 70.

* Note that the variation of altitude has a significant effect on the block fuel burn of the aircraft, therefore affecting the total carbon emissions of the airplane

10.3 Noise Verification

Historically, the noise associated with open fan engines has been a determining factor in preventing them from becoming a mainstream type of commercial aircraft propulsion system. For example, there have been instances where the acoustic pressure from an open fan has worn the paint off nearby points on the aircraft body – these engines are LOUD. Therefore, considerable analysis has been performed in order to justify the use of open fans as well as to provide solutions that will make their use feasible.

The ICAO Chapter 4[98] noise requirement defines three main noise measurement positions for the processes of noise certification of the aircraft. Flyover noise of the aircraft is measured on the ground at a point 6,500 *m.* away from the start of the takeoff roll, while the approach noise is measured on the extended centerline of the runway 2,000 *m.* away from the edge of the landing field. The lateral noise for the aircraft is measured on a line parallel to the axis of the runway 450 *m.* away from the centerline, at the location with the maximum noise level. Figures 71 through 73 illustrate these noise measurement reference points as specified by ICAO Chapter 4.

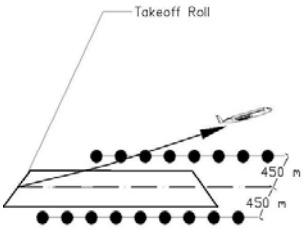

Fig. 71 Lateral Noise Reference positions

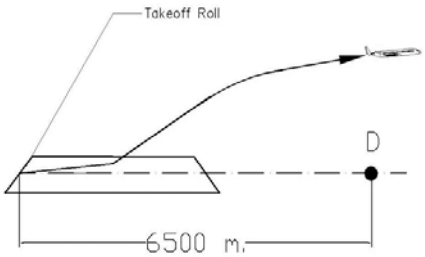

Fig. 72 Flyover Noise Reference Point (D)

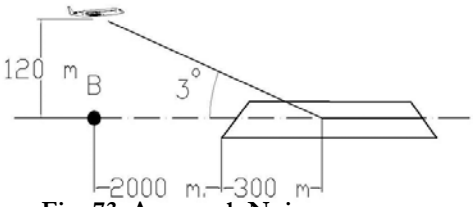

Fig. 73 Approach Noise, Reference Point (B)

ICAO Chapter 4 also cites the maximum value of the acceptable noise for each of the described reference measurement positions, and allows a cumulative deviation of 3 *dB* from the reference noise levels, while limiting the deviations at each point to 2 *dB*[99]. UACC aims to reduce the noise by of 10 Effective Perceived Noise in Decibels *(EPNdB)* compared to the ICAO-4 values listed in Table 14. In order to ascertain the feasibility of a reduction

Table 14 Maximum noise levels, ICAO Ch. 4

Position:	ICAO-Ch. 4 (*EPNdB*)
Lateral Noise	94
Flyover Noise	89
Approach Noise	98

of this magnitude, it is necessary to develop an accurate model for the prop fan noise, the most significant contributor to overall noise levels.

10.4 Far-Field Open Fan Noise Estimation

Using a method derived by *Hanson*[100], UACC developed an analytic procedure utilizing MAPLE, a symbolic computation software. Open fan noise is famously hard to model, yet *Hanson*'s model is confirmed to be accurate within 3 *dB*. This model takes into account both harmonic load interactions and acoustic interactions between the two blade rows. Vortex noise is not considered because it contributes negligibly to the overall noise level in this regime (high RPM). Altogether, *Hanson*'s method allows calculation of the complex acoustic interaction between the blade rows, providing an accurate estimation of the largest overall contribution to open fan noise – the inter-row interference component. The output of the program is a list of complex valued pressure waves as functions of observer distance and time (the real parts of several of these are shown in Fig. 74). A phase offset for each harmonic contribution is included as well. The phase offset is necessary for exact calculation of overall acoustic pressure level because varying the phase of each harmonic can cause a range of both constructive and destructive interference effects upon summation. *Hanson*'s model provides an exact value for the phase offset of each harmonic contribution, which allows a more precise estimation of the overall acoustic pressure level compared to more traditional approaches

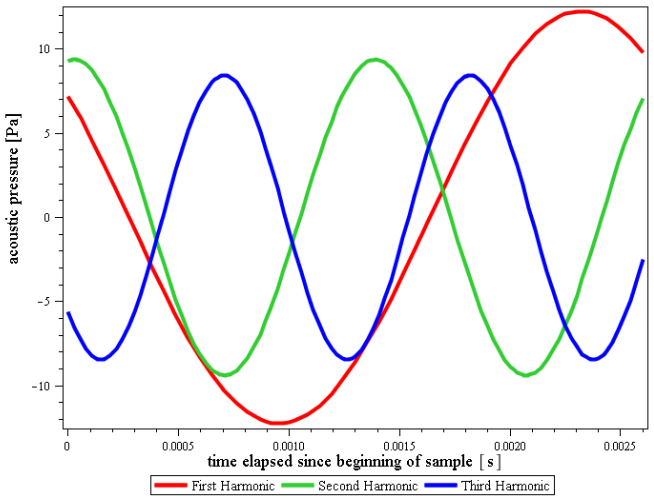

Fig. 74 Acoustic pressure modes

Difficulties in this approach include obtaining accurate harmonic lift and drag coefficients for individual blades. Harmonic lift and drag coefficients detail the additional lift and drag response of each blade due to unsteady inflow. A general unsteady inflow can be expressed as a linear combination of inflows with Fourier representations. The unsteady component of response can be represented in a similar manner. These coefficients are an important part of the noise interference calculation because it is the impingement of the unsteady flow on the second blade row that creates the bulk of this interference noise.

There is no accessible literature within the public domain on a general method to calculate the harmonic lift and drag coefficients for a given blade geometry. Therefore, UACC consulted ESDU Data Item 96027[101], which provides a method for estimating harmonic lift coefficients due to non-axial inflow into the propeller disk. A critical input into this procedure is an angle measuring inflow deviation from the axis of the rotor. UACC reasoned that a proper approximation for this parameter would be a mean angle of outflow deviation from the forward blade, allowing at least an order of magnitude estimation of the harmonic lift and drag coefficients due to blade row interaction.

Using a typical slender high advance ratio blade geometry, UACC determined that the mean axial flow deviation angle was approximately 6.4°. Inputting this into the ESDU 96027 procedure, UACC derived functions for the harmonic lift and drag coefficients up to the third harmonic. Inputting these derived functions into *Hanson*'s procedure allows the calculation of prop noise for any combination of observer angle and radial distance from the propeller hub.

Treating the takeoff case and plotting the *dB* level for several "virtual microphones" placed along the runway, it was determined that the loudest noise is generated when the aircraft reaches takeoff speed and is closest to the observer (450 *m.* per ICAO-Ch.4). Results indicate a preliminary maximum sideline noise of 109 *dB*, which considerably exceeds the ICAO Chapter 4 requirement of 94 *EPNdB* if no noise reduction techniques are utilized.

As a solution, UACC proposed that during takeoff, a clutch mechanism shall disengage the forward blade row on each engine. This eliminates most of the interference noise between the two blade rows. Choosing to disengage the forward rather than aft blade row generates a greater noise reduction, since it is the unsteady flow caused by the forward blade row's rotation that produces the bulk of the interference noise. With this setup, the aft blade row's individual noise contribution needs to be modeled while accounting for the now minor disturbances caused by the stationary forward blade row. A propeller noise estimation presented in the NASA Technical Report 32-1462[102] gives 76 *dB* for takeoff conditions with disengaged forward blade rows. This is of course significantly lower than the noise during dual blade operations. Though this number seems to be an optimistic estimate, NASA authors insist that their method is accurate to within 3 *dB*. At this decibel level, propeller noise is no longer the only considerable contributor to overall noise level. Therefore, other noise sources must be considered to yield a reasonable estimation of the aircraft's total noise level.

In addition to takeoff, flyover and approach noise must be considered. Assuming the that the forward blade row remains disengaged during these cases, UACC has ascertained that the maximum flyover noise is approximately 88 *dB*, while maximum approach noise is approximately 87 *dB* measured from positions determined by ICAO ch.4. Figure 75 details the results of the computations, showing dB levels for both flyover and approach noise respectively.

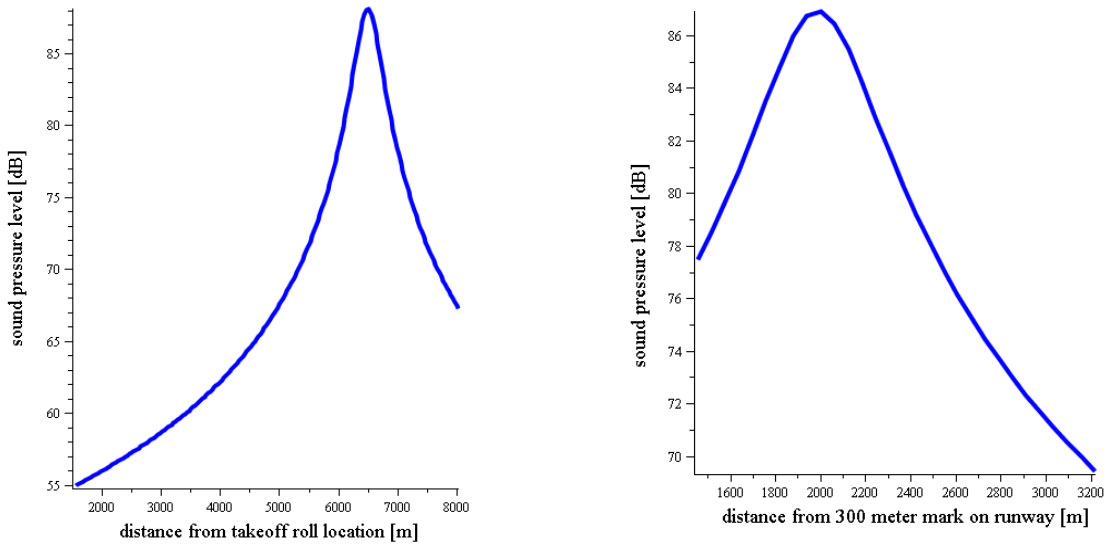

Fig. 75 Flyover noise as measured from 6500 *m.* from the takeoff roll. Maximum sound pressure level is 88 *dB* (left). Approach noise as measured 2,000 *m.* from the 300 *m.* mark. Maximum sound pressure level is 87 *dB* (right).

10.5 Total Far-Field Noise

Traditional sources of noise include air frame noise, compressor noise, combustor noise and jet noise. According to ESDU Data Item 02020*, given the extremely high bypass ratio of the engine (and as a result significantly reduced engine jet speed), the contribution of jet noise is negligible. ESDU data items belonging to the noise series[103,104] provide methods to calculate the rest of these sources of noise via empirically verified models. Using these, UACC calculated that airframe noise accounts for approximately 70 *dB*, while compressor and combustor noise add an additional 72 *dB*. Logarithmically summing these values gives approximately 85 *dB* for the maximum sideline noise (450 *m*. offset from the runway). This noise level is almost 10 *dB* below ICAO-4 requirements for takeoff, which was the initial noise goal for the Albatross configuration. So, it seems that the open fan configuration is indeed feasible as long as the forward blade row is not engaged while the aircraft is close to the ground. Once the aircraft begins to climb, the forward blade row will be engaged to save fuel. Figure 76 presents the maximum sideline noise distribution for Albatross during takeoff.

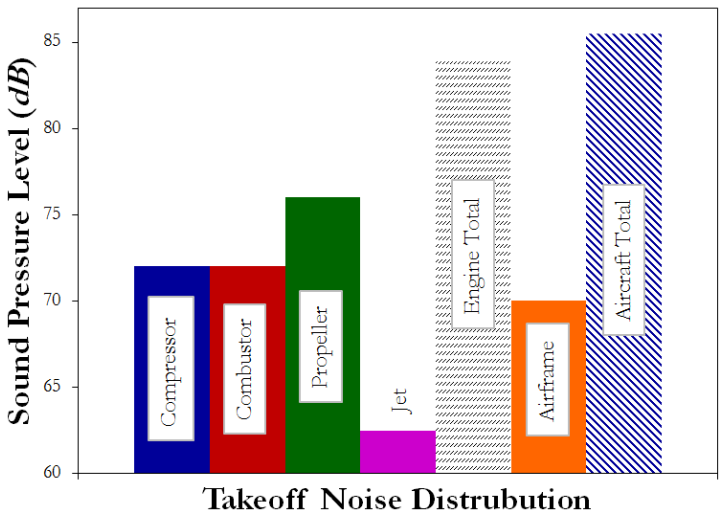

Fig. 76 Maximum sideline noise distribution for Albatross during takeoff. The jet contribution is relatively negligible. The propeller contributes the most to overall aircraft noise.

* It is shown that jet noise varies with the 8th power of the engine jet speed, which is inversely proportional to the bypass ratio of the engine.

10.6 Cabin Noise

Using *Hanson*'s method, the unattenuated noise level was calculated at the fuselage side wall adjacent to the engine rotor and found to be 151 *dB*. ESDU Data Item 02008[105] indicates that at the dominant frequencies (blade passage frequencies and their lower harmonic), cabin insulation can attenuate noise by approximately 30 *dB*. This is a typical number, but further reductions need to be achieved in order to make open fan use feasible. One advantage to the Albatross configuration is that lavatories are placed at the points of greatest noise intensity. Not only will passengers not be present here for extended periods of time, but also the lavatories might themselves provide acoustic insulation. Though adding insulation may help, the real difference will come with an investment in an active noise cancellation system. *Zimcik*[106] claims that an additional 20-30 *dB* of attenuation is possible with installation of an active noise suppression array. Assuming conservative advances in this technology (especially noise cancellation algorithms), a total noise reduction of 60 *dB* between improved insulation and the use of active noise cancellation is easily attainable – yielding an approximate 90 *dB* cabin noise, which is on par with modern configurations. It should also be noted that this is the maximum cabin noise, calculated at points in the cabin nearest to the engines. Passengers sitting farther away will experience lower noise levels in general. Though noise has been a traditional concern with open fan systems, UACC finds that noise can be managed to an acceptable level through the use of both temporary disengagement of forward blades, and the use of active noise suppression technology.

11. Performance Validation

11.1 Takeoff Performance

The required takeoff field length for Albatross is determined by applying relations presented by ESDU Data Item 85029 [107] and considering the ground effect on generated lift and drag[108]. It is assumed that the aircraft uses the previously sized flaps during takeoff without assistance from leading edge high lift devices, making the maximum lift coefficient ($C_{L_{max}} = 2.2$) attainable. The average kinetic friction coefficient was computed using the data presented by *Roskam*[109] to be 0.02, assuming a conventional tarmac mix, as used in the United States.

The takeoff trajectory was computed for normal takeoff and can be seen in Fig. 77. Assumptions regarding takeoff performance computations and the results of this analysis are presented in Tables 15 and 16.

Table 15 Takeoff Condition

$C_{L_{max_{TO}}}$	2.2
$C_{DO,TO}$	0.0328
$L/D\|_{TO}$	16
Π_{TO}	0.95

Table 16 Takeoff Performance

$V_{S_{TO}}$	114 *kts.*
V_{LOF}	137 *kts.*
S_{TO}	7,300’
$S_{TO,G}$	4,996’

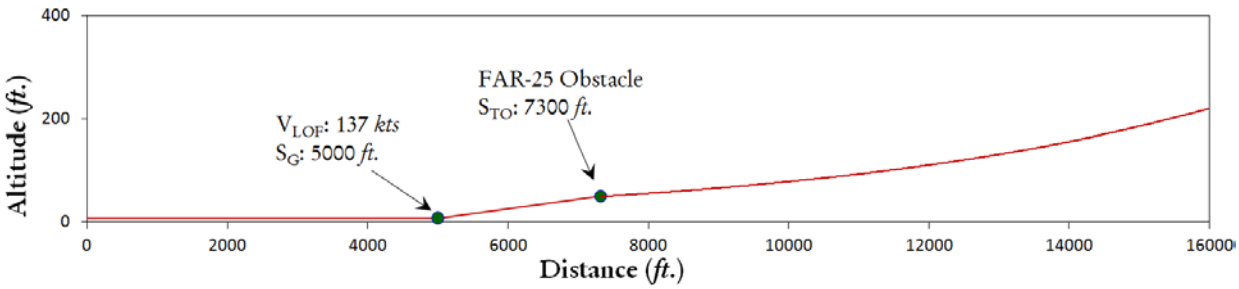

Fig. 77 Takeoff trajectory

11.2 Climb Performance

In order to verify that Albatross’ performance agrees with federal regulations, the climb gradient was compared with the values set by various sections of FAR 25. §25.121 requires all commercial aircraft to be able to maintain a climb gradient of at least 1.2%. At an altitude of 10,000’,

FAR §25.111 requires that a commercial aircraft should be able to maintain the same climb gradient with only one engine operative. Additionally, FAR §25.105 requires that the climb gradient in the transition phase between takeoff and climb should be no less than 2.4%. The result of the climb gradient analysis can be seen in Table 17, which indicates that all FAR requirements are satisfied.

Considering the high bypass ratio of the engine used and the requirements for an operational ceiling of 41,000', analyses were performed to verify that Albatross is capable of achieving this max operational ceiling. The operational ceiling is defined as the altitude at which the rate of climb is equal to 150 *ft./min.* Using the engine performance map developed for the power plant of Albatross, it was estimated that the ceiling rate of climb would occur at 43,000' in ISA conditions. At this altitude, the specific excess power available to the pilot is 396 *ft./min.*, which allows for a climb gradient of 0.6 %. Figure 78 presents the climb performance for Albatross.

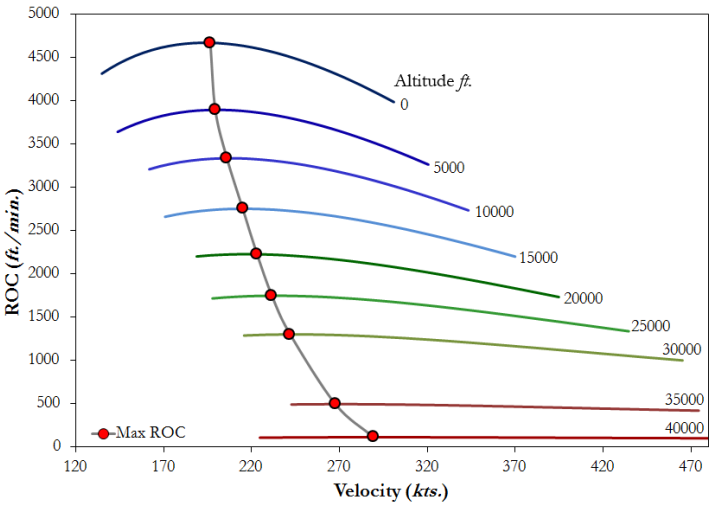

Fig. 78 ROC vs. velocity at various altitudes. Ceiling occurs at 43,000', corresponding to a ROC of 150 *ft/min*

Table 17 Results of climb gradient analysis, along with corresponding FARs

Regulation	Required Climb Gradient	Achieved Climb Gradient
FAR §25.121 Takeoff	1.2%	1.9%
FAR §25.111 Takeoff OEI	1.2%	1.9%
FAR §25.105 Transition Phase	2.4%	2.8%

11.3 Max Cruise Speed Validation

In order to verify the RFP requirements relating to cruise speed performance, thrust required to maintain level flight was computed using Equation 6:

$$T_{req} = \left(\frac{C_{D0_{clean}} \varrho S_w V_{Cr_{max}}^2}{2\cos(\alpha + \varphi_T)} \right) + \left(\frac{2W_{Cr}^2 B_{DP_{clean}}}{\varrho S_w V_{Cr_{max}}^2 \cos(\alpha + \varphi_T)} \right) \quad . \qquad (6)$$

This value was plotted versus the installed thrust data obtained using GasTurb. Figure 79 presents a graph of thrust vs. velocity for both available and required thrust for the cruise altitude of 39,000'. It can be seen from this figure that the maximum cruise speed is equal to 498 *kts.* at an altitude of 39,000', which corresponds to 0.84 Mach, satisfying the goal set by the RFP for the maximum cruise speed (0.83 Mach). The velocity corresponding to maximum range was also determined from this analysis to be 467 *kts.* (0.787 Mach at 39,000'). The maximum excess thrust is estimated to be achieved at a speed of 360 *kts.* (0.607 Mach at 39,000'), which yields the maximum maneuverability and endurance within the flight envelope.

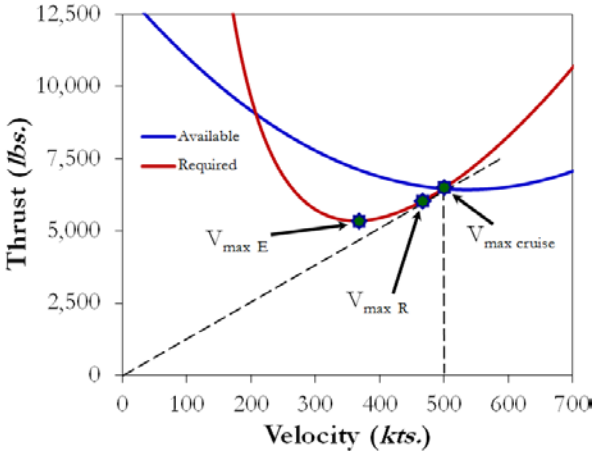

Fig. 79 Available & required thrust vs. velocity (*cruise*)

11.4 Fuel Burn Performance

Detailed analysis of the block fuel burn was performed to assess the economic advantages of Albatross over present day technology. Analysis was repeated for three different block ranges of 850, 1,200, and 3,500 *nm.* for 175 passengers, equivalent to a payload of 37,000 *lbs.* Figure 80 presents the results of this analysis. From this figure it is evident that for longer range missions, significant reductions in block fuel burn are attained by flying at higher initial cruise altitudes. The initial cruise altitude has a very minute effect on the block fuel burn of the aircraft for shorter ranges, such as the 1,200 *nm.* nominal block range specified by the RFP. This analysis also confirmed that the block fuel burn for a 1,200 *nm.* mission with 175 passengers is approximately 5,900 *lbs.* (corresponding to a fuel burn per passenger of 33 *lbs./seat*), assuming an initial cruise altitude of 39,000'. This value is almost 6 % lower than the

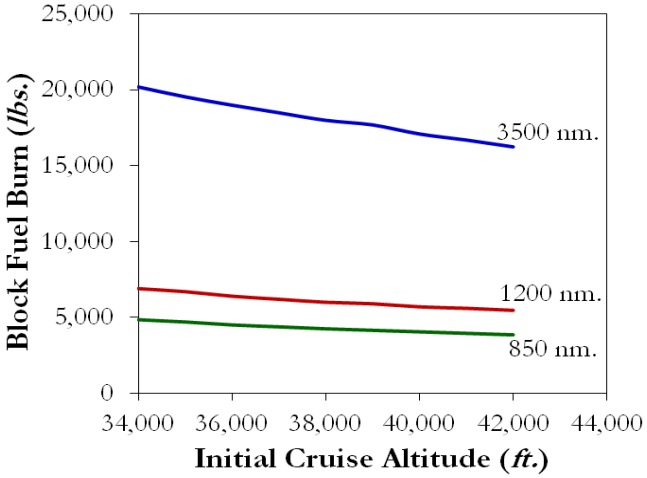

Fig. 80 Block fuel burn vs. initial cruise altitude for ranges of 3,500 *nm.*, 1,200 *nm.*, and 850 *nm.*

goal set by NASA N+1[110,111] study, confirming that the power plant technology level selected for Albatross is capable of satisfying the market's needs.

A payload-range chart was also constructed for Albatross and is presented in Fig. 81. Assumptions made for this analysis are presented in Table 18.

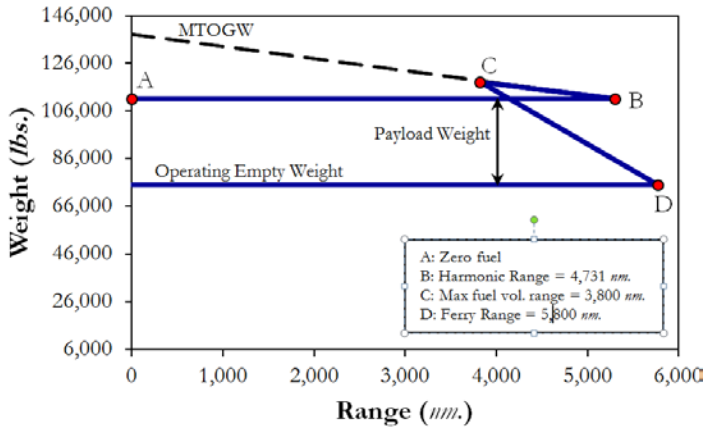

Fig. 81 Payload-Range chart

Table 18 Assumptions for payload range curve

T_{avail}	9,800 *lbs.*
α	2°
Mach	0.8
$C_{L_{opt,MaxR}}$	0.52
ICA	39,000'
C_{D_0}	0.019
TSFC	0.46 *lb./hr.-lb.*

11.5 Landing Trajectories

The method presented by ESDU Data Item 84040[112] was used to estimate the landing distance for the aircraft computed assuming a Maximum Landing Weight (MLW) of 114,996 *lbs.* MLW is defined by the RFP as the maximum zero-fuel weight (110,390 *lbs.*), plus fuel reserve for the longest range and highest payload for the aircraft (3,572 *lbs.*). The ground effects are taken into account in this analysis, for which the results are presented in detail in Table 19. Figure 82 presents the results of the simulation of the landing trajectory of the aircraft.

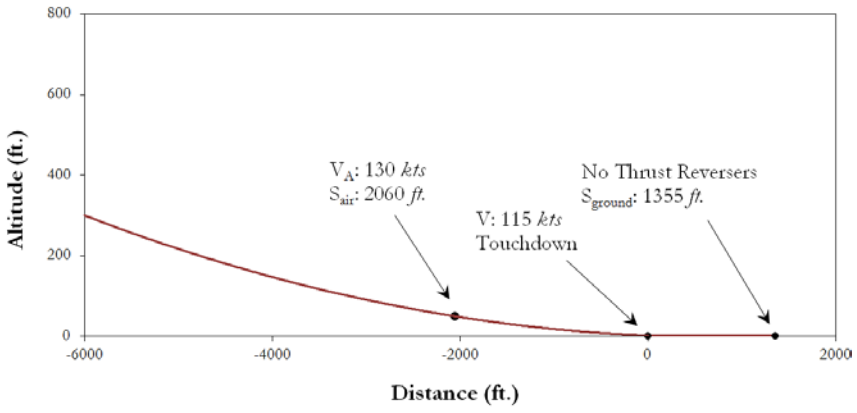

Fig. 82 Landing Trajectory for MLW of 114,996 *lbs.*

Table 19. Landing performance

Δ_n	0.1
$\bar{\gamma}$	0.03
V_{S_L}	100 *kts.*
V_A	130 *kts.*
S_{air}	2,060'
S_{LG}	1,355'
S_L	3,411'

11.6 One Engine Inoperative Conditions

Considering that the engines of Albatross are installed on the wings away from the fuselage centerline, analysis was performed to insure that the design rudder is capable of maintaining the control of the aircraft at all flight conditions. The method presented by *Roskam*[113] was used to compute the maximum controllable speed in OEI conditions, as well as the necessary rudder deflection to cancel the induced yawing moment due the inoperative engine. The analysis was repeated for takeoff, climb, and cruise conditions. The result of which can be seen in Table 20.

Table 20 OEI performance

Flight Condition	Takeoff	Climb	Cruise
Altitude (*ft.*)	0	15,000	39,000
Minimum Controllable Speed (*kts.*)	156	300	480
Rudder Deflection (°)	43	39	38

From this analysis it was found that the present rudder control surface is capable of safely controlling the aircraft at maximum thrust available with one engine inoperative at all flight conditions. Also, it was determined that a double-hinged rudder control surface with a maximum deflection of 45° will be necessary for aircraft to possess sufficient OEI controllability, considering that double-hinged rudders produce a higher yawing moment coefficient.

12. Ground Operations

12.1 Compatibility with Airport Infrastructure

The design philosophy of Albatross dictated that in order to ensure the commercial success of the aircraft, the buyers should not need to modify their present day airport infrastructure to accommodate Albatross. To be compatible with present day gates and hangers in use by airlines to support Boeing 737 and Airbus A320 aircraft, it was decided that Albatross, as a viable replacement, should be able to have the same wingspan on the ground as the aforementioned aircraft. Therefore, a folding wing mechanism was employed to reduce the span of the wing during ground operations

and docking. Figure 83 presents Albatross in docking mode with folded wings and Fig. 84 presents Albatross during ground operations.

Fig. 83 Albatross in docking mode with wings folded

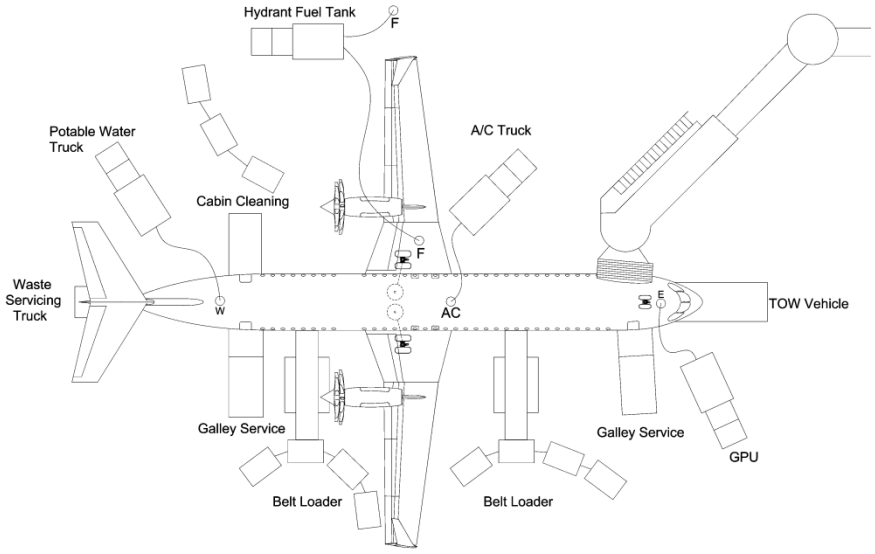

Fig. 84 Ground operation compatibility for Albatross

Considering that the wingspan of the aircraft is smaller than 150', which is the standard runway width for medium and large airports, Albatross is considered to be compatible with the majority of present day operating civilian runways and will not require any capital modifications to the runways worldwide.

Using the dimensions presented by *Roskam* for ground operational vehicles commonly utilized worldwide, a study was performed to ensure the compatibility of the configuration with ground support vehicles. It was concluded that Albatross with folded outboard wings is fully

compatible with airport ground support systems worldwide and will not require a modification in ground operational procedures. Despite the fact that Albatross uses an all-electric architecture, the ground power socket of Albatross is compatible with the generic 150 V_{AC} ground power units available in airports.

As previously discussed in Sec. 10.1, Ibis utilizes HRJ biofuels. Although it is derived from a different source than traditional jet fuel, it does not require a new set of refueling/defueling ground support equipment because HRJ has the exact physical properties of regular aviation fuel. The HRJ biofuel proposed for Albatross is to be delivered to the consumers operation-ready, therefore eliminating the likelihood of blending mistakes made by the ground crew at the airport, which may result in engine operation complications.

13. Cost Analysis

13.1 Flight Path Optimization

Multiple parametric studies were performed in order to optimize the mission profile presented in Sec. 3.2. Given that the aircraft is expected to perform transport missions in a variety of ranges, a parametric study was performed to optimize cruise Mach number and initial altitude for both the 1,200 *nm.* nominal and 3,500 *nm.* maximum design ranges. In order to model the DOC of the aircraft as a function of the mission variables, such as average block speed and initial cruise altitude, the financial model provided by *Roskam*[114] for the estimation of research, technology, development, evaluation, acquisition, and operating costs was programmed into a dynamic spreadsheet. Methods presented in Sec. 10.2 with regard to the estimation of an environmental tax were also added to take into account the effects of flight path parameters on the DOC of Albatross. Considering the previously mentioned results for the engine optimization, the DOC and the corresponding aircraft unit cost were computed for a range of Mach numbers and initial cruise altitudes. The result of these analyses is shown in Figs. 85 and 86

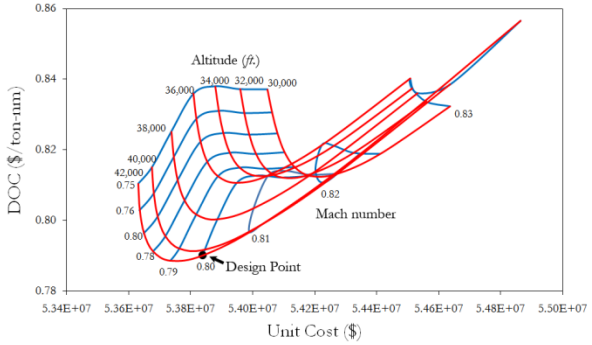

Fig. 85 DOC vs. unit cost for various initial cruise altitudes and Mach numbers, at a range of 3,500 *nm.* for a production run of 500 aircraft.

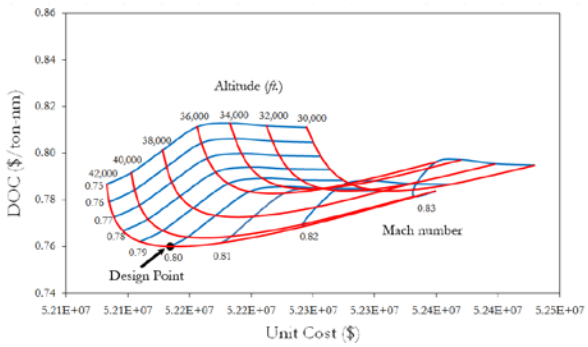

Fig. 86 DOC vs. unit cost for various initial cruise altitudes and Mach numbers, at a range of 1,200 *nm.* for a production run of 500 aircraft..

The analysis indicates that the DOC for maximum range missions rapidly declines as the aircraft starts to fly at higher altitudes and a Mach number in the neighborhood of 0.79. In the 1,200 *nm.* nominal range case, the DOC does not reduce as rapidly as the aircraft flies at higher altitudes. Instead of a Mach number of 0.79, the DOC would be minimized at a Mach number of 0.8 to 0.81. The analysis also indicates that the unit cost of Albatross for a production run of 500 aircraft will be impacted slightly by the chosen flight path parameters. This is due to the impact of the design Mach number and altitude on the structural weight of the aircraft, which in turn impacts the unit cost of the plane.

UACC recommends that Albatross should be flown at a Mach number of 0.81, while flying missions near the nominal range of 1,200 *nm.* The results of the analysis presented in Figs. 84 and 85 indicate that the reductions in DOC due to increasing ICA are minimal above an altitude of 39,000'. Therefore, UACC recommends an ICA of 39,000' for Albatross; however, higher cruise altitudes, if allowed by Air Traffic Control (ATC), will still improve the DOC of the aircraft. While flying missions near the maximum range of 3,500 *nm.*, the aircraft will incur less cost and cause less environmental impact if it is operated at a lower Mach number of approximately of 0.79 and the highest altitude allowed by the ATC. Moreover, given its small fuel consumption achieved via the utilization of advanced propulsion and aerodynamic concepts, Albatross will have an operating cost well below the commercial fleets it will replace.

13.2 Flyaway Cost Breakdown

Given the emphasis by the RFP placed on the competitiveness of flyaway and operating costs, attention was paid to the financial drivers in various stages of the design. *Roskam*'s[115] method was used to estimate the development and acquisition cost. The research and development includes the costs of engineering and design, development and support, prototypes and testing operations, and program financing. It was assumed that the research and technology development of the project will yield a 5% return over a period of three years, while the financing cost will be 7% of the total research and development cost of the project. Acquisition cost includes the costs associated with engineering and design for the manufacturing phase, production program, and test operations, as well as 15% finance fees and a 12% depreciation of invested capital. Sensitivity analysis was performed to assess the effect of variation of the difficulties factors defined by *Roskam* on the final flyaway cost to estimate an uncertainty of the cost figures. The analysis was repeated for two production runs of 500 and 1,500 aircraft, the results of which can be seen in Table 21.

Table 21 R&D, acquisition and flyaway cost breakdown for Albatross, assuming production runs of 500 and 1,500 aircraft

Cost Item	500 Production Run Cost (10^6 $)-2019 U.S. Dollar	1,500 Production Run Cost (10^6 $)-2019 U.S. Dollar
Research & Development Phase:		
Engineering & Design	254	254
Development, Support, & Testing	85	85
Prototype Aircraft	1,426	1,426
Test Operations	52	52
Finance Cost	145	145
R & D subtotal	*1,962*	*1,962*
Profit	103	103
Total	**2,065**	**2065**
Acquisition Phase:		
Engineering & Design	318	445
Production Program	17,452	40,639
Test Operations	67	200
Finance Cost	4,184	9,684
Manufacturing Sub-Total	*22,022*	*50,967*
Profit	2,642	6,116
Total	**24,664**	**57,083**
Flyaway Cost per plane:		
Worst Case Scenario	53.6	39.4
Best Case Scenario	44.7	33.9
Uncertainty	±4.45	±2.75

To investigate the effects of the size of manufacturing on fly-away cost, analysis was performed for a large range of production runs. Figure 87 presents the results of this analysis assuming the highest values for all difficulty factors in *Roskam*'s method (i.e. the worst case scenario). For the purpose of comparison, the market price of the aircraft was also computed for a 20 year production run, assuming an average production rate of 220 planes per year.

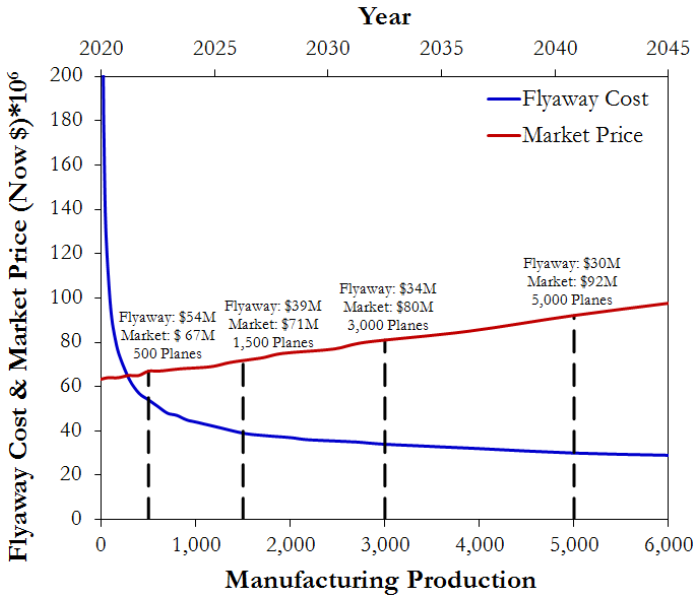

Fig. 87 Flyaway cost & market price vs. manufacturing production

13.3 Operating Cost Breakdown & Competitive Analysis

As requested by the RFP, the operation and maintenance costs of Albatross were computed to assess its viability against current in-service aircraft. *Roskam*'s[116] method was used to perform DOC estimation for both biofuels and conventional JP-10 jet fuel. The cost of regular fuel was obtained by consulting the fuel cost projections obtained from the U.S. Energy Information Administration interactive web portal [117]. This portal presents projections for the cost of energy and main forms of fossil fuels assuming different economic scenarios, modeling the observed trends in energy supply and demand cycles. Reviewing these projections, it was determined that in 2020, an average jet fuel cost of 2.98 *$/gal.* will represent the middle ground between the worst and best economic scenarios. A study by E4tech Company[118] suggests that biofuels are cost comparable at present, but their demand will greatly exceed the production volume if they become commercially

available. This study also indicates that the cost of HRJ related biofuels could be as low as 1.20 *$/gal.* Moreover, the maximum cost for HRJ related biofuels is considered to be dictated by the cost of jet fuel (which can be as high as 2.98 *$/gal*) to preserve competitiveness in the energy market. Furthermore, the study suggests that HRJ related biofuels will be available commercially by 2018, implying that by EIS these biofuels will be substantially cheaper than conventional aviation fuel. Concluding from this study, UACC chose a cost of 2.09 *$/gal.* for HRJ related biofuels. The environmental tax model presented in Sec 10.2 was implemented to account for the benefits incurred by utilization of lower carbon footprint biofuels and flying at higher altitudes.

DOC analyses were performed for Albatross using both conventional aviation fuel and HRJ related biofuels. Similar cost estimations were performed on the Boeing 737 and Airbus A320, assuming comparable utilization times. Table 22 presents the results of DOC comparison analyses for a production run of 500 aircraft.

Table 22 Results of DOC comparison analysis for Airbus A320-200, Boeing 737-800, Albatross with conventional jet fuel, and Albatross with HRJ related biofuels

Cost Item	Airbus A320-200	Boeing 737-800	Albatross (Jet Fuel)	Albatross (Biofuels)	Average Change from Today's Competitors (Jet Fuel, Biofuel)
Annual Utilization (*nm.*)	1,865,256	1,891,081	1,807,932	1,807,932	-------
Crew (*$/nm.*)	0.96	0.95	0.91	0.91	-4.0%, -4.0%
Fuel, Oil, & Env. Tax (*$/nm*)	4.53	3.85	3.01	1.77	-28%, -58%
Insurance (*$/nm.*)	0.15	0.15	0.42	0.42	+280%, +280%
Maintenance (*$/nm.*)	2.96	2.84	2.42	2.42	-17%, -17%
Depreciation (*$/nm.*)	4.93	4.68	1.56	1.56	-67%, -67%
Landing & Navigation Fees ($)	0.40	0.36	0.22	0.22	-42%, -42%
Total DOC* (*$/nm*)	**15.03**	**13.85**	**9.30**	**8.81**	**-35%, -39 %**

From this analysis, it was concluded that Albatross will present extreme reductions in DOC thanks to reductions in TSFC (~35%) and an increase in cruise L/D (~25%). It is also shown that the DOC of Albatross could be reduced by as much as 4% as a consequence of using biofuels. It should be noted that this analysis is only valid for the 2020 market, and this difference will increase as oil prices rise and HRJ related biofuels become more available economically.

* Including the Financing Cost with a rate of 7 percent.

14. Future Recommendations

To improve the certainty of the analysis pertaining to the viability of NLF wings (i.e. to identify the location of transition to turbulence on the upper and lower surface with more accuracy), UACC would like to suggest the utilization of CFD tools with more diverse control over turbulence parameters, as well as superior hardware compatibility allowing for cluster computing. At present, the accuracy of the results presented in this proposal is limited by the maximum computing power accessible by the team. Although some of the analyses presented in this volume have required CPU times well above 40 hours, UACC realizes that, given the relatively low number of fluid cell elements (~1.7 million), these results have to be more accurate to provide applicable transition predictions. There is also potential for research and development into cleaning procedures (on ground or in flight) to ensure the cleanliness of the wing surfaces. Such measures may be critical to the maintenance of laminar flow on the surfaces of the aircraft, although arguments for and against the level of cleanliness has been presented in various sources of literature[119,120]. More modern propulsion elements, such as recuperated and intercooled engine core concepts, may also be utilized to increase the efficiency of the engines beyond the presented performance in this proposal. Other concepts such as inlet water injection may also be utilized to effectively reduce NOx emission levels. As discussed in Sec. 5.1, the unique engine integration of Albatross allows for further expansions of payload capacity with no need to redesign the empennage or wing structure, making Albatross capable of future expansions as the market may demand.

15. References

[1] *Roskam, Jan.*, Airplane Design, Part I through VIII , DAR Corporation, 2003

[2] *Heinemann, E., Raussa, R. and Van Every, K.,* Aircraft Design, The Nautical and Aviation Publication Co., 1985

[3] *Eppinger, Steven D.* and *Ulrich, Karl T.*, Product Design and Development, Second Edition, Irwin McGraw-Hill, Boston, 2000

[4] "Engineering Science Data Unit", Series 3. *Volumes on Aerodynamics,* items 91014. "Maximum Lift of Wings with Trailing-Edge Flaps at Low Speeds". *IHS Inc., 1995*

[5] *Edi, Prasetyo, Fielding, J.P.* Civil-Transport Wing Design Concepts. Journal of Aircraft Vol. 43, № 4. July-August 2006.

[6] "Engineering Science Data Unit", Series 3. *Volumes on Aerodynamics,* items 77028 Amendment F. "Geometric Characteristics of Typical Bodies". *IHS Inc., July 1990*

[7] *Redeker*, *G.*, *Horstmann, K.H.*, *Köster*, *H.*, and *Quast A.* Investigations on High Reynolds Number Laminar Flow Airfoils. Journal of Aircraft Vol. 25 № 7. July 1988

[8] *Lehner*, *Stephan* and *Crossley*, *William*. Hybrid Optimization for a Combinatorial Aircraft Design Problem. Proceedings of 9th AIAA Aviation Technology, Integration, and Operations Conference. 21-23 September 2009

[9] *Holmes, B.J.* Observations and Implications of Natural Laminar Flow on Practical Airplane Surfaces. Journal of Aircraft Vol. 20 №. 12. December 1983

[10] *Roskam*, *Jan.* Airplane Design Part VI Sec. 4.2 p. 23-43. DAR Corporation. 1990

[11] Appendix to Request for Proposal Document for Team Aircraft Design Competition. AIAA. 2008-2009

[12] "Engineering Science Data Unit". *Volumes on Performance,* item 73018. "Introduction to Estimation of Range and Endurance".

[13] "Engineering Science Data Unit". *Volumes on Performance,* item 73019. "Approximate Methods for Estimation of Cruise, Range, and Endurance".

[14] "Engineering Science Data Unit". *Volumes on Performance,* items 74018. "Lost Range, Fuel, and Time Due to Climb and Descent".

[15] *Roskam*, *Jan.* Airplane Design, Part V Ch. 2 p. 3-17. DAR Corporation. 1999

[16] *Godston*, *J.*, and *Reynolds*, *C.* Propulsion System Integration Configurations for Future Prop-Fan Powered Aircraft. Proceedings of AIAA/SAE/ASME 19th Joint Propulsion Conference. Seattle Washington. June 27-29. 1983

[17] *Roskam*, *Jan.* Airplane Design Part I Sec. 341 p. 118-187. DAR Corporation. 1987

[18] *Roskam*, *Jan.* Airplane Design Part II Fig. 12.7 p.286. DAR Corporation. 1997

[19] "Engineering Science Data Unit". *Volumes on Performance,* item 73019. "Approximate Methods for Estimation of Cruise Range and Endurance: Aeroplanes with Turbo-Jet and Turbo-Fan Engines." Amendment C. May 1982

[20] *Roskam*, *Jan.* Airplane Design Part I Sec. 3.2 p 94. DAR Corporation 1997

[21] "Engineering Science Data Unit". *Volumes on Aerodynamics,* item 95021. "Wing Lift Coefficient Increment at Zero Angle of Attack"

[22] "Engineering Science Data Unit". *Volumes on Transonic Aerodynamics,* item 74013. "A Method For Estimating Drag-rise Mach Number at Zero Incidence of Smooth or Bumpy Non-Ducted Axisymmetric Bodies Without or With Fins", Aug 1974.

[23] "Engineering Science Data Unit". *Volumes on Transonic Aerodynamics,* item 83017. "The Wave Drag Coefficient of Spherically Blunted Secant Ogive Forebodies of Fineness Ratio 1.0, 1.5, and 2.0 at Zero Incidence in Transonic Flow." Amendment A. October 1992.

[24] *Dodbele*, *Simha*. Design Optimization of Natural Laminar Flow Bodies in Compressible Flow. Journal of Aircraft. Vol. 29 № 3. May-June 1992.

[25] *Lee*, *Jae-Moon*, *Schrage*, *Daniel* and *Mavris*, *Dimitri*. Development of Subsonic Transports with Natural Laminar Flow Wings. AIAA Journal 98-0406. 1997

[26] *Huenecke*, *Klaus*. Modern Combat Aircraft Design. p. 47 fig. 4-14. Airlife Publishing Ltd. England. 1987

[27] *Lehner*, *S.*, and *Crossley*, *W.* "Combinatorial Optimization to Include Greener Technologies in a Short-to-Medium Range Commercial Aircraft." ICAS 2008-4.10.2, ICAS 2008 Congress including the 8th AIAA 2008 ATIO Conference. Anchorage, AK. September 15-18, 2008.

[28] *Roskam*, *Jan.* citing *Torenbeek*, *E.* Synthesis of Subsonic Airplane Design. Appendix G, p. 533. 1981

[29] *Roskam*, *Jan.* Airplane Design. Part VI. DAR Corporation. 1990. All Sections relevant to Class II drag polar analysis for commercial jets were used.

[30] *Torenbeek*, *E.* Synthesis of Subsonic Airplane Design. Chapters pertaining to low speed aerodynamic predictions. 1981

[31] *Roskam*, *Jan*. Airplane Design. Part VI. DAR Corporation. 1990. All sections presenting a model for relationships between drag and Mach number.
[32] *Morgan*. Turbojet Fundamentals. Douglas Aircraft Company, Inc. Santa Monica, CA. 1956
[33]*McKay, Bruce.ds*, *C*. Next Generation Propulsion & Air Vehicle Considerations.Proceedings of AIAA/SAE/ASME 19th Joint Propulsion Conference. Denver Colorado. August 2-5. 2009
[34]*Holste,F. and Neise, W*, "Noise Source Identification in a Propfan Modeled by Means of Acoustic Near Field Measurements", Journal of Sound and Vibration №203(4), 1997
[35]Shivashankara B., Johnson, D., and Cuthbertson, R. Installation Effection on Counter-Rotation Propeller Noise. Boeing Commercial Airplanes. Proceedings of AIAA 13th Aeroacoustic conference. October 22-24, 1990.
[36]Per research suggestion of Phillip Adkins, Physicist Fellow, University of Southern California
[37] *Hileman*, *James I*., et al. Development of Approach Procedures for Silent Aircraft. Proceedings of the 54th AIAA Aerospace Science Meeting. Reno Nevada. January 8-11. 2007.
[38]*Fischer*, *B*., and *Klug*, *H*. Proceedings of AIAA/SAE/ASME/ASEE 25th Joint Propulsion Conference. Configuration Studies for a Regional Airliner Using Open-Rotor Ultra-High-Bypass Ratio Engines. Monterey, CA. July 10-12. 1989.
[39]*Rangwala*, *A.S*. Turbo-Machinery Dynamics: Design and Operation. McGraw Hill. 2005
[40]*Cumpsty*, *Nicholas*. Jet Propulsion: A simple guide to the aerodynamic and thermodynamic design and performance of jet engines. Second Edition.Cambridge University Press. Ch. 11. 2003.
[41] *Giampaolo*, *Tony*. Gas Turbine Handbook: Principles and Practice. Taylor and Francis. 2009.
[42]*Collie*, *WallisV*., et al. Advanced Propulsion System Design and Integration For a Turbojet Powered Unmanned Aerial Vehicle. Proceedings of the 41st Aerospace Science Meeting and Exhibit. Reno, Nevada. January 6-9. 2003.
[43]*Eckardt, D. and Grieb, H*. Turbofan and Propfan as Basis for Future Economic Propulsion Concepts.Proceedings of AIAA/ASME/SAE/ASEE 22nd Joint Propulsion Conference. Huntsville, Alabama. June 16-18. 1986
[44] Boeing 737 Specification Sheet, BCA Division, http://www.boeing.com/commercial/737family/specs.html.
[45] *Roskam, J*. Advanced Aircraft Analysis Package Help Files, Keyword: Engine CG, DAR Corporation, Wichita, KS, 2010.
[46]"Engineering Science Data Unit".*Volumes on Aerodynamics,* item 83017 Amendment A. "The Influence of Body Geometry and Flow Conditions on Axisymmetric Boundary Layers at Subcritical Mach Numbers." Amendment A. September, 1984.
[47] *Seddon*, *J*. and *Goldsmith*, *E.L*. Intake Aerodynamics Second Edition. AIAA Education Series. Chapter 11. 1990.
[48] *Fujino*, *Michimasa*. Design and Development of the HondaJet. Journal of Aircraft Vol. 42 № 3. May-June 2005.
[49] *Fujino*, *Michimasa*. Wave-Drag Characteristics of an Over-the Wing- Nacelle Business-Jet Configuration. Journal of Aircraft Vol. 40 № 6. November- December 2003.
[50] Committee of Aeronautical Technologies, Aeronautics and Space Engineering Board, Commission on Engineering and Technical Systems, National Research Council of Aeronautical Technology for the Twenty-First Century National Academy Press, Washington, D.C. 1992.
[51] *Schwartz, Emily and Kroo , Ilan M*. Aircraft Design: Trading Cost and Climate Impact. Proceedings at the 47th AIAA Aerospace Science meeting, Stanford University Jan. 5-9, 2009.
[52] *Moir*, *Ian* and *Seabridge, Allan*. Aircraft Systems: Mechanical, Electrical , and Avionics Subsystems Integration Third Edtion. 2008.
[53] *Srimoolanathan*, *Balaji*. Aircraft Electrical Power Systems-Charged with Opportunities. Frost & Sullivan. p.2. 2008.
[54] *Moir*, *Ian* and *Seabridge, Allan*. Aircraft Systems: Mechanical, Electrical , and Avionics Subsystems Integration Third Edtion. 2008.
[55] *Moir*, *Ian* and *Seabridge, Allan*. Aircraft Systems: Mechanical, Electrical , and Avionics Subsystems Integration Third Edtion. 2008.
[56] *Ensign*, *Thomas*. Peformance and Weight Impact of Electrial Environmental Control System and More Electric on Citation CJ2. Proceeedings of the 45th AIAA Aerospace Sciences Meeting and Exhibit. January 8-11, 2007.
[57] *Sinnett*, *Mike*. 787 No-Bleed Systems: Saving Fuel and Enhancing Operational Efficiencies. Boeing Aeromagazine. Iss. 28 Quarter 4. 2007
[58] *Cronin*, *Michael J*. All-Electric vs Conventional Aircraft: The Production/Operational Aspects. Lockheed-California Co. June, 1983.
[59] *Garrison*, *Michael* and *Steffan*, *Scot*. Two-Fault Tolerant Electric Actuation Systems for Space Applications. Proceeding of the 42nd AIAA/ASME/SAE/ASEE Joint Propulsion Conference and Exhibit. July 9-12, 2006.

[60] "Engineering Science Data Unit". *Volumes on Aircraft Performance,* item 83042. "Estimation of Spray Patterns Generated from the Sides of Aircraft Tires Running in Water or Slush." Amendment A. April, 1998.
[61] *Moir*, *Ian* and *Seabridge, Allan.* Aircraft Systems: Mechanical, Electrical , and Avionics Subsystems Integration Third Edtion. 2008.
[62] Boeing Commercial Airplanes. Airplane Characteristics for Airport Planning. Weight Section. August 2009
[63] *Graber*, *Edwin J. Overview* of NASA PTA Propfan Flight Test Program. NASA report number N92-22536.
[64] *Willby*, *J.F.*, *Rennison*, *D.C.*, and *Willby*, *E.G.* Noise Control Predictions for High Speed, Propeller-Driven Aircraft. Proceedings of the 6th AIAA Aeroacoustics Conference. June 4-6. 1980.
[65] *Heimbold, R.L., Cronin, M.J., and Howison, W.* Study of the Application of Advanced Electrical/Electronic Technologies to Conventional Aircraft. NASA/JSC/Lockheed NAS-9-15863, July 1979.
[66] *Howison, W.W.* and *Cronin, M.J.* Electronic/Electric Technology Benefits Study. NASA-LRC/Lockheed NAS-16199. Jan. 1982.
[67] *Cronin*, *Michael J.* All-Electric vs Conventional Aircraft: The Production/Operational Aspects. Lockheed-California Co. June, 1983.
[68] Roskam, Jan. Airplane Design Part V. Section 5. 1999
[69] *Raman Raj et al.* The effects of Advanced Materials on Airframe Operating and Support Costs. The RAND Corporation, Santa Monica, CA. 2003.
[70] "Engineering Science Data Unit". *Volumes on Acoustic Fatigue,* item 84027. "Endurance of Fibre-Reinforced Composite, Laminated Structural Elements Subjected to Simulated Random Acoustic Loading". Amendment C. August, 2001.
[71] Advanced Aircraft Analysis help file on Structure. DAR Corporation. Keyword Libove's Axis. Wichita, Kansas. 2009.
[72] "Engineering Science Data Unit". *Volumes on Aerodynamics,* item 83040. "Method for the Rapid Estimation of Spanwise Loading of Wings with Camber and Twist in Subsonic Attached Flow". Amendment C. July 1995.
[73] *Harris, G.* "Flutter Criteria for Preliminary Design," LTV Aerospace Corporation, Voughts Aeronautics and Missile Division, Engineering report 2-53450/3R-467 under Bureau of Naval Weapons Contract NOW 61-1072C, September 1963.
[74] *Liebeck, R. H., Page, M.A., Rawdon, Blaine K., Scott, Paul W., and Wright Robert A.*, "Concepts for Advanced Subsonic Transports," NASA CR-4628, McDonnell Douglas Corporation, Long Beach, CA, September 1994.
[75] Per suggestion of Mr. Blaine Rawdon, Technical Fellow, Boeing Commercial Aircraft.
[76] *Roskam*, *Jan.* Airplane Flight Dynamics and Automated Flight Controls. Part I Sec. 4.2.2. p. 205. 2003
[77] Per suggestion of Mr. Mark Page, Chief Scientist, Swift Engineering.
[78] Military Specification MIL-F-8785 B Flying Qualities of Piloted Airplanes; 1969: Air Force Flight Dynamics Laboratory, WP AFB, Dayton, Ohio.
[79] *Roskam, J.* Airplane Flight Dynamics and Automatic Flight Controls, Part I, DAR Corporation, 2003, p. 186.
[80] *Roskam, J.* Airplane Flight Dynamics and Automatic Flight Controls, Part I, DAR Corporation, 2003, p. 143.
[81] Military Specification MIL-F-8785 B Flying Qualities of Piloted Airplanes; 1969: Air Force Flight Dynamics Laboratory, WP AFB, Dayton, Ohio.
[82] *Roskam, J.* Airplane Flight Dynamica and Automatic Flight Controls, Part I, DAR Corporation, 2003, p. 205.
[83] *Hoak. D.E.,*"USAF Stability and Control DATCOM, Write Paterson AFB, OH
[84] *J. Roskam,* Airplane Flight Dynamics and Automatic Flight Controls Part I, Section 5.2.4 & 5.2.5 PP 329-337 DAR Corp. 2003
[85] International Air Transport Association Report on Alternative Fuels. p. 1. 2009
[86] International Air Transport Association Report on Alternative Fuels. p. 34. 2009
[87] Air Traffic Action Group. Beginner's Guide to Aviation Biofuels. p.6. May 2009
[88] E4tech. Review of the Potential for Biofuels in Aviation for the Committee on Climate Change. P. 37. August 2009
[89] E4tech. Review of the Potential for Biofuels in Aviation for the Committee on Climate Change. P. 51. August 2009
[90] E4tech. Review of the Potential for Biofuels in Aviation for the Committee on Climate Change. P. 60. August 2009
[91] Air Traffic Action Group. Beginner's Guide to Aviation Biofuels. p.10. May 2009
[92] International Air Transport Association Report on Alternative Fuels. p. 42. 2009
[93] Univeristy of Virginia. Algae: Biofuel or the Future? Science Daily June 2, 2010.
[94] E4tech. Review of the Potential for Biofuels in Aviation for the Committee on Climate Change. P. 59. August 2009

[95] International Air Transport Association Report on Alternative Fuels. p. 35. 2009
[96] International Air Transport Association Report on Alternative Fuels. p. 50. 2009
[97] *Schwartz, Emily and Kroo , Ilan M.* Aircraft Design: Trading Cost and Climate Impact. Proceedings at the 47th AIAA Aerospace Science meeting, Stanford University Jan. 5-9, 2009.
[98] ICAO Annex 16 to the Conventional International Civil Aviation. Environmental Protection Vol. I. Aircraft Noise. July 2008.
[99] Annex 16 to the conventions on International Civil Aviation, Volume I, Aircraft noise, P. II.3.3 dated 20/11/2008, International Civil Aviation Organization
[100] *Hanson*, *D.B.* Counter Rotation Propellers. Proceedings of AIAA/NASA 9th Aeroacoustics Conference. October 15-17, 1984.
[101] "Engineering Science Data Unit". *Volumes on Aircraft Noise,* item 96027. Estimation of the Unsteady Lift Coefficient of Subsonic Propeller Blades in Non-axial Inflows. May 1997
[102] *Marte*, *Jack E.* and *Kurtz, Donald W.* NASA Technical Report 32-1462. A Review of Aerodynamic Noise from Propellers, Rotors, and Lift Fans. Jet Propulsion Laboratory. January 1970.
[103] "Engineering Science Data Unit". *Volumes on Aircraft Noise*, item 90023. Amendment D. Airframe Noise Prediction. December 2008.
[104] "Engineering Science Data Unit". *Volumes on Aircraft Noise*, item 05001. Prediction of Combustor Noise from Gas Turbine Engines. February 2005.
[105] "Engineering Science Data Unit". *Volumes on Aircraft Noise*, item 02008. Amendment A and B. Aerodynamics and Aero-Acoustics of Rectangular Planform Cavities. September 2006.
[106] *Zimcik*, *D.G.* Active Control of Aircraft Cabin Noise. RTO AVT Symposium on Habitability of Combat and Transport Vehicles. October 4-7, 2004.
[107] "Engineering Science Data Unit". *Volumes on Performance,* item 85029. "Calculation of Ground Performance in Takeoff and Landing". Amendment A. March 2006.
[108] "Engineering Science Data Unit". *Volumes on Aerodynamics,* item 71007. "Low Speed Normal Force and Itching Moment of Slender Wings in Ground Effects". June 1971
[109] *Roskam*, *Jan.* Airplane Design Part VII Sec. 5.2 p. 117-123. DAR Corporation. 1991
[110] *Banke, Jim.* Shhhh! Keep It Down, Please. NASA news topics on aeronautics. http://www.nasa.gov/topics/aeronautics/features/aircraft_noise.html. Retrieved May 2010.
[111] Berton, Jeffrey J., and Envia, Edmane. An Analytical Assessment of NASA's N+1 Subsonic Fixed Wing Project Noise Goal. Proceedings of the 15th AIAA/CEAS Aeroacoustics (30th AIAA Aeroacoutics) Conference. May 11-13, 2009.
[112] Engineering Science Data Unit". *Volumes on Performance,* item 84040. "First Approximation for Landing Field Length for Civil Transport Airplanes (50 ft, 15.24 m screen)". December 1984
[113] *Roskam*, *Jan.* Aircraft Design Part II Sec. 11.3. p. 267-268. DAR Corporation. 1997.
[114] *Roskam Jan.*, Airplane Design Part VIII ; Section 5.2.4; DAR Corporation. 1990.
[115] *Roskam Jan.*, Airplane Design Part VIII ; Section 4.2 P 50-54; 1999
[116] *Roskam*, *Jan.* Airplane Design Part VIII. DAR Corporation 1990.
[117] U.S. Energy Information Administration, independent statistics and analysis. Annual Energy Outlook. May 11, 2010
[118] E4tech. Review of the Potential for Biofuels in Aviation for the Committee on Climate Change. P. 76. August 2009
[119] *Holmes*, *B.J.* and *Obara*, *C.J.* Observations and Implications of Natural Laminar Flow on Practical Airplane Surfaces. AIAA Journal of Aircraft. Vol 20 № 12. December 1983
[120] *Hermanspann*, *Fred.* Rain Effects on Natural Laminar Flow Airfoils. Proceedings of the AIAA 34th Aerospace Sciences Meeting and Exhibit. Jan 15-18, 1996